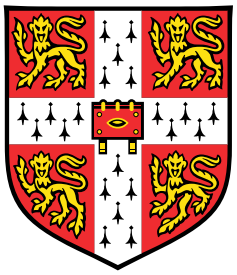

A Schottky-to-Ohmic Transition in Epitaxial Ferroelectric Hafnia Devices

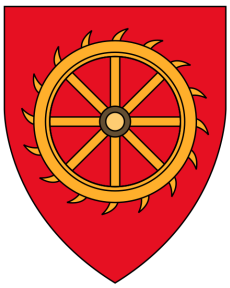

Moritz Leander Müller

Supervisor: Prof. Judith Driscoll

Department of Materials Science and Metallurgy
University of Cambridge

This dissertation is submitted for the degree of
Doctor of Philosophy

St. Catharine's College

August 2024

Declaration

This thesis is the result of my own work and includes nothing which is the outcome of work done in collaboration except as declared in the preface and specified in the text. It is not substantially the same as any work that has already been submitted, or is being concurrently submitted, for any degree, diploma or other qualification at the University of Cambridge or any other University or similar institution except as declared in the preface and specified in the text. It does not exceed the prescribed word limit for the relevant Degree Committee.

Moritz Leander Müller
August 2024

To my family.

Abstract

The development of analog resistive non-volatile memory elements is of great interest for future information storage technology. These devices can be used to emulate the electronic behaviour of biological synapses and neurons for neuromorphic computing or sensing applications. Hafnia is a promising material to use in resistive memory systems due to its high industrial compatibility. Both the migration of oxygen ions and ferroelectricity are two mechanisms actively being explored to drive resistance change in hafnia based devices. This thesis explores the interplay between interfacial redox chemistry and ferroelectricity and how these influence the resistance switching behaviour in epitaxial hafnia films.

A device stack is engineered to elicit large resistance changes through both ferroelectricity and interfacial redox reactions. Ultra-thin epitaxial Y doped HfO_2 (YHO) is grown with a controlled oxygen stoichiometry. To stabilise the polar phase in YHO and provide a resistance-tuneable bottom interface, YHO is grown on $La_{0.66}Sr_{0.33}MnO_3$ (LSMO) buffered Nb doped $SrTiO_3$ substrates. In-depth X-Ray diffraction based structural analysis identified the polar nature of the film and a strain induced rhombohedral distortion. Ferroelectricity in the film was confirmed by piezoresponse force microscopy. In device configuration, using an Au top electrode with an ultra-thin Ti adhesion layer, a resistance switching mode with large on-off ratio was observed. The pristine device was stabilised in an intermediate resistance state and did not need an electro-forming process. The mode reversibly switched between a purely capacitive (Schottky) and resistive (Ohmic) state, a Schottky-to-Ohmic transition (SOT). A series of voltage pulse trains were used to explore the intermediate resistance states of the system. Both analog and integration behaviour was demonstrated, depending on the pulse profile. The SOT may therefore find application as both a synapse and a neuron respectively in neuromorphic applications.

Capacitance-voltage measurements were employed to correlate the ferroelectric polarisation reversal with the SET process and not the RESET process. Therefore, ferroelectricity was indicated to only be partially responsible for the observed resistance change. Electrode area dependent current measurements suggested that in the low resistance state, current transport occurred through a localised conductive filament. A detailed analysis of the interface chemistry suggested the importance of precisely designed oxygen scavenging at both

interfaces to stabilise the SOT. Furthermore, interface stoichiometry changes were observed during resistance switching by a combined hard photo-electron spectroscopy and electron energy loss spectroscopy study.

Impedance spectroscopy measurements were used to correlate the stoichiometry changes at the LSMO|YHO interface to resistance changes during the SOT. The conductive pristine resistance state was shown to predominantly be limited by the LSMO|YHO interface and was proposed to occur due to oxygen scavenging at the top electrode, by-passing through-grain conduction. Analysis of the SOT analog switching behaviour showed that both the YHO layer and the LSMO|YHO interface switch separately during the RESET operation, but simultaneously during the SET process. Furthermore, stack modifications demonstrated the importance of using an ultra-thin LSMO to stabilise the SOT. It was hypothesised to occur due to interface strain enhanced defect formation, oxygen transfer or symmetry changes at the LSMO|YHO interface.

Acknowledgements

I am immensely grateful for all the support I have received throughout this PhD from colleagues, friends and family.

First and foremost, I would like to thank Prof. Judith Driscoll for giving me the opportunity to pursue a PhD in novel non-volatile memory systems, which gains relevance by the day. Thank you for sharing your wisdom on thin-film growth techniques and architecting complex heterostructures. Your constant strives for excellence, putting ideas into commercial perspective and encouragement as well as giving me the opportunity to apply my skillset and develop outside of the PhD has shaped me personally and professionally.

I am grateful for the financial support I have received and would like to thank the following institutions and individuals in particular: Centre for Doctoral Training in Nanoscience and Nanotechnology, Cambridge Display Technology Ltd., the Cambridge Philosophical Society, and Dr. Bill Welland.

This PhD would not have been the same, nor even possible without our constant exchange, Dr. Maximilian Becker and Dr. Nives Strkalj. Max, thank you for your constant input, great trips abroad, Zukunftsschmieden, scientific approach, teaching me impedance spectroscopy, shaping my perspective to the potential of ferroelectrics and a great friendship. Thank you Nives for always, without exception, having an open ear and taking the time to talk all matters science, life and philosophy. Your patience, openness and rigour really left an impression. Working and learning together these past years has been a joy.

I would like to thank the following for their invaluable experimental expertise and support for teaching of these techniques. Dr. Nadia Stelmashenko for teaching me electrode sputtering and AFM. Dr. Mary Vickers, Dr. Gulio Lapronti and Wayne Skelton-Hough for the introduction, guidance and assistance high resolution on X-Ray crystallography. Prof. Rachel Oliver and Dr. Saptarsi Ghosh for helping me with scanning probe microscopy. Dr. Gunnar Kusch for assisting me during cathodoluminescence measurements. Dr. Simon Fairclough for performing STEM measurements and helping me interpret EELS data.

I'd also like to thank the members of Device Materials Group all the shared memories. In particular, thank you to Dr. Megan Hill for sharing her expertise in photoelectron-spectroscopy and being a great beam-time partner. Thank you, Dr. Matt Wells for introducing

me to PLD and our chats about art. Dr. Markus Hellenbrand for interesting discussions and always having an open ear to troubleshoot equipment. I thank Ji Soo Kim, Sunil Taper and Atif Jain for our discussions about ferroelectrics and going through this PhD journey together. Thank you, Benedetta Gaggio for always showing up with energy.

I'd like to acknowledge and thank Prof. Marin Alexe for sharing his knowledge on ferroelectric resistance switching and scientific discussions.

I'd like to thank Jack, Tom, Abi and Semih for all the tennis sessions, coffee breaks and chats we had throughout the years. Nell, Dan, thank you for always being there. From early morning drives, to midday walks and lunches, afternoon coffees, after-work adventures, and late-night dinners. We lived this PhD together. Thank you for your never-ending support and friendship.

Thank you to my family. There from day one, who taught me to be curious and dig down to discover the way things worked. Always asking questions, taking in the wonders of the world around. From the Maillard reaction to surface tension and sunscreen, you have grown and shaped the scientist in me, for which I'll be forever grateful. Thank you for supporting and encouraging me. Without family at the core, this would not have been possible.

Table of contents

List of figures

List of tables

Chapter 1

Introduction

The development of computing devices and efforts to represent natural intelligence in hardware have long co-evolved [1].

The growth in transistor density and associated computational power has steadily kept pace with Gordon Moore's empirical prediction that the number of transistors on an integrated chip would double roughly every 24 months [2], later to become known as Moore's law. The increase in component density was accompanied by favourable Dennard scaling, which demonstrated that as transistors decreased in size, their areal power density remained constant [3]. This allowed manufacturers to massively increase the performance of their chips without ballooning energy consumption. As transistor sizes reached the nanometre scale, Dennard scaling began to falter. Quantum mechanical effects influenced current leakage, leading to increased power consumption and began to limit processing speed. To combat this, transistor material chemistries were modified and computer architectures began to depart from performing computing tasks sequentially and moved towards parallelising operations, which proved particularly useful for data-intensive applications.

Artificial neural networks (ANNs) are a collection of statistical methods aimed at pattern recognition by emulating functions of the human brain. As processing power increased, ever larger ANNs were created. Tracking the advances in artificial intelligence is challenging since progress algorithms and data are difficult to quantify. However, the total compute necessary to train the most advanced machine learning (ML) models can be evaluated [4, 6], see Fig. 1.1 a). Before 2010, the compute demand from ANNs was roughly in line with that of Moore's law, doubling every 24 months. Around 2012, an inflection point occurred. Inherently parallel computing architectures, such as graphics processing units (GPUs), were starting to be used to train ML models. Parallelisation proved to be extremely viable. As modern neural network architectures [7] scale tremendously well from using bigger models,

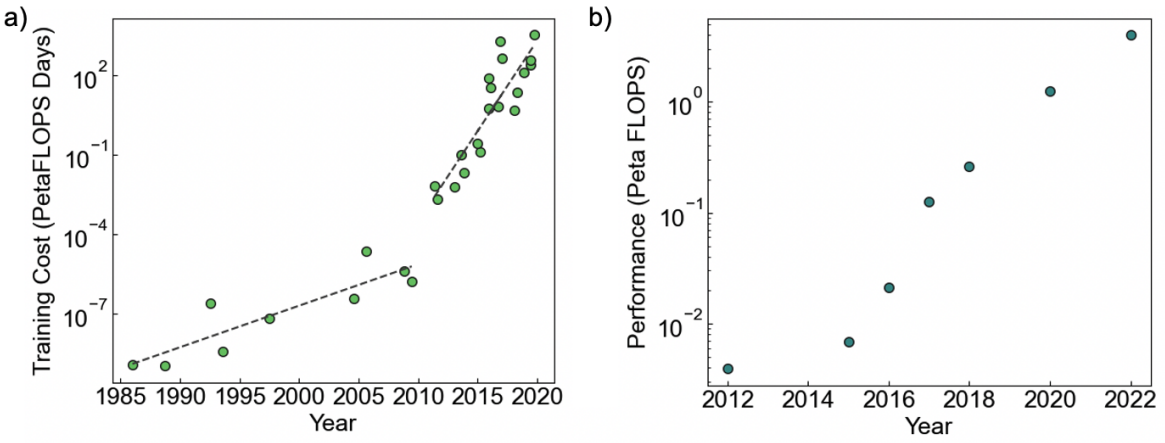

Figure 1.1: a) Compute demand for ML models, data from [4], b) Inference performance of NVIDIA datacentre GPUs, data from [5].

larger datasets and longer training time[8], a boom in compute demand for model training ensued, doubling every $\sim$3 months.

The growth in compute demand has outpaced the growth in compute performance of even the most advanced GPUs. Fig. 1.1 b) displays NVIDIA datacentre GPU's processing performance for comparison. Over the past decade GPU performance supply improved 10^3x, while training demand increased by almost 10^5x. At the time of this writing, we are currently witnessing a historic build-out of compute capacity, with data-centres expanding rapidly to train next-generation models. Yet this scale-up of computational capacity also escalates its energy consumption, which may create stresses in electricity supply [9, 10]. While the slow-down of Dennard scaling has limited improvements in processing efficiency, this is not the limiting factor [11]. The root of the problem originates from the von-Neumann architecture, on which almost all modern chips are built [12]. The separation between random access memory (RAM) and compute requires a resource-intensive data transfer, which can have a $\approx$100x higher energy cost than processing it [13, 14], resulting in the so-called von-Neumann bottleneck. A number of solutions have been proposed to circumvent or alleviate these limitations, including novel architectures, 3D stacking of components [15], using optical data-transfer on chip [16] or even entirely novel computing paradigms [17].

This thesis discusses the use of analog resistive memories to directly perform in-memory computation and representing the synapses and neurons of artificial neural networks (ANNs) in hardware [1]. ANNs consist of a large diversity components, of which the perceptron is one of the simplest building blocks [20]. A perceptron receives signals from multiple input nodes, where each input signal is multiplied by its associated synaptic weight. The weighted signals are summed and passed through an activation function, where processed signal is propagated

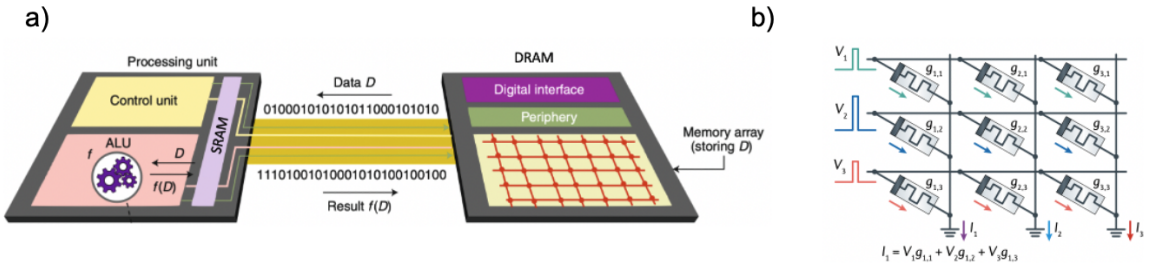

Figure 1.2: a) Schematic of the data shuffling in the von Neumann Architecture, with permission from [18] b) Vector-matrix multiplication in a crossbar array, with permission from [19].

to subsequent perceptrons. In the von Neumann architecture this multiply-and-accumulate (MAC) operation requires extensive data movement, see Fig 1.2 a), from the processing unit to external dynamic random access memory (DRAM). Fast, near compute storage, static random access memory (SRAM), is limited due to its low areal density. However, if analog resistive memories are arranged in a crossbar array, as shown in Fig 1.2 b), Ohm's and Kirchhoff's law can be used to directly perform the MAC operation in memory during a single compute cycle [18]. Synaptic weights are stored in analog resistive memories as conductance values. More complex computations can be achieved by using voltage pulses to represent action potentials, leveraging the temporal and higher order dynamics in the resistive memories [21, 22].

1.1 Thesis Aim

This thesis aims to investigate the ferroelectricity and oxygen electrochemistry of HfO_2 based heterostructures through their memristive response. Both modes have been shown to individually exhibit memristive properties. By studying these concurrently in a single memristive system, we aim to uncover insights into the nanoscale screening phenomena in ferroelectric HfO_2 and the nature of its ferroelectricity. The memristive response is engineered by tuning both the film and the interfaces of HfO_2. The growth of the ferroelectric phase is favoured by doping the film with aliovalent Y, which further introduces a controlled concentration of oxygen vacancies. The heterostructures are grown epitaxially to minimise the effect of non-ferroelectric phases. This will be achieved by growing the film on $La_{0.67}Sr_{0.33}MnO_3$ (LSMO) buffered substrates, which can stabilise the epitaxial growth and provide a rich platform for memristive behaviour, especially in the ultra-thin regime due to its thickness dependent resistance tunability. To disentangle the memristive response hard X-Ray photoelectron spectroscopy (HAXPES) and impedance spectroscopy will be used. HAXPES is a particularly powerful technique to track redox reactions and changes in band-alignment between resistance states, whereas impedance spectroscopy can deconvolute resistance and capacitance changes within various elements of the device stack.

Chapter 2

Theory and Background

Chapter Summary

This chapter introduces the theoretical background and covers literature context for the data presented in the experimental chapters.

The first section covers the phenomenon of ferroelectricity and how surface charges are screened through external electrodes and charge carriers residing within the film. The emergence of ionic defects, how these can interact with electric charge carriers and the transport of ions and electrons is discussed. Next, the literature is surveyed on how ferroelectricity and ionic defects can modify conduction currents in thin film devices and lead to various resistance switching modes. Finally, the specific materials used in this manuscript are detailed and how their unique properties may contribute to resistance switching response.

2.1 Theory

2.1.1 Ferroelectricity

Polarisation

Ferroelectric materials are natural candidates for memory applications, owing to their switchable spontaneous polarisation. Dielectric materials in the linear approximation exhibit a polarisation $\mathbf{P}^D$ under applied electric field $\mathbf{E}$ due to alignment of of dielectric dipoles, according to

$$\mathbf{P}^D(\mathbf{E}) = \varepsilon_0(\varepsilon_r - 1)\mathbf{E}, \tag{2.1}$$

where ε_0 is the permittivity of free space and ε_r the relative permittivity. Ferroelectric materials possess an additional spontaneous polarisation $\mathbf{P}^{FE}$, such that the total polarisation is $\mathbf{P} = \mathbf{P}^D + \mathbf{P}^{FE}$. Below the Curie Temperature T_C, a phase transition occurs from a paraelectric to a ferroelectric phase. In displacive ferroelectrics, this is accompanied by the freezing out of a soft-mode phonon, resulting in the formation of a spontaneous polarisation [23]. When sandwiched between conductive electrodes and upon application of an electric field above a characteristic coercive field $E \geq E_c$, the ferroelectric capacitor exhibits a hysteretic **P**-**E** relationship as shown in Fig 2.1 a). This is contrast to dielectric polarisation, which has a linear relation with the electric field [24]. The polarisation switches orientation at $|\mathbf{E}| > E_c$, reaches a maximum at the saturation polarisation P_s and on removal of the field, retains a remnant polarisation P_r. Around E_c, the polarisation passes a region of zero net polarisation. Intermediate states of ferroelectric polarisation originate from the the formation ferroelectric domains, that are locally uniform regions of ferroelectric polarisation. The net polarisation is described as a sum of the polarisations of individual domains

$$\mathbf{P}^{FE} = \Sigma_{i=1}^{N} P^i_{domain}, \tag{2.2}$$

where N is the number of domains with polarisation P^i_{domain}. Different orientations of ferroelectric polarisation are separated by a ferroelectric domain wall [25].

Ferroelectric capacitor structures form the basis of commercial ferroelectric memories [26]. The write operation is the application of a voltage pulse, where $V \geq V_C$, to the capacitor changing the direction of the ferroelectric polarisation and representing logic '0' and '1'. One of the common ways to measure polarisation relies on the determination of the displacement current density $J_D = \frac{d\mathbf{D}}{dt}$, which is a time derivative of the displacement field $\mathbf{D} = \varepsilon_0\mathbf{E} + \mathbf{P}$. If there is no change in conduction current density J_C, the read operation requires a unipolar

destructive voltage pulse V≥V_C. Polarisation reversal causes a significant increase to J_D and allows the deduction of the previous polarisation state by means of a charge reference.

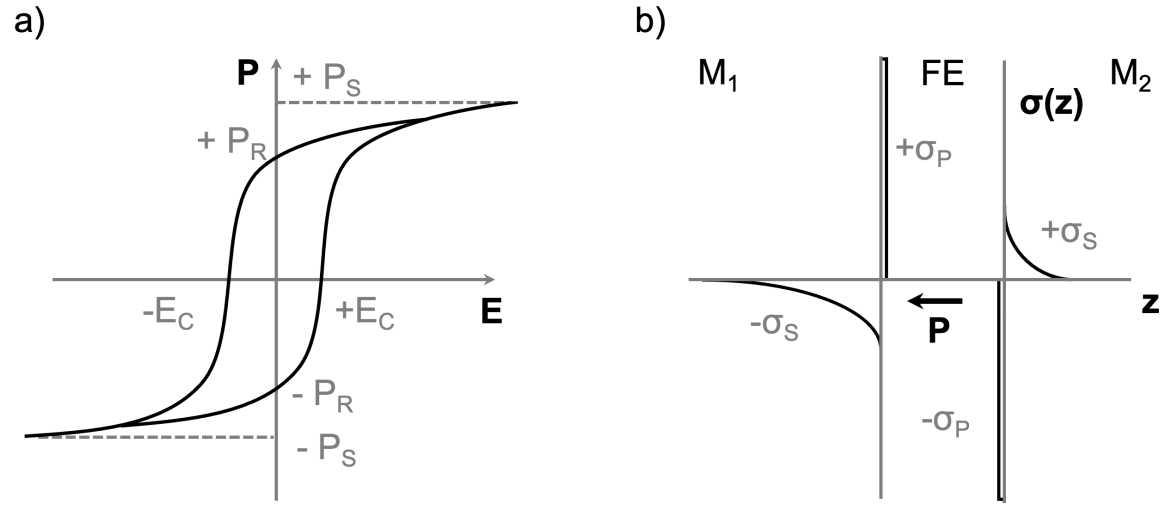

Figure 2.1: a) Polarisation - electric field relation of a ferroelectric. Adapted with permission from Ref. [23] b) Charge density distribution of a ferroelectric capacitor with two different electrode materials. Fig. adapted with permission from Ref. [27].

Polarisation Screening

Interfaces of a ferroelectric material host bound charges giving rise to a depolarising field, E_D. The energy minimum of the system is a balance between the energy reduction from the polarization stabilisation and and the energy increase associated with the resulting depolarizing field. It is therefore necessary to consider the screening of bound charges. Ideally, the ferroelectric polarisation is screened by an infinitesimally thin sheet charge density σ_S just outside of the ferroelectric surface, perfectly compensating the ferroelectric surface charge density $\sigma_P = \mathbf{P}$. Real metals have a finite Thomas-Fermi screening length, l_i, such that the σ_S extends into the metal along dimension z, see Fig. 2.1 b). The screening charge σ_S of a ferroelectric capacitor is dependent on the polarisation P, the ferroelectric thickness d, the relative permittivity of the ferroelectric ε_r and and the ionic permittivity of each metal $\varepsilon_{M,i}$, where i = 1,2 stand for metal M_1, M_2.

$$\sigma_S = \frac{Pd}{\varepsilon_r(\frac{l_1}{\varepsilon_{M,1}} + \frac{l_2}{\varepsilon_{M,2}}) + d} \tag{2.3}$$

The difference between σ_S and P governs the magnitude of the depolarising field E_D [28].

$$E_D = -\frac{\sigma_P - \sigma_s}{\varepsilon_0 \varepsilon_r} \tag{2.4}$$

This relation can be examined in two limits. At perfect screening $l_n \to 0$, σ_S = P and $E_D = 0$. Here the polarisation is perfectly screened. On the other hand, if $l_n \to \infty$, σ_S = 0 and E_D = -$\frac{\sigma_P}{\varepsilon_0 \varepsilon_r}$. The polarisation is not screened at all, which leads to the suppression of net polarization, for example through the formation of domains [27]. The screening of ferroelectric polarisation is complex and can come in a variety of forms, interested readers are encouraged to refer to the following reference [29]. Importantly, the depolarisation field becomes more significant as the thickness of the ferroelectric decreases.

Finally, we will consider the case, where the ferroelectric material itself contains residual free charge carriers. When a metal and a semiconductor are brought into contact, dissimilar Fermi levels are equalised, often through a charge transfer between the two materials. For an n-type material in contact with a high work-function metal, this results in electron carrier depletion with a width w. The carrier depletion bends the valence and conduction band upwards resulting in the formation of an interfacial Schottky barrier of height ϕ_b^0 [30]. The barrier height formation is complex [31] and is dependent on the band-offsets [32], density of interface states [33], the dielectric constant [34, 35] and the doping density [36] of the material. A built-in voltage V_{bi} is present, which is dependent on the density of states in the valence band of the semiconductor N_V,

$$V_{bi} = \phi_B^0 - \frac{k_B T}{q} \ln\left[\frac{N_V}{\rho(T)}\right], \tag{2.5}$$

where k_B is the Boltzmann constant, T the temperature, q the electronic charge and ρ the charge carrier concentration. The presence of a ferroelectric polarisation induces an additional surface charge density, which modifies the built-in voltage according to $V'_{bi} = V_{bi} \pm \frac{P}{\varepsilon_0 \varepsilon_{st}} \delta$, where δ is the distance between the ferroelectric surface charge and the material interface and ε_{st} the static permittivity. The depletion region width w of the Schottky barrier, in equation 2.6, is therefore not only dependent the total charge carrier density N_{eff} but also on the ferroelectric polarisation. This can give rise to interesting polarisation-dependent transport phenomena, as discussed in section 2.2.1

$$w = \sqrt{\frac{2\varepsilon_0 \varepsilon_{st}(V + V'_{bi})}{q N_{eff}}}. \tag{2.6}$$

2.1.2 Ionic Defects

Defect Generation

The presence of ionic defects is unavoidable in crystalline materials. These imperfections can create energy levels within the bandgap and therefore strongly influence the electronic, optical and magnetic properties of a material [37], often degrading the performance of a functional device. However, the controlled incorporation of defects can be beneficial in certain applications. Here, we will only consider one of the most prevalent zero-dimensional defects present in oxide thin films, the oxygen vacancy. Defects form through three primary mechanisms: thermodynamics, redox reactions or impurities [38]. Formation pathways are represented through chemical reactions using the Kröger-Vink notation [39].

The formation of ionic defects is dependent on its Gibbs free energy of formation, $\Delta G_{form} = \Delta H_{form}\text{-}T\Delta S_{form}$, where ΔH_{form} and ΔS_{form} are the enthalpy and entropy of defect formation. At finite temperature, defects are natively present due to the entropic contribution to the free energy. An example would be the formation of a Frenkel defect, where an oxygen ion O_O departs its lattice position to become an interstitial ion O_i and leaving an oxygen vacancy V_O.

$$O_O^X \leftrightarrow O_i'' + V_O^{\bullet\bullet} \tag{2.7}$$

The free energy of formation is also strongly influenced by the oxygen chemical potential. When two materials of differing oxide formation energies are interfaced, an equilibrium oxygen concentration is established through redox across the interface of the two materials $\Delta G = RT \ln K$, where K is the equilibrium constant and R the gas constant. This process is often kinetically limited due to low oxygen mobility at ambient conditions. The redox reactions creates a degree of non-stoichiometry in the reduced material, which also results in the formation of additional electronic charge carriers.

$$\mathrm{O_O^X} \leftrightarrow V_{\mathrm{O}}^{\cdot\cdot} + 2e' + \frac{1}{2}\mathrm{O_2} \tag{2.8}$$

Finally, aliovalent impurities spuriously present or deliberately incorporated can create oxygen vacancies. For semiconductors such as silicon, doping a host lattice with aliovalent elements results in the creation of electronic charge carriers. However, wide bandgap materials, such as ZrO_2 or HfO_2 only have a narrow range in which the Fermi level is stable [40]. Instead, aliovalent doping, which pushed the Fermi level beyond the stable range, results in the formation of ionic defects. To illustrate, the trivalent N^{3+} is replacing the tetravalent M^{4+} in the MO_2 lattice. The substitution of N^{3+} creates valence band hole state,

which shifts the chemical potential, such that the creation of a compensating oxygen vacancy becomes favourable.

$$N_2O_3 + 2M_M^{\times} + O_O^{\times} \rightarrow 2N_M' + V_O^{\cdot\cdot} + 2MO_2 \tag{2.9}$$

Charge Trapping

Mid-gap defect states interact with electronic charge carriers. If the trap state lies beneath the Fermi level, an electronic charge carrier can become trapped. The Shockley-Read-Hall theory [41] describes the generation (electron-hole pair creation), recombination (electron-hole pair annihilation) and immobilisation (trapping) of charge carriers by ionic defects. The trapping mechanism can be broken down into, capture: carrier finds imperfection and becomes immobilised, and emission: thermally or otherwise excited charge carrier is released back into conduction or valence band. The life time, τ_e, for which a charge resides within a trapped state, depends on the energy difference between the trapped state, E_t, and the conduction (valence) band for electrons (holes), E_C (E_V). τ_e is further influenced by the capture cross-section σ, N_C the effective defect density and v_{th} the average carrier thermal velocity.

$$\tau_e = \frac{1}{N_C \sigma v_{th}} \exp\left(\frac{E_C - E_t}{k_B T}\right) \tag{2.10}$$

2.1.3 Transport

Electronic transport

The investigation of electronic transport mechanisms is an essential part in the study of resistive switching memories. Identifying the type of transport present in different resistance states can yield information about where in the device stack the resistance change is occuring. Transport measurements are performed in low sweep-rate, steady-state conditions to avoid any impact from displacement currents. Careful field, temperature, and thickness-dependent current measurements are required to properly identify a transport mechanism [42]. This however is a challenging task, since a multitude of mechanisms can occur in parallel and series with each-other. It is therefore useful to perform conduction mechanism studies in conjunction with impedance spectroscopy.

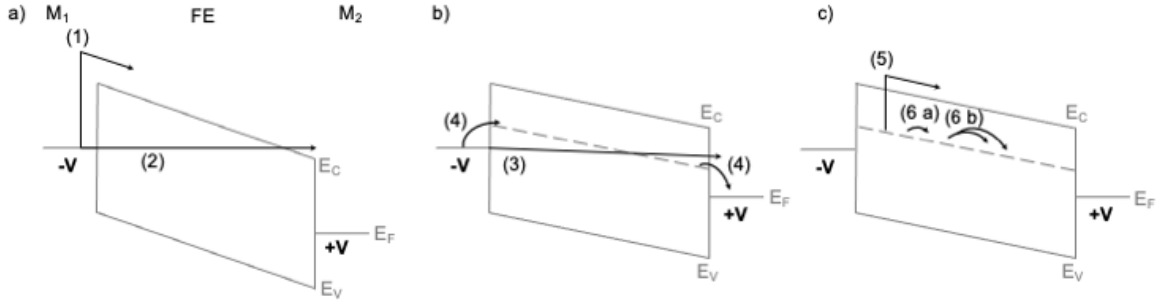

Figure 2.2: Illustration of current transport across nanoscale dielectrics, showing, a) Schottky emission, Fowler-Nordheim tunneling, b) direct tunneling and trap-assisted tunneling, c) Poole-Frenkel emission and hopping conduction a) Fig. adapted with permission from Ref. [42].

A selected number of conduction mechanisms are visualised in Fig.2.2. Even when considering a *non-defective* tunnel barrier, transport can occur through thermionic emission, above the barrier (1), Fowler-Nordheim tunnelling, through the barrier into the conduction band (2) or tunnel directly through the dielectric (3). Each mechanism dominates at different thicknesses, field and temperature [28]. The presence of intragap defect energy levels significantly complicates the conduction mechanism analysis and often leads to increased leakage current through different mechanisms, illustrated in Fig.2.2 b). A summary of the conduction mechanisms investigated in this manuscript is given in Table 2.1.

Table 2.1: Summary of conduction mechanisms, adapted with permission from [42]

Mechanism	**Current Density Expression**
1) Thermionic Injection (TI)	$J_{TI} = A^{**}T^2 \exp\left[-\frac{1}{k_B T}\left(\Phi_B - \sqrt{\frac{e^3 E}{4\pi\varepsilon_0\varepsilon_{ifl}}}\right)\right]$
2) Fowler-Nordheim (FN) Tunneling	$J_{FN} = \frac{e^3 m_e}{8\pi h m_{e,ox}\Phi_B} E^2 \exp\left[-\frac{8\pi\sqrt{2m_{e,ox}}}{3he}\frac{\Phi_B^{3/2}}{E}\right]$
3) Direct Tunneling (DT)	$J_{DT} \approx \exp\left[\frac{-8\pi\sqrt{2qm^*}}{3h}\sqrt{m^*\phi_B}\kappa t_{ox}\right]$
4) Trap-Assisted Tunneling (TAT)	$J_{\mathrm{TAT}} = A\exp\left[-\frac{8\pi\sqrt{2qm^*}}{3hE}\phi_T^{3/2}\right]$
5) Poole-Frenkel (PF) Emission	$J_{PF} = q\mu N_C E \exp\left[\frac{-q\left(\phi_T - \sqrt{\frac{qE}{\pi\varepsilon_i\varepsilon_0}}\right)}{k_B T}\right]$
6) Hopping Conduction	$J_{\mathrm{Hopping}} = qanv\exp\left[\frac{qaE}{kT} - \frac{E_a}{kT}\right]$
a) Nearest neighbour hopping	
b) Variable range hopping	
7) Ohmic Conduction	$J_{\mathrm{Ohmic}} = \sigma E = q\mu N_C E \exp\left[-\frac{E_C - E_F}{kT}\right]$
8) Space-Charge Limited Conduction (SCLC)	
a) Ohmic Region	$J \propto V$
b) Child's Square Law	$J_{SCLC} = \frac{9}{8}\varepsilon_0\varepsilon_r\mu\Theta\frac{V^2}{d^3}$
c) Steep Increase	

Where J is the current density, m^* the effective electron mass, A^{**} is the Richardson constant, E is the electric field, k_B is the Boltzmann constant, T is the temperature, Φ_B is the barrier height, h is the Planck constant, q is the electron charge, ε_0 is the permittivity of free space, ε_{ifl} is the dielectric constant of the insulator, μ is the mobility, N_C is the effective density of states in the conduction band, E_C is the conduction band edge, E_F is the Fermi level, ϕ_T is the trap depth, V is the applied voltage, ε_r is the relative permittivity, Θ is the ratio of free to trapped charge, d is the thickness of the material, a is the hopping distance, n is the density of localized states, v is the attempt-to-escape frequency, ϕ_B is the barrier height, κ is the tunneling attenuation factor, and t_{ox} is the oxide thickness.

Ionic Transport

In thin film metal-insulator-metal geometry, ion migration can become appreciable at high fields, high temperatures and low thickness. The relevant driving forces are the electric field, Soret thermo-phoresis and Fick diffusion. Here, oxygen vacancy migration is considered. In dilute cases, the ionic motion is modelled as oxygen vacancies hopping between two wells, separated by a potential barrier [43]. The reaction coordinate is described by Gibbs energy of migration $\Delta G_{mig} = \Delta H_{mig}\text{-}T\Delta S_{mig}$, where ΔH_{mig} and ΔS_{mig} are the enthalpy and entropy of the reaction respectively. For most binary oxides, $\Delta H_{mig} \approx 0.5 - 1$ eV [44]. The probability of successfully completing a jump across the potential barrier, Γ, is thermally activated, with ν_0 being the attempt frequency.

$$\Gamma = \nu_0 exp\left(\frac{-\Delta G_{mig}}{k_B T}\right), \tag{2.11}$$

The presence of an electric field, **E**, modifies the potential barrier and subsequently the forward and reverse jump probabilities. Using the treatment of Mott and Gurney [45], such that $\Delta H_{mig}(E) = \Delta H_{mig} \pm \mathbf{E}|z_i|ea_i$. The charge of the ion i being $|z_i|e$ and a_i, the distance between the peak and the trough of the potential barrier. Hence due to a difference in forward and reverse jump probabilities a net migration in the direction of the electric field occurs for positively charged ions and vice versa for negatively charged ions. The average ionic drift velocity ν_d can then be described as follows:

$$\nu_d = B\exp\left(\frac{-\Delta H_{mig}}{k_B T}\right)\sinh\left(\frac{|z_i|ea_i E}{k_B T}\right) \tag{2.12}$$

with $B = 4(1-n_i)a_i\nu_0 exp(\Delta S_{mig}/k_B T)$ and n_i being the concentration of the mobile ionic species i [46]. The field dependent ionic drift velocity can be described in two regimes, separated by a critical field strength.

$$E_{crit} = \frac{k_B T}{|z_i|ea_i} \tag{2.13}$$

At small fields $E << E_{crit}$, the drift velocity is proportional to the field $v_d \propto E$. At fields approaching and above the critical field, $E \sim E_{crit}$, the drift velocity becomes exponentially dependent on the field $v_d \propto E_{crit} exp(\frac{E}{E_{crit}})$ [47]. For doubly charged oxygen vacancies in many metal oxides at T = 300K, $|z_i|e = 2$ and $a_i \approx$0.5 nm, the critical field is found to be $E_{crit} \approx 1$ MV cm^{-1}. These field strengths are approached by nano-ionic memories and often lie in the range of dielectric breakdown processes [44].

Applying a high electric field across a thin insulator can result in significant Joule heating and corresponding local temperature increase. Soret thermophoresis describes the diffusion of ions in response to a temperature gradient. Due to a difference in kinetic energy, oxygen ions in a high temperature region will migrate towards cooler regions. Importantly, the opposite occurs for oxygen vacancies, which will accumulate in regions of higher temperatures [48]. The Soret thermo-diffusion is balanced through Fick diffusion, which is a driving force to alleviate concentration gradients [49]. These two thermal forces are the foundation of thermochemical memories (TCM).

2.2 Resistive Switching Mechanisms

The aforementioned physical phenomena can have a strong influence on the leakage current across a thin-film device. Modifications of the polarisation direction, occupancy of charge traps or spatial distribution of ionic defects can elicit a resistance change response.

In the literature, devices with voltage-history-dependent analog resistances are commonly referred to as *memristors*, a compound word from memory and resistors. This concept was first introduced by Leon Chua in 1971, connecting the charge and magnetic flux linkage as a 4^{th} fundamental circuit element on the basis of symmetry arguments, yielding stringent predictions in frequency and current-voltage relations [50]. While reports of hysteretic current-voltage relationships date back as far as 1801 [51], in 2008 Strukov et al connected the concept of memristors to resistance switching in metal oxide thin film devices [52], sparking renewed interest in the field. Chua later extended the definition of the memristor to encompass a much wider range of physical phenomena [53]. In the literature as well as in this thesis, the term memristor is solely used to describe voltage-dependent resistance switching and does not refer specifically to the frequency dependent predictions made by Chua.

The nomenclature adopted here will follow that of reference [54]. A memristor has a high resistance state (HRS) and a low resistance state (LRS). Switching the memristor from the HRS to the LRS is the SET process and conversely the RESET process. The bias is applied to the device with unipolar (only using one voltage polarity) or in bipolar (using both positive and negative bias) sweeps. If the SET process occurs at positive voltage, the device is deemed to display figure 8 wise (8w) switching rotation, while if the SET process occurs at negative voltage, the device displays counter 8 wise (c8w) switching. A memristors order of complexity refers to the number of state variables needed to describe the resistance state of the system. Higher order memristors exhibit more dynamic, time-dependent, resistance states [21]. A specific mechanism can maintain a resistance state for a certain period of time,

the retention, and has a limited number of full switching cycles, the endurance, before the device breaks.

2.2.1 Ferroelectric Mechanisms

Commercial ferroelectric RAM suffers from a destructive read operation, requiring the operator to reprogram the polarisation direction after inspecting the logic state. Using the impact of the ferroelectric polaristion on leakage currents, a resistance-switching memory can be created. Intermediate resistance states can also be stabilised with ferroelectric domains, which makes the ferroelectric memristors particularly promising as artificial synapses in crossbar arrays [55, 56].

In 1994, Blom et al, first reported a resistance change in a thin film ferroelectric material, which was attributed to a polarisation reversal [57]. This effect was termed the ferroelectric Schottky diode (FSD). A 250 nm thick $PbTiO_3$ (PTO) film was sandwiched between Au top and $LaSrCoO_3$ (LSCO) bottom electrodes. Hysteretic leakage current characteristics were proposed to be correlated with polarisation-field sweeps. The system was modelled as a back-to-back Schottky diode, where PTO|Au contact barrier was significantly larger than the PTO|LSCO barrier. The PTO|Au interface was current-limiting. Therefore, changes at the PTO|Au interface governed the overall leakage current. The ferroelectric polarisation modified the barrier profile at each interface. This effect is schematically shown in Fig 2.3 a). The concept of the ferroelectric Schottky diode can be extended to an extreme case, where upon polarisation reversal a rectifying Schottky contact barrier turns Ohmic. Here, a high polarisation, very high carrier concentration and specific band profile are required [58].

Indications of this effect can be found in systems where the ferroelectric is sandwiched by electrodes, which result in high potential barriers at each interface. Here one interface remains blocking, while the other becomes quasi-ohmic, on reversal of the polarisation direction. This effectively allows the change of rectification direction of the capacitor stack by ferroelectric polarisation reversal, commonly termed the switchable diode effect [59–62].

When the thickness t of a ferroelectric material is reduced to be smaller than the depletion region widths (i.e., $t < 2w$), the material becomes fully depleted of electronic charge carriers. In this thickness range, quantum mechanical tunnelling currents become significant. If the remnant ferroelectric polarization can be maintained and the ferroelectric layer is sandwiched between two electrodes of different Thomas-Fermi screening lengths, ferroelectric tunnel junctions can be formed [64, 65]. At nano-scale thickness the depolarising field begins to significantly modify the potential barrier profile of the tunnel junction, as shown in Fig. 2.3 b). The magnitude of the change $\Delta\phi$ in the potential barrier depends on the Thomas-Fermi

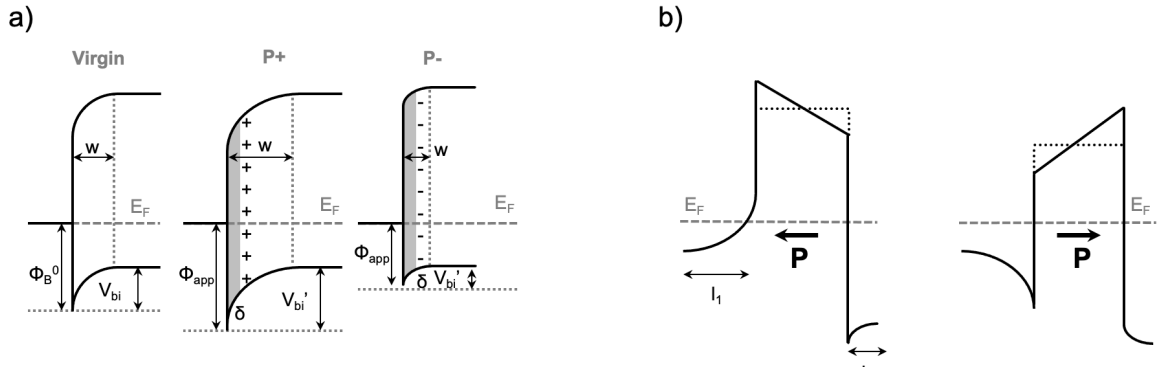

Figure 2.3: a) Influence of polarisation reversal on the barrier height Φ_B^0 and depletion region width w. Fig. adapted with permission from Ref. [63] b) Impact of polarisation reversal on the shape of a tunnel junction. Fig. adapted with permission from Ref. [27]

.

screening lengths, l_i, and the relative ionic permittivity ε of the electrode i, as shown in below.

$$\Delta\phi_i = \frac{l_i Q_s}{\varepsilon_0 \varepsilon_{M,i} e} \tag{2.14}$$

The interface potential will therefore be raised when the polarisation is pointing towards the electrode. Since the potential changes more at the electrode with weaker charge screening, the average potential across the barrier is dependent on polarisation direction as well, as shown by the dotted lines in Fig. 2.3 b). This change in barrier height and widths elicits a polarisation dependent change in conduction current.

2.2.2 Thermochemical Mechanism

The thermochemical mechanism (TCM) describes resistive switching modes, where Joule-heating-induced thermal processes and local reduction govern the formation and dissolution of conductive sub-stoichiometric filaments [48]. The processes are schematically illustrated in Fig. 2.4 a). The switching is unipolar, since electric field only has secondary effects on the filament growth [66]. The RS is initiated by the application of a large voltage stress, which results in a partial dielectric breakdown within the insulator, shorting the two electrodes and setting the device into a LRS [67, 68]. To prevent an irreversible breakdown of the device, a compliance current is used. During the forming and SET process, Joule heating results in a temperature gradient, with which the Soret force causes an accumulation of V_O near the hottest part of the device. This tends to be the tip of a growing filament, leading to a thermal runway effect. The diameter of the filament is governed by the imposed compliance current.

However, in real devices, the time-frame of current compliance lies within the microsecond range, which can lead to the current overshooting, often significantly degrading switching variability [69]. The RESET process occurs by lifting the compliance current and thermally stimulated Fick diffusion opposes concentration gradients and dissolves the conductive filament. Subsequent SET operations are achieved by renewed dielectric breakdown of the material. The SET voltages are typically lower than forming voltages, indicating that the RESET operation does not return the cell into a pristine state and residual stumps of the filament remain. The TCM often co-exists with a valence change mechanism (VCM) through a virtual cathode model [70]. The conductive filament is first formed through the TCM and the eventual resistance change often does not rely on the dissolution of the filament but rather on homogeneous redox processes at the electrode interface [71, 72].

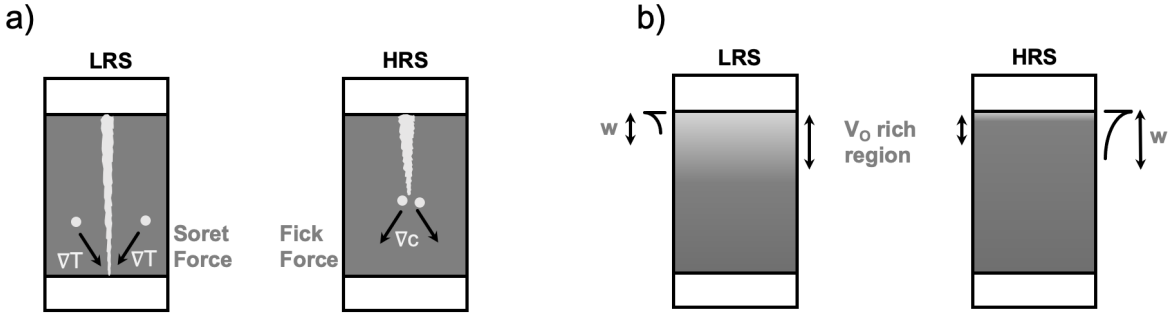

Figure 2.4: a) Filament formation in the TCM b) Interface modification during the VCM. Fig. adapted with permission from Ref. [73].

2.2.3 Valence Change Mechanism

The VCM entails a wide range of bipolar resistive switching modes. It relies on electric-field-enhanced ionic drift in mixed ionic-electronic conductors. In the *"standard"* VCM model, the accumulation and depletion of charged oxygen vacancies near a rectifying Schottky barrier causes a resistance change [74]. An n-type material, which is contacted by a high work-function metal, forms a Schottky barrier. V_O are considered mobile donors. Their presence within a positive depletion region locally reduces the oxidation state of metal cations by donating electron density [75]. The local doping modifies the potential barrier height and width. Even small changes in donor concentration can lead to significant changes in resistance. It is important to note that this vacancy-dependent barrier modification is only appreciable in materials with a high dielectric constant and high dopant concentration [76–78]. Critically, this simplified model is further complicated in materials such as HfO_2, due

the narrow doping range, limiting Fermi level movement [40] and requirement to consider the oxygen chemical potential at the interface for such mechanisms [79].

Nevertheless, numerous methods exist to engineer the material stack towards better switching performance [80, 81]. Considering first the switching layer, a higher ionic mobility is desirable for fast switching and low voltage operation. Yet, this may also negatively impact the retention of a device, due to the voltage-time dilemma [82]. Enhanced mobility can be achieved through increasing tensile strain, increasing V_O concentration or engineering fast diffusion paths. Tensile strain perpendicular to the ionic travel lowers the activation barrier between neighbouring jump sites and increases ion mobility[83–85]. Ionic conductivity of a material is most easily improved by increasing the quantity V_O. This is often performed by either fabricating the switching material under oxygen poor conditions or by annealing the device stack in a reducing environment. However, this process is challenging to control and induces additional electronic charge carriers. An alternative method is to use hypo-valent dopants, such as Y^{3+} substituting Zr^{4+} in the prototypical high-temperature oxide ion conductor Yttria-stabilised Zirconia (YSZ). Yet, studies have shown that a maximum in the ionic conductivity exists, which for YSZ occurs around 8 mol % Y_2O_3 [86]. The thermodynamically stable configuration of V_O is to be sandwiched between two dopant cations [40, 87]. This materialises itself as an additional association energy term, which increases activation energy for ion migration [88]. At low doping concentration, the V_O are separated from dopant cations, whereas at high concentrations V_O begin to form ordered clusters with dopants, eventually limiting conductivity [89]. Finally, enhanced ionic conductivity at grain boundaries through pipe-diffusion has been proposed [90]. Grain boundaries and dislocations act as preferential sites for filament formation [91, 92]. A lower cation density and higher strain have been attributed to enhanced oxygen mobility [93, 94]. This has enabled researchers to engineer grain-boundaries to become the dominant resistive switching path, transporting both ions and electrons [95, 96]. A resulting reduction in electro-forming and switching voltage is consistently observed across material classes [97, 98].

Interfaces are critical lever to tune the performance of memristive devices. The device stacks are typically built with asymmetric electrodes, featuring an active electrode with a current-limiting barrier to be manipulated and an Ohmic interface, which often has a high oxygen affinity to facilitate oxygen exchange. Various electrode parameters ought to be considered to either elucidate or limit parasitic side reactions. A key aspect, which often gets overlooked is the catalytic activity of the electrode. Nobel metals such as Pt, Au and Ir have excellent electro-catalytic properties in the water-splitting cycle. The presence of water is ubiquitous and plays a critical role in modulating the resistance switching response [99, 100]. Paired with a noble metal, volatile resistance switching can occur through oxygen

exchange with the atmosphere by storing residual oxygen in grain boundaries within the electrode [101, 102]. The relative oxide formation energy between the switching material and electrode is another critical factor, as it determines the long-term equilibrium distribution of oxygen and can limit switching endurance [103, 104]. During switching, these electrodes oxidize, creating excess oxygen vacancies in the switching material that increase local carrier concentration. Furthermore, a high kinetic energy during deposition may further increase defect concentrations at the interface, which can improve switching performance. This is often observed in systems grown on Nb-doped $SrTiO_3$ (NbSTO) [105–107]. Finally, the successive oxidation and reduction of an electrode can become the current limiting element [108].

2.3 Materials

2.3.1 HfO_2

The primary material of interest in this thesis is hafnium oxide (HfO_2). It has risen to prominence in the semiconductor industry primarily because of its use to replace SiO_2 as a gate dielectric in MOSFETs. The capacitance of the gate dielectric is an important parameter to control the source-drain current of a MOSFET and therefore key to optimise device performance. The capacitance of the thermally oxidised silicon was successively increased by decreasing the thickness of the dielectric. However, shrinking SiO_2 down to $\sim$1-2 nm led to enhanced leakage currents across the oxide, due to quantum mechanical tunnelling effects. These problems resulted in excessive static power dissipation. Replacing SiO_2 with a thicker material of higher permittivity (high - κ) would decrease current leakage, while retaining a high capacitance. Tertiary ABO_3 complex perovskite oxides tend to have very high dielectric permittivity. However, the stringent requirements for gate dielectric are also high band-offsets (>1 eV) as well as high chemical and thermal stability with respect to silicon [109]. A high silicon band-offset is required to prevent both electron or hole injection into the dielectric and is determined through the bandgap, charge neutrality level and electron affinity. Complex oxides tend to be titanates or tantalates, which have a lower oxide formation energy than silicon. This thermodynamic instability oxidises the silicon underneath, leading to highly defective interfaces, which act as sites for current leakage. These effects are further exasperated by thermal processing at the front end of the line [110]. HfO_2 on the other hand, has a large permittivity, large band-offset and thermodynamic stability with respect to silicon, making it an ideal candidate as a high - κ dielectric [32, 111].

Notably, HfO_2 was discovered to have a ferroelectric phase at the nanoscale [112], which reinvigorated research into ferroelectric non-volatile memories due to its high industrial compatibility. In contrast to commonly used ABO_3 complex oxide ferroelectric materials, such as $Pb(Zr,Ti)O_3$ (PZT), $BaTiO_3$ or $SrBi_2Ta_2O_9$ (SBT), HfO_2 is significantly more silicon compatible, which is particularly important for application as ferroelectric field effect transistors (FEFETs)[113]. However, different to MOSFETs, where amorphous materials are preferred due to a low density of current leakage inducing grain boundaries, ferroelectric materials are required to be highly crystalline. Problems due to poor silicon compatibility, such as the formation of defective silicon interlayers, negatively affect ferroic order [114].

Non-volatile memory devices, such as FeRAM, are not based on MOSFETs and are typically fabricated at the back end of the line (BEOL) and therefore have a strict thermal budget to maintain the integrity of the transistor structure underneath[14]. Perovskite oxide-based ferroelectrics often require high temperature deposition and tightly controlled stoichiometry to generate the high crystallinity necessary to maintain ferroic order. This is commonly achieved by using methods, such as pulsed laser deposition (PLD), sputtering and molecular beam epitaxy (MBE) [77]. These are directional deposition methods and struggle to achieve wide area coverage. Crucially, HfO_2 based materials can be deposited at low temperature by atomic layer deposition (ALD) and are crystallised into the ferroelectric phase through a rapid thermal annealing process (RTA)[113]. Perovskite ferroelectrics are challenging to deposit using ALD due to the highly controlled stoichiometry transfer required. Furthermore, during ALD, the deposited material conforms to more complex device structures, such those in FinFET and gate-all-around (GAA) process nodes [115]. This allows the use of HfO_2 based ferroelectrics to be extended to 3D integration for ultimately scaled storage density [62].

Finally, ferroelectric thickness related effects begin to dominate in the ultra-thin regime. The depolarising field becomes more significant as the thickness of the ferroelectric decreases and is highly dependent on the ability to compensate the polarisation surface charges. Crystalline imperfections, such as dead-layers, grain boundaries or oxygen vacancies, suppress ferroic order. Only perovskite ferroelectric of the highest crystalline quality can maintain a ferroelectric polarisation at nano-scale thickness [116–118]. The previously mentioned problems impose significant constraints on the types of devices that can be developed at commercial scale. An example would be ferroelectric tunnel junctions, which require low thickness and high polarisation [28]. Curiously, HfO_2 maintains its ferroelectric properties at the nanoscale and even increases in polarisation magnitude as the thickness is reduced. Therefore, HfO_2 based ferroelectrics have tremendous advantages over perovskite ferroelectrics in a commercial setting.

How HfO_2 retains its ferroelectric properties in spite of large depolarising fields is a topic of intensive research involving several hypotheses including flat phonon bands[119], coupling to an antipolar phase[120] or an electrochemical state [121, 122]. Moreover, HfO_2 is structurally isomorphic to the well-known oxide ion conductor YSZ [123] and has demonstrated its use in nano-ionic resistive memories [124]. Bulk ceramic HfO_2 exhibits a range of crystal structures. At ambient conditions, the monoclinic (m) $P2_1/c$ phase is most stable. Elevated temperature results in two symmetry-increasing phase transformations into tetragonal (t) $P4_2/nmc$ and cubic (c) Fm3m phases at 1973K and 2600K respectively. Increased pressure first forms an antipolar orthorhombic-I phase Pbca and subsequently a second orthorhombic-II Pnma phase [125]. The high-temperature cubic and tetragonal phases are particularly attractive for applications as high-k dielectrics as the phase transformation is accompanied by increases in permittivity, increasing from $\sim$20 in the m-phase to 24-75 for the t phase [126]. Critically, high-κ *amorphous* phases can be stabilised at room temperature by sputtering through a local cubic-like sub-structure [127]. Doping by hypo-valent rare earth oxides has been particularly successful, as cations occupy substitutional position within the HfO_2 parent lattice. The addition of an aliovalent dopant into HfO_2 is accompanied by a phase transformation as well as an increase in ionic conductivity, with larger cations yielding lower relative increases in ionic conductivity [123, 128, 129].

In 2006, while aiming to enhance the permittivity in HfO_2 thin films by using a Si dopant, Böscke et al discovered a non-linear capacitance – voltage dependency at a dopant concentration between the m and t phase [112]. Extensive structural and electrical characterisation attributed this feature to the stabilisation of a ferroelectric orthorhombic (o) $Pca2_1$ phase. Initially, this came as a surprise and was met with scepticism, since the phase-diagram of HfO_2 was assumed to be thoroughly investigated. A wave of research effort was sparked into the newly discovered ferroelectric properties. The routes towards stabilising the ferroelectric phase are complex and include effects from dopants, electrode strains, thermal history and many more. Interested readers are encouraged to explore the following reviews [130–133].

Among all influences, the role of oxygen vacancies continues to be a topic of considerable debate. It was observed that depositing or annealing doped HfO_2 in a low pO_2 environment, can enhance the fraction of the ferroelectric o phase [131]. Furthermore, unlike perovskite-based ferroelectrics, the positional bistability of one oxygen anion out of two in the unit cell appeared to be a driving factor for ferroelectric polarization. Lastly, polycrystalline ferroelectric HfO_2 devices, which are grown in a multi-phase state, need to be cycled significantly to increase their polarisation, known as the wake-up effect. This has been associated with an oxygen vacancy redistribution and phase transformation from the t $\rightarrow$ o phase [134]. These observations have led researchers to ponder whether the vacancy

migration is fundamentally related to the ferroelectricity observed in HfO_2. A report in 2022 by Yun et al. correlated the degree of structural order with the polarisation magnitude in epitaxial Y-doped HfO_2 (YHO), singifying the intrinsic nature of the ferroelectricity in HfO_2 and excluding the influence of extrinsic surface energy contributions [135]. Furthermore, oxygen vacancy accumulation at the interfaces is often associated with endurance failure. Enhanced endurance at 20K with minimal loss in polarisation magnitude, was used to claim minimal contributions of oxygen vacancies to the ferroelectric polarisation [135]. Conversely in 2023, Kelley claimed that ferroelectricity in HfO_2 can be controlled by a surface electrochemical state [122]. Here a ferroelectric $HfZrO_4$ (HZO) surface was investigated by scanning probe microscopy across a wide range of oxygen partial pressures and temperatures. A rich phase diagram of paraelectric-, antiferroelectric- and ferroelectric-ionic behaviour was observed. The ferroic behaviour was claimed to be inseparable, coupled and even driven by surface electrochemical states [121].

Additionally, in epitaxial films the wake-up effect is minimised. The fabrication of epitaxial films is therefore crucial to resolve these issues. Epitaxial films were first fabricated using a structural analog YSZ substrate and depositing Y-doped HfO_2. This allowed the crystallographic identification of the Curie temperature ∼450 °C [136]. Sn-doped In_2O_3 (ITO) was subsequently used as a bottom electrode to demonstrate a high polarisation of around 30 $\mu C/cm^2$ [137, 138]. Later, significant polarisation was also observed when HZO was deposited on the perovskite $SrTiO_3$/$La_{1-x}Sr_xMnO_3$ system [139, 140]. Curiously, the ferroelectric films displayed a rhombohedral distortion. The large lattice constant, symmetrical and orientation disparity between the bottom electrode and ferroelectric film, pointed toward a complex domain-matching epitaxy [141]. These systems also allowed to deconvolute the beneficial effect of epitaxial tensile strain on the ferroelectric phase stabilisation [142, 143]. Yet, it was soon noticed that the interface chemistry played a significant role. A few monolayer thick, oxygen-deficient interfacial layer seemed to bridge the electrode and the ferroelectric film above. This interfacial layer was correlated to polarisation and could only be obtained using LSMO as a bottom electrode [144]. Furthermore, the interfacial layer proved sensitive to both the La concentration in the LSMO as well as its termination. These were correlated to interfacial redox processes, charge transfer and oxygen partial pressure [145–147].

2.3.2 $La_{1-x}Sr_xMnO_3$

$La_{1-x}Sr_xMnO3$ (LSMO) is the main conductive buffer material used for the growth of YHO in this manuscript. It is part of a family of mixed valence manganites exhibiting collosal magnetoresistance. While magnetic properties will be neglected here, the concomitant

electronic properties of LSMO provide a rich platform to explore various resistive switching modes [148]. The bulk material can be described by a *pseudo-cubic* crystal structure. The Mn ion sits at the centre of an oxygen octahedron, with La or Sr ions occupying the corners of the cube. Due to the octahedral symmetry, the Mn 3d orbitals undergo crystal field splitting into localised t_{2g} and delocalised e_g orbitals. A tetragonal Jahn-Teller distortion further lifts the degeneracy of the orbitals as shown in Fig [149]. Doping the parent compound $LaMnO_3$ with Sr, substitutionally replaces trivalent La^{3+} with bivalent Sr^{2+} ions. The increased hole doping is compensated by a change in the Mn oxidation state from trivalent Mn^{3+} to tetravalent Mn^{4+}, which governs the degree of occupation of the conduction band. At very low and high Sr^{2+} concentration, $0.1 < x$ and $x > 0.5$, the LSMO is in an insulating state. While at x = $\frac{1}{3}$, the ratio between Mn^{3+}:Mn^{4+} is roughly equal and LSMO exhibits a half-metallic state with nearly 100% spin polarisation. A high bulk Curie temperature of 369K is observed which is correlated to both a metal-insulator transition as well as a ferromagnetic-paramagnetic transition [150].

Epitaxial growth of LSMO thin films introduces strain and surface interactions, which have a significant impact on the electronic properties. Any strain, compressive or tensile, away from the bulk lattice parameter of 3.87 Å decreases T_C away from the bulk value[151]. In this work, TiO_2-terminated $SrTiO_3$ (STO) and 0.5 wt% Nb-doped $SrTiO_3$ (NbSTO) are used as substrates for epitaxial LSMO growth. A lattice parameter of a = 3.905, induces a small $\approx 0.9\%$ tensile strain. Notably, interfacing LSMO with NbSTO, an n-type degenerate semiconductor, results in charge transfer across the interface, and electron doping of LSMO. The conducting properties of the LSMO are further deteriorated [152] and a potential barrier forms, affecting charge transport across the heterojunction [153]. The potential barrier is dependent on the substrate termination. SrO-TiO_2 |$La_{1-x}Sr_xO$-MnO, creates a positive charge at the LSMO interface, TiO_2-SrO | MnO_2-$La_{1-x}Sr_xO$ creates a negative charge at the interface. The $La_{1-x}Sr_xO$ terminated interface barrier was found to be larger due to interfacial reconstruction, which resulted in a significant interfacial dipole [154, 155]. LSMO also exhibits a thickness-dependent metal-insulator transition (MIT), where below a critical thickness t_c, the material changes to an insulator. This transition has been associated with a *dead-layer* [156] but may also have an intrinsic origin. Reports of the critical thickness are inconsistent and are highly dependent on preparation conditions. An increase in thickness is also accompanied by a slight change from monoclinic to rhombohedral crystal symmetry [157, 158]. Transport measurements indicated a gradual transition from weak to strong thermally activated electron localisation when the film thickness is above and below t_c respectively. Transport at $t \approx t_c$ showed a transition to two-dimensional transport with Mott variable range hopping [151].

The magnetic and resistance changes of LSMO are particularly useful when integrated into a device geometry. The complex HfO_2|LSMO interface can be leveraged to elicit a resistance-changing response. The screening of ferroelectric polarisation causes the accumulation and depletion of charge carriers, which can lead to a shift in the metal-insulator transition temperature through the ferroelectric field effect [159, 160]. Furthermore, LSMO undergoes a topotactic phase transition between a perovskite and a brownmillerite phase upon a change in oxygen stoichiometry [161, 162]. This phase transition can also be leveraged to observe resistance switching in device configuration [163–165].

Chapter 3

Methodology

Chapter Summary

This chapter describes the various experimental methods used in this manuscript.

The fabrication of a ceramic target is covered and subsequently, it is used to deposit the epitaxial films using pulsed laser deposition. The main principles of the deposition method and how deposition parameters affect film quality are elaborated. Conditions used to deposit and pattern top electrodes using photo-lithography and magnetron sputtering are described. The crystallographic quality is assessed using X-ray diffraction, whereas investigation into surface and piezoelectric properties is performed using scanning probe microscopy. Principles of impedance spectroscopy are covered extensively. Finally, the fundamentals of scanning transmission electron microscopy, cathodoluminescence and photoelectron spectroscopy are elaborated.

3.1 Device Fabrication

3.1.1 Target Fabrication

Ceramic ablation targets for use in the Pulsed Laser Deposition (PLD) system were synthesised using HfO_2 (99.9%) and Y_2O_3 (99.999%) powders from Alfa Aesar. The powders were appropriately weighed, dispersed in iso-propyl alcohol (IPA) and ground to a fine powder using a ball miller. After filtering and drying the milled powder, these were subsequently calcinated at 1000 °C for 6 hours in air. The powder was ground again using a pestle and mortar for 40 minutes and subsequently placed into a die press. The powder was pressed into 2 inch circular targets with 10 tons of weight. The target was finally sintered at 1450 °C for 48 hours. Before each use the targets were polished with 800 grit sandpaper. A powder X-ray diffraction (PXRD) spectrum of two fabricated targets are shown in Fig. 3.1, comparing pure HfO_2 with $Hf_{0.93}Y_{0.07}O_x$ (YHO7). The differences in the target spectra clearly highlight that a solid state reaction and phase change has taken place.

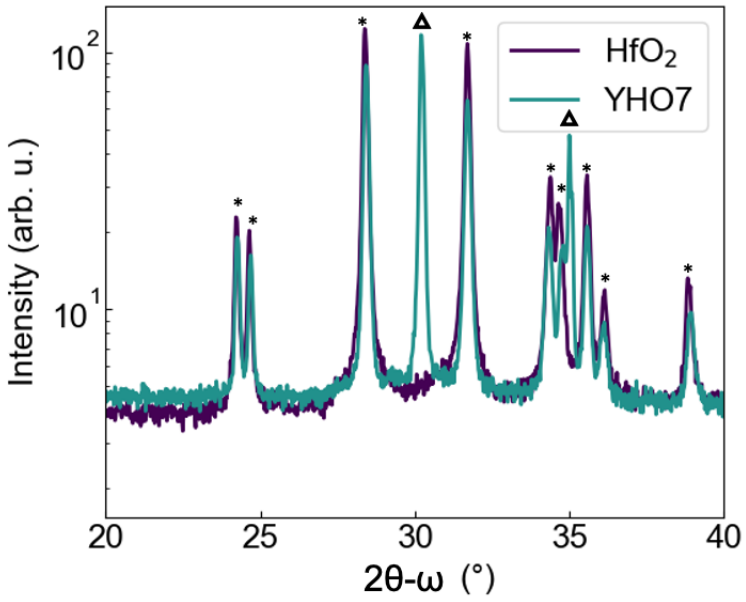

Figure 3.1: Powder X-Ray diffraction spectrum showing two targets. * inicated monoclinic reflections, whereas △ are reflections from o, t or c phases.

3.1.2 Pulsed Laser Deposition

Pulsed laser deposition (PLD) was used to epitaxially deposit LSMO and HfO_2-based films. The deposition setup contains a COMPex Excimer KrF laser, emitting 20 ns 248 nm pulses. These travel through guiding optics until a lens is reached, which focuses the laser onto the target. Laser energy calibration was performed ahead of the lens. The pulse is then focused into a vacuum chamber, containing a target carousel, substrate heater, pumps and gas inlets. Before deposition, the chamber is evacuated to 10^{-6} mbar and the heater, on which the substrate is mounted, is set to 950°C for 90 mintues. This serves to create a well-defined step-edge structure on the surface of a $SrTiO_3$ substrate[166]. The deposition oxygen pressure is then set using a mass-flow controller.

As the laser pulse arrives at the target, it is absorbed and ablates a small quantity of target material, creating a vapour above it. Subsequent interaction of the vapour with the laser pulse creates a plasma, which expands and is propagated normal to the target surface [167, 168]. A high target density is integral to the content of the plasma, since a low density target can lead to particulate ablation and decrease film quality. The target is rotated and rastered to ensure uniform exposure to the incident laser. The fluence is calibrated to exceed the material's ablation threshold significantly, ensuring that the vapour above the target is independent of the material's vapour pressure. Consequently, a consistent stoichiometry transfer is achieved, which is a key advantage of PLD. The fluence governs the quantity of material ejected as well as the kinetic energy of the plume and is therefore an important parameter to adjust.

As the plasma plume expands, it begins to interact with the deposition gas, leading to scattering and decreasing the kinetic energy of the plume on arrival to the substrate. If a reactive gas is used, such as O_2, material in the plasma can form molecular bonds, which aids film stoichiometry. However, it is advantageous to control cation stoichiometry during growth process, while oxygen stoichiometry is tuned after [95]. Importantly, if the deposition pressure is too high, it can lead to the condensation of nano-particles during plasma propagation, which then deposit on the substrate. An alternative method to control the impinging kinetic energy and stoichiometry is to adjust the target-substrate distance.

As the plume arrives at the substrate surface, a high supersaturation is required for condensation of the material from the gaseous phase onto the substrate. By design, PLD has a very high instantaneous deposition rate, but each pulse often only deposits « 1 monolayer of material. The long pause between pulses, governed by pulse repetition rate, allows the adatoms to relax [169]. At sufficiently high substrate temperature, the surface adatom is mobile and diffuses to a suitable binding location. However, if the impinging kinetic energy of the plasma is too high, it can create stresses in the film and potentially resputter condensed atoms. Condensation preferentially occurs at substrate imperfections, such as step edges

or dislocations. For epitaxial growth, single-crystal substrates are used. Yet commercial substrate may not have sufficient surface structure. Chemical and thermal treatments can create large step-structures [166, 170], which guide crystal growth and lead to very high crystal quality.

After film deposition, the chamber is flooded with 300 mbar of O_2, driving it into the film and minimizing oxygen deficiency. The system is then cooled slowly between 1-10 K min^{-1}. Therefore, control over target density, substrate surface structure, fluence, deposition pressure, repetition rate, substrate temperature and cooling procedure is critical to optimise the stoichiometry, energy and rate of impingent ions, which in turn affect the film quality.

3.1.3 Reflection High Energy Electron Diffraction

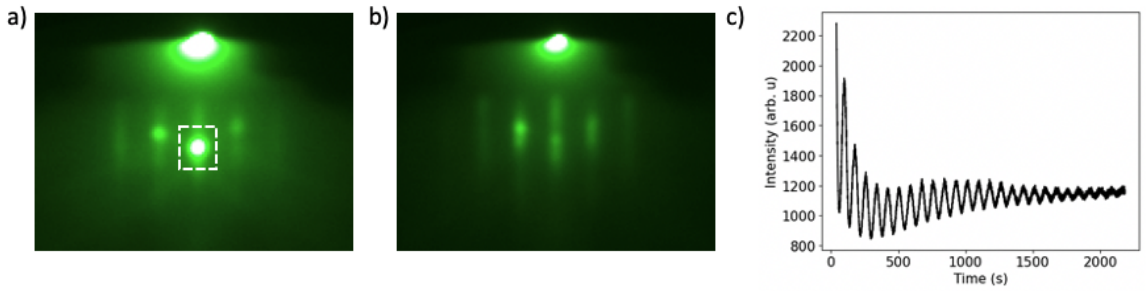

Figure 3.2: Rheed pattern of a) STO, b) LSMO, c) RHEED intensity oscillations of the specular reflection during LSMO growth.

RHEED (Reflection High Energy Electron Diffraction) was used to in-situ monitor the epitaxial growth of LSMO. During RHEED operation, a monochromatic beam of electrons is used at a grazing incidence on the substrate surface. An acceleration voltage of 25 kV and a beam current of 1.5 A were used. Diffracted electrons are captured by a phosphorous screen to yield a 2D diffraction pattern, as shown for STO and LSMO in Fig. 3.2. The diffraction spots are visible as streaks, indicating a smooth surface [167, 171].

Growth monitoring was performed by tracking the intensity change of the specular reflection over time, indicated by the dashed box in Fig. 3.2 a). As the LSMO film is deposited, the intensity of the reflection oscillates, shown in Fig. 3.2 c). Each oscillation corresponds to the growth of a single unit-cell and demonstrates layer-by-layer growth. A peak in the oscillation corresponds to a completed mono-layer, where random scattering is minimised, whereas the trough of the oscillation occurs at half-mono-layer completion, where more of the incident electrons are scattered away from the detector.

3.1.4 Photo-lithography and Contact Sputtering

Micron sized electrodes on top of the film were fabricated by photo-lithography and an AJA magnetron sputtering system. The films were first cleaned by 3 washes with acetone, IPA and deionised water in an ultrasound bath and dried with compressed N_2. Electrode areas were defined by a positive photo-resist process. A spin-coater was used to deposit a thin layer of photoresist (AZ 4533 Merck materials GmbH). The sample was baked at 110°C for 1 minute on a hot plate. Sample was placed on a SÜSS Microtech MJB-3 mask-aligner with a photo-lithography mask, and exposed to UV radiation. After exposure, the sample was placed in a 1:1 water:developer (AZ 351 B, Merck materials GmbH) solution to develop and remove the exposed photo-resist. Samples were then placed into a vacuum chamber and exposed to a sputtering plasma to deposit a variety of electrode materials. The conditions are summarised in Table 3.1 below. Subsequently the devices were placed into acetone to soak overnight and gently sonicated to remove the photoresist.

	Pressure (mtorr)	Power (W)
Ti	2	120
Pt	40	6
Au	40	6

Table 3.1: Summary of sputter deposition parameters of electrode materials.

3.2 X-Ray Diffraction

A range of X-Ray diffraction (XRD) based techniques were used to evaluate the crystallographic properties of epitaxial thin films. These fundamentally rely on how X-ray electromagnetic radiation interacts with periodic and crystalline materials. A Malvern Panalytical Empyrean P2 high-resolution diffractometer was used. Cu Kα radiation with a wavelength of λ = 1.5406 Å is passed through mono-chromators and divergence slits to improve the coherence of the incident radiation and allows for high-resolution acquisition. The system is capable of full 4-circle rotation. Scanning along different angles allows various sections of the Ewald sphere to be inspected. ω signifies the angle between sample surface and X-ray source, 2θ is the angle between detector and the incident beam, ϕ the angle of rotation of the plane perpendicular to the surface normal and χ the angle of rotation of the plane perpendicular to the beam propagation at $\omega = \theta = 0$, as shown in Fig. 3.3.

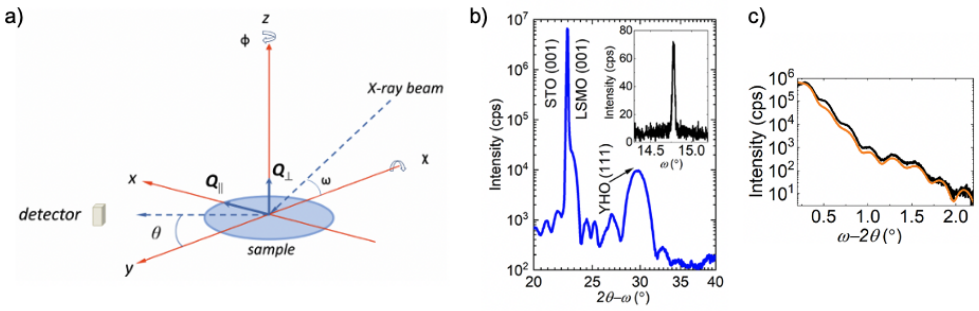

Figure 3.3: a) Representation of the diffractometer goniometer, with permission from [172], b)$2\theta - \omega$ scan oxide heterostructure with ω scan inset c) XRR and fit of an oxide heterostructure. Fig. reproduced from [173].

X-ray Reflectivity (XRR) is used to assess the thickness, roughness and density of a sample [174]. X-ray radiation used in grazing incidence (1-2°), close to and above the critical angle θ_c of total internal reflection, and a coupled $\omega - 2\theta$ scan is performed. An exemplary spectrum is shown in Fig. 3.3 c). X-Rays are reflected both at the surface and interfaces of the thin film, causing interference (Kiessig) fringes. The spacing between these oscillations is inversely dependent on the thickness of the sample. Finally, the intensity of reflected radiation drops sharply with increasing $\omega - 2\theta$, which yields information on both surface and interfacial roughness of the sample [175].

Specular XRD allows the study of the films out of plane lattice periodicity and uses a coupled $2\theta - \omega$ scan. It relies on the Bragg diffraction condition in equation 3.1

$$n\lambda = 2d_{hkl}sin(\theta), \tag{3.1}$$

where n is an integer, λ the wavelength of irradiation, d_{hkl} the separation between crystallographic planes with Miller indices hkl and θ being the Bragg angle. In high-quality films with low roughness, diffraction peaks are surrounded by Laue oscillations, which allow the estimation of the film thickness as shown in Fig. 3.3 b). For samples with grains spanning the film thickness, the 2θ peak width on the other hand can be used to estimate the thickness with the Scherrer equation [176]. Centering the incident X-ray source on a peak and performing a scan along ω, reveals information about the lateral inhomogeneity of the sample, such as grain-size and mosaicity. Similarly, while keeping 2θ and ω in the diffraction condition, a rotational scan along ϕ reveals information about the in-plane orientation of the lattice planes.

3.3 Scanning Probe Microscopy

Scanning probe microscopy (SPM) is a facile method to study topographic, mechanical and electrical properties of surfaces at high spatial resolution. A Bruker Multimode 8 was used for atomic force microscopy (AFM) and piezoresponse force microscopy (PFM) measurements and Gwyddion software was used for analysis. The basic principle of AFM involves the use of a cantilever with sharp, nanometre-sized pyramidal tip which is rastered across a surface. The vertical and torsional motion of the cantilever is tracked by reflecting a laser on the cantilevers surface. The position of the laser is captured by a 4 quadrant photo-diode, where deflection away from the centre forms the basis of the image formation.

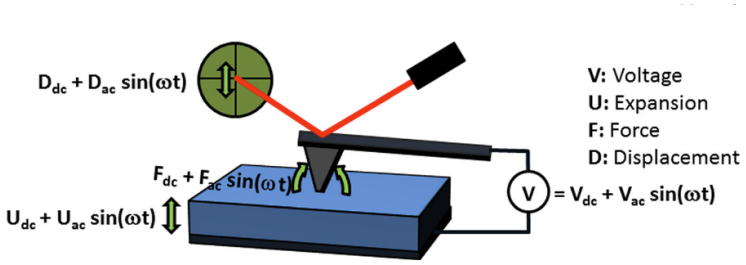

Figure 3.4: Measurement process and tip-surface interaction during PFM, with permission from [177].

AFM is used to study topography and mechanical properties and was invented by Binning Quate and Gerber in 1985 [178]. Here, the tapping mode is used. The cantilever is oscillated by a piezoelectric crystal near its resonance frequency and is only briefly in contact with the sample surface. A feedback mechanism holds the cantilever oscillation at a constant deflection. As the tip comes nearer to the sample surface, van der Waals forces attract the tip closer to the surface until Pauli repulsive forces deflect the tip again. These forces influence the defection amplitude, torsion and lag of the tip oscillation. Feedback correction therefore governs the image formation.

PFM was used to study the piezoelectric and ferroelctric properties of the samples and was developed by Güthner and Dransfeld [179]. In contrast to the AFM tapping mode, here a conductive tip remains in contact with the sample. Fig. 3.4 illustrates the operation of the PFM. A ferroeletric material is investigated by applying an alternating voltage to the cantilever tip and observing the piezoresponse [180]. The amplitude of the signal is related to magnitude of piezoelectric d_{33} coefficient, which is constant across domains and only dips to zero across domain boundaries. Typically, for positive d_{33} coefficients, if the electric field is aligned with the polarisation direction, the domain expands at positive bias and contracts at negative bias. The acquired signal is in phase with the mechanical displacement. In contrast,

if the polarisation anti-aligned to the applied field, a phase difference of 180° is observed and occurs due to the contraction of the domain at positive bias and expansion at negative bias. Pristine films may have undefined multi-domain configurations, hence a DC voltage above the coercive voltage is applied to the cantilever to manually draw domains. In addition to mapping the polarisation, local switching spectroscopy measurements can be performed. It is critical to note that other physical or electrochemical phenomena can give rise to similar signals in PFM and proper care needs to be taken with their interpretation [177, 181].

3.4 Impedance Spectroscopy

Impedance spectroscopy (IS) is a well established technique to investigate thin film oxides. The main advantage of the technique is the ability to separate resistive and capacitive contributions from different components of a device stack [182]. Complementing IS with direct current (DC) conduction analyses can be a powerful combination for the investigation of memristors, allowing the isolation of the resistance switching element and determination of conduction mechanisms. However, this coupling remains underutilised in the literature. The principle of IS lies in the measurement of a frequency spectrum, conversion of raw data into impedance, visualisation of the data through different formalisms and lastly attribution of features and fitting of data through equivalent circuit modelling.

In an IS experiment, a metal oxide thin film, sandwiched between two electrodes, is excited with an alternating voltage, U_t, with amplitude U_0 and angular frequency ω in a small-signal, linear and reversible regime. An alternating current, which is retarded by the phase angle θ is measured by an impedance spectrometer. The excitation frequency is then swept, typically between 10 Hz - 1 MHz.

$$U_t = U_0 sin(\omega t) \tag{3.2}$$

$$I_t = I_0 sin(\omega t + \theta) \tag{3.3}$$

The complex impedance Z_ω is obtained by the ratio of the Fourier-transform $\hat{U}_\omega$ of the voltage U_t and the Fourier-transform $\hat{I}_\omega$ of the measured current I_t.

$$Z_\omega = \frac{\hat{U}_\omega}{\hat{I}_\omega} = Re(Z'_\omega) + i \cdot Im(Z''_\omega) \tag{3.4}$$

$$\theta = tan^{-1}(Z''/Z') \tag{3.5}$$

The real, Z', and imaginary, Z", parts of the impedance describe the resistive and reactive contributions respectively. The reactive contribution can be further separated into capacitive (θ = -90°) and inductive (θ = 90°) components, whereas the resistive contribution has no phase shift (θ = 0°).

Physical conduction processes or system components give rise to certain features in the impedance spectrum. These features are often modelled and represented through idealised equivalent circuits. Serial and parallel combinations of resistors, capacitors and more advanced elements are arranged and fitted to the experimentally acquired dataset. Herein lies the fundamental challenge in interpreting impedance spectroscopy data. The *correct* choice of equivalent circuit can often oversimplify the underlying physics or easily overfit existing data. However equivalent circuit fits are often necessary to make quantitative arguments about the system under test. In the field of ceramic metal oxides, the primary physical processes visible within the measured frequency range are often grain, grain-boundary and interface region impedances. The equivalent circuit adopted for this is the 'Bricklayer model', developed by Bauerle [183]. Each of these components is modelled as parallel RC elements connected in series, as shown in 3.5 a). As film thickness is reduced, the grain size becomes of

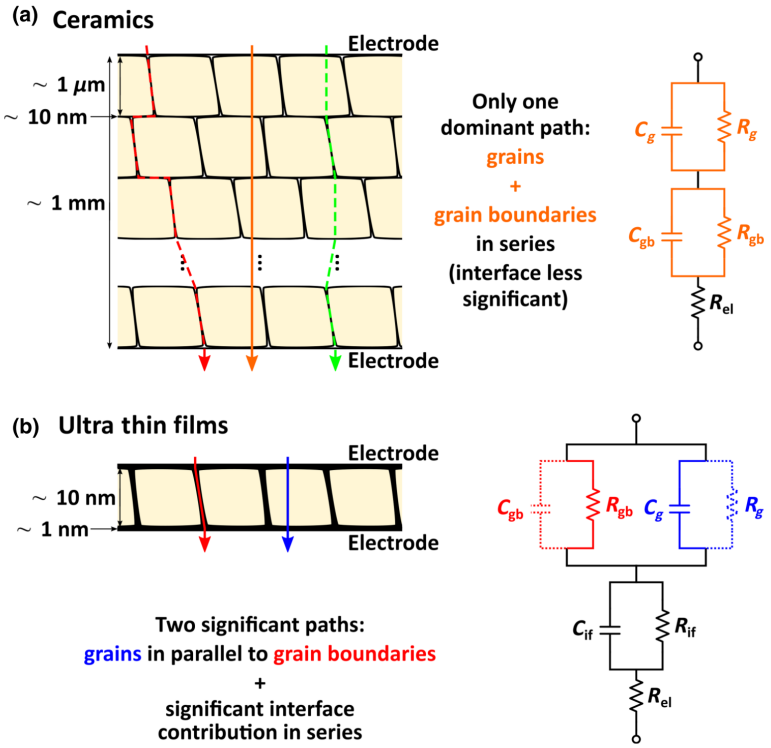

Figure 3.5: a) Bricklayer model for the impedance elements in ceramics b) impedance elements for ultrathin films, with permission adapted from [184].

similar magnitude to the film thickness, such that no grain boundaries of the metal oxide exist perpendicular to the current path, as shown in 3.5 b). Therefore, grain and grain-boundary contributions to the impedance are represented to be parallel to each other rather than in series. In practise, however, two parallel RC components cannot be isolated or distinguished from each other. Furthermore, in thin films, the space-charge impedance of interfacial layers becomes significant.

Considering now an ideal non-disperse model system, we take the hopping conduction of ions within a solid electrolyte across potential wells in the direction of an electric field [185]. We assume that the potential wells are evenly spaced and are of equal height. Consecutive hops are only dependent on temperature, electric field and the shape of the potential barrier. The hopping process gives rise to a single relaxation time constant τ and is related to the parallel combination of a resistance R, $Z_R = R$, and capacitance C, $Z_C = \frac{1}{i\omega C}$ by equation 3.6, where f_0 is the relaxation frequency.

$$\tau = \frac{1}{2\pi f_0} = RC \tag{3.6}$$

The relaxation is visualised through the Bode plot Fig. 3.6 a), which displays the frequency dependence of the real part *Z'* and imaginary part *Z"* impedance. A number of features are relevant. First, the resistance plateau in *Z'* at low frequency corresponds to R. Second, the peak in the *Z"* corresponds to the relaxation frequency f_0 and the frequency dependence of the Z" follows a power-law with a relation of $Z \propto f^n$, where $n = 1$.

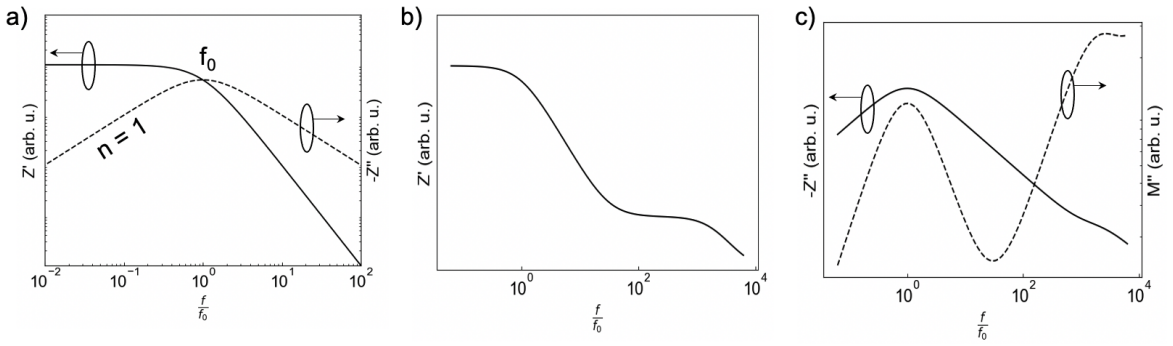

Figure 3.6: a) Bode plot of Z' and Z" for single relaxation b) Bode plot of Z' for two relaxations c) Combined Bode plot of Z" and M" for two relaxations.

Systems often have more than a single relaxation, which is convoluted with the first relaxation, as shown in fig 3.4 b). Data visualisation through the complex electric modulus formalism can yield additional information. The modulus formalism emphasizes the relaxation with the smallest capacitance and is dependent on the empty cell capacitance C_0 and complex impedance Z^* through $M^* = 2\pi f i C_0 Z^*$ [186]. Combined plots of *Z"* and *M"* can

therefore reveal the largest resistance and smallest capacitance respectively, illustrated in 3.6 c).

Real systems however rarely behave in this idealised manner. Critically, the conductivity and permittivity tend to be frequency dependent, which is not taken into account above. These non-idealities reveal themselves in power-law frequency dependent behaviour of AC conductivity, permittivity or changes in slope of *Z"*. Early reports of this behaviour originate from the Curie-von Schweidler behaviour, which examined the power-law dependent relaxation of polarisation [187]. Jonscher consolidated the power-law behaviour observed in a wide range of systems such as disordered networks, amorphous semiconductors, hetero-junctions and dielectrics, under the *universal dielectric response* [188]. This was a phenomenological model based around the frequency-dependent susceptibility and conductivity $\sigma_{AC} = \sigma_0 + A\omega^n$ with the exponent being $0 < n < 1$. These non-idealities could be described for by the constant phase element (CPE), which is linked to a random network of RC components [189]. It describes an artificial circuit element between a resistor and capacitor. The exponent α represents the constant phase and is a free parameter between 1 (θ = 90°) and 0 (θ = 0°).

$$Z_{CPE} = \frac{1}{Q_0(i\omega)^\alpha} \tag{3.7}$$

The CPE is most often used in accounting for diffusion impedances [190, 191] or fractal roughness of electrodes [192] and even ferroelectrics [193]. However CPE is not based on a microscopic theory.

Ferroelectric materials exhibit *Rayleigh behaviour*, which refers to the analogy between the behaviour of magnetic domains in a magnetic field to ferroelectric domains in an electric field [184]. It describes the linear dependence of the permittivity on the applied electric field through the centre of mass motion of domain walls. Individual segments of the domain wall can be pinned at defects and interfaces and give rise to a logarithmic frequency-dependent permittivity. An equivalent circuit element, the domain wall pinning element Z_{DW} was developed by Becker et al. [194, 195], which allows the explicit study of domain wall motion in a ferroelectric and can be extended to inter-phase boundaries. The domain wall pinning element is determined through equation 3.8 and uses the static real and imaginary part of the relative permittivity, $\varepsilon'_{r,0}$ and $\varepsilon''_{r,0}$, as well as the logarithmic dispersion strength $\Delta\varepsilon'_r$ as free fit parameters.

$$Z_{\mathrm{DW}}(f) = \frac{\varepsilon''_{r,0} - i\left[\varepsilon'_{r,0} + \Delta\varepsilon'_r \ln\left(\frac{1\,\mathrm{Hz}}{2\pi f}\right)\right]}{2\pi f C_0 \left\{\left[\varepsilon'_{r,0} + \Delta\varepsilon'_r \ln\left(\frac{1\,\mathrm{Hz}}{2\pi f}\right)\right]^2 + \varepsilon''^2_{r,0}\right\}} \tag{3.8}$$

3.5 Transmission Electron Microscopy

3.5.1 STEM

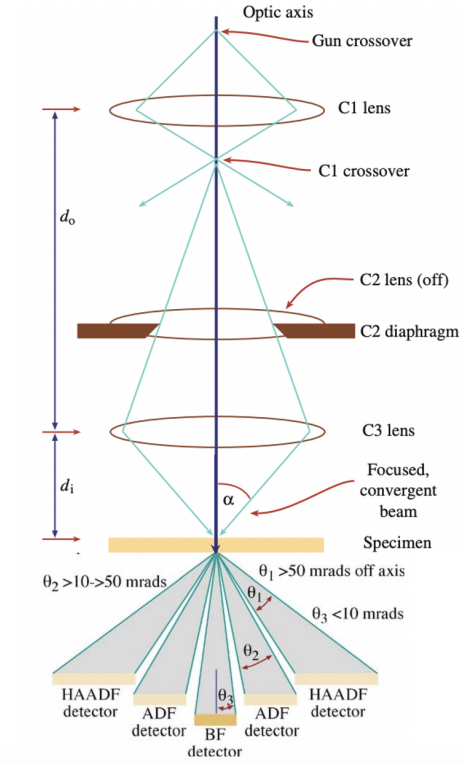

Figure 3.7: Components of a scanning transmission electron microscope, with permission adapted from [196].

Scanning transmission electron microscopy (STEM) is an imaging technique that allows to characterise materials with atomic-scale resolution. In this thesis, a probe-corrected ThermoFisher Spectra 300 operating at 300kV with a Gatan Continuum EELS spectrometer was used. A high energy coherent electron beam is focused through magnetic lenses to a sharp convergence angle, as illustrated in Fig 3.7. The resulting beam is scanned across the specimen to gain spatial resolution. The specimen needs to be thin enough to be electron-transparent. Electron detectors are distributed radially from the optical axis. Detectors at different scattering angles allow different imaging techniques to be used, enabling the separation of contrast modes. The bright-field detector lies directly on the optical axis and captures transmitted electrons. Often, this detector is ring-shaped and the primary electron beam is transmitted for other measurement modes. At higher scattering angles, annual dark field detectors capture Bragg-(elastically scattered) diffracted electrons. Finally, high-angle annular dark field (HAADF) detectors capture incoherent Rutherford scattered electrons.

The scattering contrast here is directly related to the atomic number Z^2 and is excellent for imaging heavy atoms[196].

3.5.2 EELS

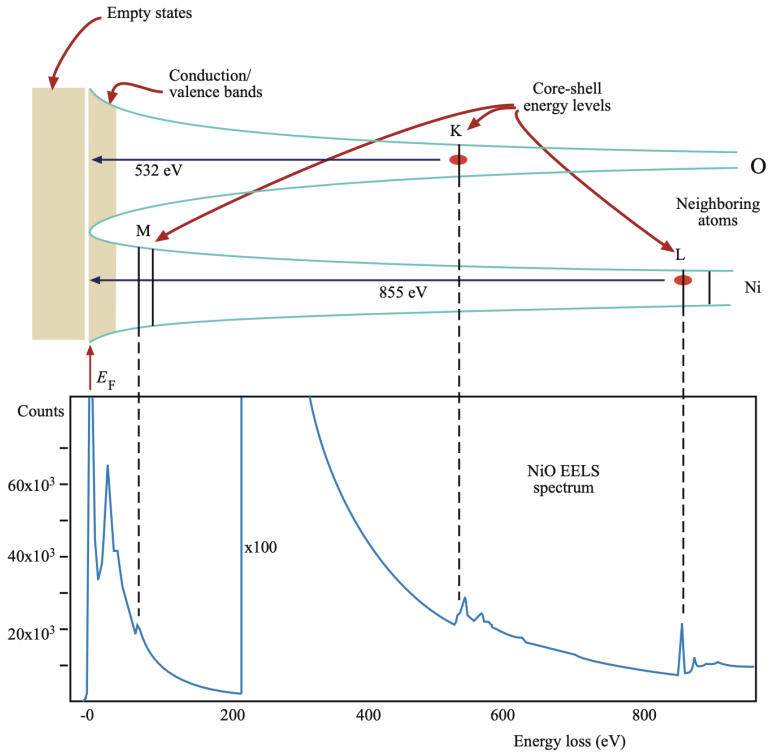

Figure 3.8: NiO EELS spectrum with corresponding electronic transitions, with permission from [196].

Electron energy loss spectroscopy (EELS) is a powerful technique to investigate the chemical properties of atomic orbitals. It is used complementarily to STEM, where the primary electron beam optical axis is captured after being inelastically scattered by the sample lamella. High energy beam of electrons interacts with core-shell electron orbitals of the lamella. These are excited to higher energy levels, whereas the electron beam loses energy, characteristic of the atomic transition. This energy loss is the key measurement principle behind EELS. The excited electrons can de-excite and emit an X-ray photon or eject another (Auger) electron in the outer electron shell, which are the basis for energy-dispersive X-ray spectroscopy (EDX) or Auger electron spectroscopy.

The energy loss spectrum contains three primary regions, as illustrated in Fig. 3.8 for an exemplary NiO spectrum. The first region contains the most intense section of the spectrum,

the zero loss peak (ZLP). As the name suggests, these are electrons which have not been scattered by the sample lamella and hence experienced no loss in energy. The position of the ZLP serves as an energy calibration and the full width half maximum (FWHM) is used as an indication of the energy resolution. Finally, using the ratio of the ZLP integrated intensity I_0 over the integrated intensity of the total spectrum I_t, gives an estimate of the number of scattering events per incident electrons, known as the ratio-log technique.

$$\frac{t}{\lambda} = -\ln(\frac{I_0}{I_t}) \tag{3.9}$$

Here $\frac{t}{\lambda}$ gives the ratio of the lamella thickness t and the electron inelastic mean-free path λ [197]. Plural scattering events can significantly convolute the data analysis of the low-loss and core-loss regions. Therefore, thin lamellas with $\frac{t}{\lambda} < 1$ are preferred.

The low-loss region typically contains energy losses of up to 50 eV. Within this region, losses originate from loosely bound outer shell valence/conduction electron density. Therefore, it is used to investigate the bandgap, dielectric function and inter-band transitions. The most prominent signal within this region is the plasmon peak, which originates from oscillations of weakly bound electrons. This oscillation occurs at a specific plasmon energy E_p and is dependent on the conduction/valence electron density n.

$$E_p = \sqrt{ne^2h/\pi m} \tag{3.10}$$

Here e is the elementary charge, h the Planck constant and m the effective electron mass. Shifts in the plasmon peak are particularly useful for examining electronic changes across a sample. Finally, the core loss region examines inner shell transitions, where the near edge fine structure (chemical states) can be investigated $\geq$50 eV from ionisation edge. Transitions in this region are characteristic for each element and are used for chemical fingerprinting. The integrated intensity of each of the core losses can be related to the relative concentration of the element. However, the signal intensity decreases with a power law, which needs to be removed as a background before quantification. Furthermore, changes within a single peak across a sample can be investigated to study chemical changes. For example, chemical shifts can indicate changes in local electron density. Differences in relative peak intensities within a specific core loss can suggest different orbital occupations.

3.6 Cathodoluminescence

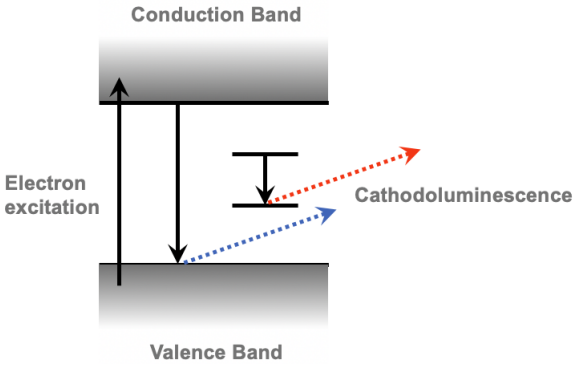

Figure 3.9: Electron excitation and subsequent photon emission process

Cathodoluminescence is a phenomenon where the emission of light occurs upon the irradiation of a material with a high-energy electron beam (0.1-300 keV). The primary electron beam carries too much energy to directly excite electrons into the conduction band. These are therefore inelastically scatted, giving rise to secondary electrons, X-Rays and Auger electrons. The secondary electrons in turn excite electrons into the conduction band, as schematically illustrated in Fig. 3.9. From the conduction band, the electrons can decay radiatively to a lower energy level and recombine with a hole state, emitting a photon of characteristic wavelength. The decay can occur either directly from the conduction band to the valence band (band edge emission) shown in blue or through in-gap states, shown in red, similarly to photoluminescence [198].

In contrast to photoluminescence, the advantage of cathodoluminescence is that it is not limited by the incident laser wavelength and is therefore particularly suitable to study wide band-gap insulators. Furthermore, changing the acceleration voltage and beam current modifies the interaction volume of the electron beam. This therefore allows the confinement of luminescence emission and is particularly suited to study ultra-thin films. A FEI-XL30 FEGSEM with a Gatan MonoCL cathodoluminescence system was used in this work.

3.7 Photoelectron Spectroscopy

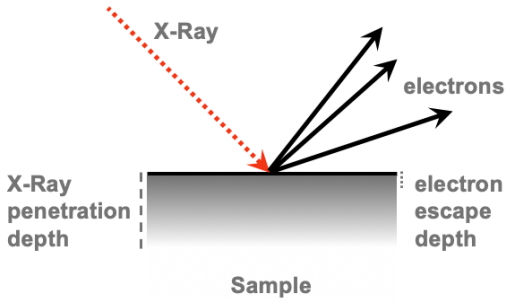

Figure 3.10: Photoelectric effect and XPS sampling depths

X-ray photoelectron spectroscopy (XPS) is a surface-sensitive technique based on the photoelectric effect, which provides chemical information about a sample. During measurement, a material surface is illuminated by X-Rays, which are absorbed and cause the emission of an inner-shell photoelectron. The photoelectron then travels towards the surface of the material and is scattered, depending on the inelastic mean free path. Once the photoelectron reaches the surface, it escapes the material with kinetic energy, E_{KE} and is detected after passing through collection lenses. The binding energy E_{BE} is characteristic of specific elements and depends on the incident X-ray energy $h\nu$, the detector workfunction φ and E_{KE}.

$$E_{BE} = h\nu - E_{KE} - \varphi \tag{3.11}$$

Similarly to ELNES, relative shifts in E_{BE}can suggest changes in the nearby charge density. We differentiate between a rigid binding energy shift, that is a shift of all valence bands and all core levels of the insulator by the same value indicative of an internal electric field, from chemical binding energy shift, an individual shift specific to of a core level indicative of a change in the local electronic structure due to chemical bonding. Furthermore additional peaks can appear, which signify different bonding environments or changes in oxidation state. These are often convoluted with the original peak. XPS analysis therefore often relies on a model, where Shirley backgrounds are removed from the signal and individual peaks are fitted with Voigt functions [199]. The shallow penetration depth of XPS severely limits its application to study oxide heterostructures, see Fig. 3.10. Buried interfaces in real devices are also experimentally accessible using the hard X-ray variant of photoelectron spectroscopy (HAXPES) at higher photon energies, increasing the information depth up to several tens of nm [200, 201].

Hard X-ray photoelectron spectroscopy (HAXPES) uses energies in the range of 5.9 keV in contrast to the commonly used 1.4 keV used in lab-based XPS. In this thesis, HAXPES experiments were performed at the Diamond beamline I09.

Chapter 4

A Schottky-to-Ohmic Transition in Epitaxial Ferroelectric Hafnia Devices

Chapter Summary

This chapter describes the growth, structural characterisation and current-voltage response of an epitaxial hafnia-based capacitor stacks. Evidence of high-quality epitaxy and a rhombohedral distortion in the HfO_2 film are presented. Piezo-response force microscopy strongly suggested the presence of ferroelectricity within the film. A resistance switching mode of the device stack is demonstrated showing a high on/off ratio, which was termed a Schottky-to-Ohmic transition and is investigated extensively during the remainder of this manuscript. Voltage-pulse based measurements demonstrated both synaptic and neuronal functions of the switching mode. A model linking ferroelectricity with the observed memristive behaviour is proposed and is based on polarisation dependent interface barrier modification.

The results of this chapter have been published in Ref. [173]:

M.L. Müller, M.T.Becker, N. Strkalj, J.L. MacManus-Driscoll. "Schottky-to-Ohmic switching in ferroelectric memristors based on semiconducting $Hf_{0.93}Y_{0.07}O_2$ thin films." Applied Physics Letters **121**, 9 (2022)

Author Contributions

PLD growth was performed by me. XRD and PFM were performed by Nives Strkalj and me. Electrical characterisation was performed by Maximilian Becker and me.

4.1 Introduction

Resistance switching (RS) memory devices based on metal oxides have been found to be useful in mimicking the electronic functions of the brain's synapses and neurons [14]. Voltage pulses, which emulate action potentials, applied to these devices elicit a change in resistance, which may be time or rate-dependent, and are governed by the devices' order of complexity [21]. Such neuromorphic approaches applied to computing promise a low-power, inherently parallel, alternative to current computing hardware paradigms. A promising class of RS systems are devices based on ferroelectric materials. Their bistable, voltage-switchable polarisation is a natural candidate for memory applications. If confined into the ultra-thin regime (<5 nm) and sandwiched by two asymmetric electrodes, a ferroelectric polarisation reversal modifies the potential barrier and therefore the tunnelling current and device resistance [27, 64]. Gradual changes in resistance can be achieved through the application of sub-coercive voltage pulses, which partially switch the polarisation through ferroelectric domains. These device stacks can therefore be exploited as synapses in neuromorphic computing systems [202].

Stabilising ferroelectricity at the nano-scale is challenging. Ineffective screening of the polar surfaces and the resulting influence of the depolarisation field can distrupt ferroic order. At these length scales, ionic defects begin to play a noticeable role in governing electrostatic boundary conditions [203] and therefore also transport properties. Electrochemical surface states have been shown to couple to ferroelectric polarisation, creating newly proposed ferroionic states [204]. Furthermore, anionic migration can become significant in ultra-thin films and at high fields, leading to an additional contribution to electro-resistance [164]. An additional ionic degree of freedom may allow control over other physical properties such as magnetic or optical characteristics [205], leading to a rich set of physical coupling phenomena that are presently not well understood. In the context of neuromorphic computing, the presence of both ferroelectric and ionic degrees of freedom can lead to the reversal of the electro-resistance sign [206] and add further time-dependency in the resistance change kinetics[206, 207]. It therefore may be attractive to design ferroelectric systems with high ionic conductivity [208] to explore and exploit such coupling.

HfO_2 has emerged as a promising candidate for RS non-volatile memory applications, primarily due to its compatibility with complementary metal oxide semiconductor (CMOS) process technology as a high κ dielectric. The discovery of its ferroelectric properties at the nanoscale reignited interest in ferroelectrics [112]. However, the mechanisms by which the material maintains ferroelectric properties at the nanoscale and tolerates high depolarisation fields remain unclear [132, 133]. Electrochemical effects, particularly oxygen deficiency have been shown to play an important role in stabilising the ferroelectric phase, as discussed

in section 2.3. Enhancing the oxygen ionic conductivity of HfO_2 through aliovalent doping and utilising a bottom electrode, which is highly sensitive to changes in stoichiometry, may be an effective route to elucidate and couple ferroelectric and electrochemical effects.

An ultrathin epitaxial 0.5 wt. % Nb doped $SrTiO_3$| $La_{0.67}Sr_{0.33}MnO_3$| $Hf_{0.93}Y_{0.07}O_x$ heterostructure is presented, whose transport characteristrics were studied using Ti|Au top electrodes. YHO exhibited a polar phase with a rhombohedral distortion and we demonstrated the ferroelectric properties of the film through piezoresponse force microscopy (PFM). We observed significant resistance switching hysteresis and propose that this effect is due to polarisation reversal and its effect on the occupancy of defect-induced charge traps.

4.2 Experimental Methods

The epitaxial thin films were fabricated by pulsed laser deposition (PLD). Two ablation targets for PLD were synthesised. The target with composition $Hf_{0.93}Y_{0.07}O_x$ was prepared as described in section 3.1.1 by mixing HfO_2 and Y_2O_3 powders. A $La_{0.67}Sr_{0.33}MnO_3$ (LSMO) was synthesised similarly. Powders of $LaCO_3$, $SrCO_3$ and MnO were ground and mixed in the appropriate ratios. Calcination was performed at a temperature of 850°C and sintering at 1200°C. In this study, 0.5 wt. % Nb-doped $SrTiO_3$ (NbSTO) single crystals with (001) orientation from Crystech GmbH were used as substrates. Before deposition, the substrates were annealed at 950°C for 1 hr at a pressure of 10^{-6} mbar to obtain an ordered step-terraced surface structure. LSMO film with a thickness of 11 nm was deposited as a conducting buffer layer at a temperature of 750°C and pressure of 0.133 mbar O_2. The laser pulse fluence and repetition rate were set to 1.5 J/cm^2 and 2 Hz respectively. The progress of the LSMO deposition was tracked using RHEED, see section 3.1.3. YHO film with a thickness of 4.5 nm was deposited at 890°C and 0.1 mbar O_2, using a fluence of 1.2 J/cm^2 and rate of 2 Hz. After the deposition, the chamber was flooded with 400 mbar O_2 and cooled slowly to room temperature at 5K/min. Top electrodes were fabricated by a photolithographic process and magnetron sputtering, as described in section 3.1.4 and consisted of a 2 nm Ti adhesion layer on which 50 nm thick Au was deposited.

4.3 Structural Characterisation

The crystalline quality of the thin films was assessed using high resolution X-ray diffraction (XRD). Fig. 4.1 a) shows a scan along 2θ-ω, displaying lattice spacing induced Bragg reflections. The most intense signal at 22.7° originates from the STO (001) diffraction. At a slightly higher angle, 23.0°, the LSMO (001) is visible, whereas a (111) reflection is

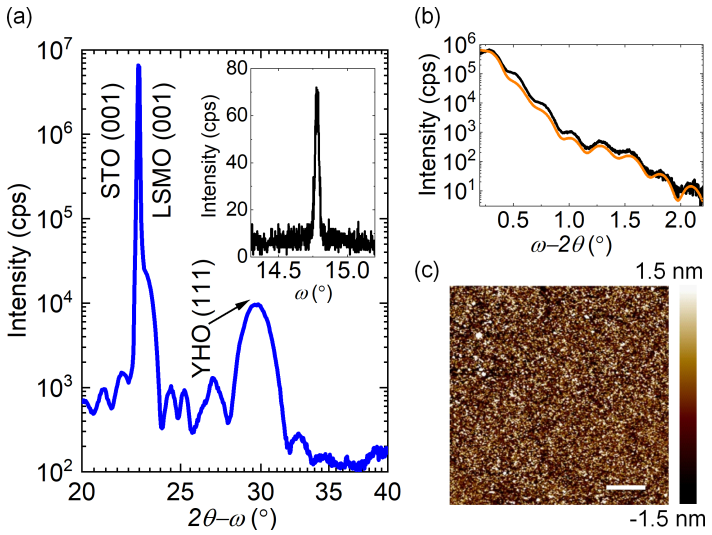

Figure 4.1: Crystallographic and surface characterisation of the epitaxial LSMO|YHO heterostructure a) 2θ-ω XRD scan, inset showing a rocking curve scan along ω b) XRR measurement (black) and fit (orange) c) tapping mode AFM measurement of the surface, scale bar is 1 μm. Fig. reproduced from [173].

present for YHO at 29.9°. This (111) YHO reflection occurs at a slightly lower angle than observed in the orthorhombic phase, 30.1°, in polycrystalline films [112] and those grown on YSZ(111)|ITO [209]. This could suggest a buffer-layer strain-induced rhombohedral distortion is present, as reported previously for similar device stacks [139, 210, 211]. Laue oscillations are observed beside the main reflections, indicating a very high crystalline quality and a low surface roughness in the investigated films. A rocking curve around the YHO (111) reflection was obtained, see the inset of Fig. 4.1a). The full width half maximum (FWHM) of the peak was 0.0367°, indicating a high lateral coherence length and low degree of mosaicity, ie. a small degree of tilt of the out of plane orientation with respect to the substrate. On the same system with different layer thicknesses, Yun et al observed [210] the existence of a sharp and broad peak in the rocking curve, which corresponded to high and low crystallinity regions in the sample. The broad peak was not observed in this study, indicating high crystalline quality of the sample.

The thicknesses of the layers were confirmed by fitting X-ray reflectivity (XRR) data using the Panalytical X'Pert Reflectivity Software, see Fig. 4.1 b). The layer thickness analysis yielded 11 nm for LSMO and 4.5 nm for YHO. The root mean square surface roughness was calculated be 0.5 nm, verified by a roughness of 0.8 nm observed using atomic force microscopy (AFM), see Fig. 4.1 c). The surface topography displays the slightly granular texture, which originates from the large symmetry mismatch between LSMO and YHO and hence resulting in complex domain-matching epitaxy between the two films.[141]

The YHO epitaxy present here, while displaying a high crystalline quality, does contain a small degree of periodic incoherence through grain, domain or orientation boundaries. A detailed structural analysis using electron microscopy follows in section 5.5.

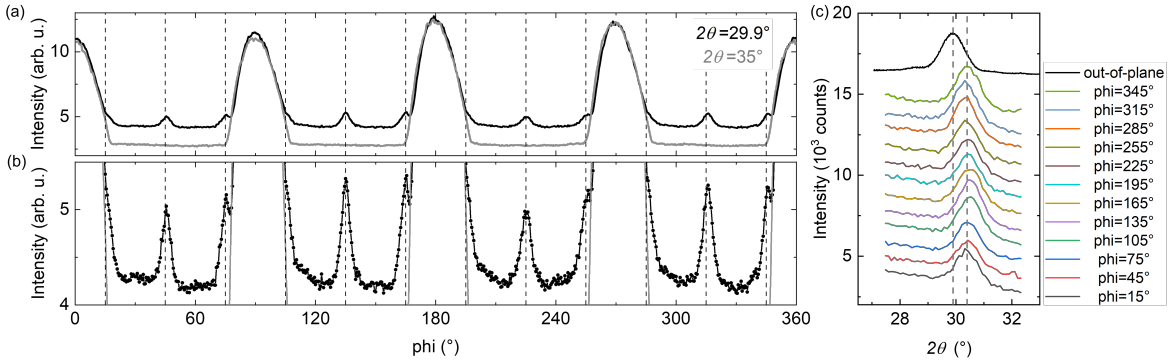

Figure 4.2: Orientation and texture analysis of the heterostructure a) ϕ-scan at χ=71° and 2θ= 29.9° (black) and 35°(grey) b) zoomed in ϕ-scan highlighting the 12 fold in-plane symmetry of the YHO c) 2θ scan across each peak in ϕ. Fig. reproduced from [173].

Further insight into the texture and orientation of the heterostructure was gained by following the guidelines presented in [143, 212]. We fabricated an equivalent device with a 9 nm thick YHO film instead to increase the diffraction signal. In our laboratory setting, we used an X-Ray line source, which resulted in significant background signal within the scan. To account for the background, we performed a ϕ scan at 2θ = 35°, where no material reflection is expected, see Fig. 4.2 a) in light grey. A rhombohedral distortion is a lattice angle change away from 90° in the case of a cubic parent lattice and can be thought of as the expansion or compression of a unit cell along the (111) diagonal. This manifests itself as a disparity in d-spacing among the family of (111) lattice planes. In-plane domains can be accessed by performing a ϕ scan. For a (111) oriented film, 3 in-plane reflections for (-111), (1-11) and (11-1) domains are expected at an angle of χ = 71° away from the out-of plane reflection. We therefore perform a scan along ϕ with 2θ = 29.9° and χ = 71°. Instead of 3 reflections, 12 evenly spaced reflections are observed. These stem from the four-fold symmetry of the STO(001)|LSMO(001) buffer system, and arise due their symmetry mismatch with the (111) oriented YHO [141]. The in-plane d-spacing was assessed by performing a scan along 2θ for each reflection, as shown in Fig. 4.2 c). The in-plane reflections have a consistent 2θ = 30.3°. The lattice spacing is, therefore, significantly larger out-of-plane than in the in-plane direction. This is clear evidence of a rhombohedral distortion present in this film, an expansion of the unit cell in the out-of-plane direction. The degree of the rhombohedral distortion α is calculated to be $\alpha = 2 * atan(\frac{d_{-111}}{d_{111}})$ = 89.26°.

4.4 Scanning Probe Microscopy

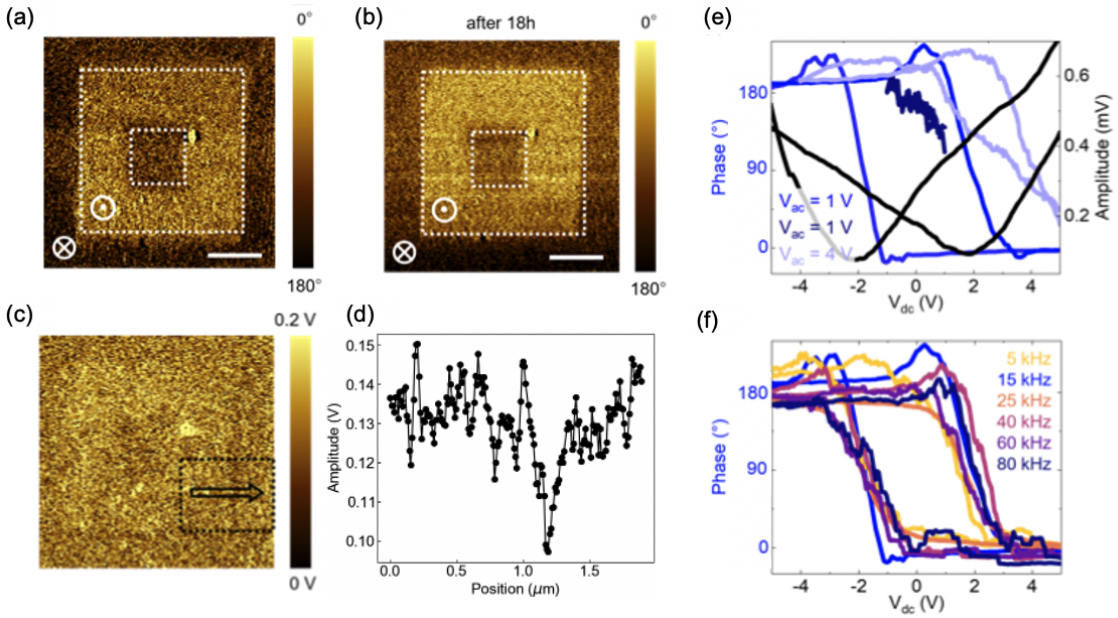

Figure 4.3: Scanning probe microscopy evaluation of the samples piezoresponse a) PFM phase measurement of the drawn square-in-square pattern showing in and out of plane polarisation b) PFM phase square-in-square pattern after 18 h c) PFM amplitude d) averaged linescan showing dip in amplitude profile at ferroelectric domain wall e) amplitude and phase switching spectroscopy at varying V_{DC} and V_{AC} f) measurement frequency dependent phase measurement during switching spectroscopy. Fig. reproduced from [173].

To check whether ferroelectricity is present in the YHO films, we carried out extensive PFM measurements. To assess whether the thin film is ferroelectric, we perform piezo-response force microscopy (PFM) [177, 181, 213]. A DC bias, V_{DC} is applied to the sample, while the SPM tip is grounded and subsequently rastered across the surface to write a domain pattern. An alternating bias, V_{AC} = 1V, of frequency f = 15 kHz is applied to record the piezoresponse of the pattern. Fig. 4.3 a) shows a square-in-square pattern of the recorded phase signal, which was written with V_{DC} = +6V and -4V for the outer and the inner square, corresponding to the polarisation pointing up and down respectively. A clear 180° phase difference is evident between the two squares, which is stable for at least 18 hours, see Fig. 4.3 b). An indication of electrostatic charging is visible in the amplitude signal of the scan recorded directly after domain writing, which may distort the quality slightly, see Fig. 4.3 c). Furthermore, the amplitude signal across the two written states shows a dip, a feature observed at ferroelectric domain walls [214], as indicated in Fig. 4.3 c) and d). Local switching spectroscopy experiments were performed to evaluate whether the signal

is of ferroelectric origin. Fig. 4.3 e) shows the characteristic ferroelectric phase (blue) and amplitude (black) once field is swept between $V_{DC} = \pm 5V$ using an V_{AC} = 1V. The coercive voltage is slightly asymmetric due to the internal field arising from the work function difference between the LSMO bottom electrode and the PtIr PFM tip, occurring at -2.0V and 2.4V. The existence of a coercive voltage, V_C, was determined by varying the drive signal (V_{DC}, V_{AC}). If $V_{DC} < V_C$, dark-blue (1V,1V), no hysteresis is observed. Similarly, if $V_{AC} > V_C$, shown in light-blue (4V,4V), no hysteresis is observed either. Ferroelectric switching is only expected above the coercive voltage[181]. If $V_{AC} > V_C$, the ferroelectric material switches multiple times during the measurement, such that a proper hysteresis loop cannot be recorded. Furthermore, the device was switched using a wide range of frequencies 5-80kHz with no measurable trend in hysteresis, as would be expected for ionic redistribution [215]. Therefore, the combination of evidence from PFM and the expected structural characteristics obtained for the polar phase from XRD measurements suggests the YHO film under investigation is ferroelectric.

4.5 Resistive Switching

The current density - voltage (J-V) characteristics of the heterostructure were inspected by using a source measure unit and a probe station. Bipolar voltage sweeps 0V→-4V→4V→0V were applied to the Au top electrode while the NbSTO substrate was grounded. A sweep rate of 900 mV/s was used, which is equivalent to a frequency of 0.1Hz. The measured current contains contributions from conduction currents J_C and frequency-dependent displacement current J_D, due to the derivative of the displacement field with respect to time, $\frac{\delta \mathbf{D}}{\delta t}$. Prior to measurement, the device was in an intermediate resistance state. A pre-poling step was performed to turn the device into the HRS. Fig. 4.4 a) shows the measured voltage-dependent current density, which varied according to *ABCD*. From 0→-2V in orange, the device is in the HRS until the current sharply increases at *A* by about two orders of magnitude and further rises until *B*. The device remains in the LRS, indicated in blue, until reaching *C*, at which point the device is RESET, and the current gradually decreases until *D*. From *D* the device is in the HRS and the current decreases until 0V. The memory window of the resistive switching (RS) hysteresis is calculated by the ratio between the LRS and HRS currents ($\frac{I_{ON}}{I_{OFF}}$) and is visualised in the inset of Fig. 4.4 a), a maximum window of 540 is reached at 0V.

Fig. 4.4 b) shows the J-V dependence upon increased measurement frequency. High-frequency measurements at 10, 100 and 1000 Hz were performed using an Aixacct thin film analyser. The resistance-switching hysteresis does not change significantly and remains open. In addition, the measured current density remains similar, even with a 4-order of magnitude

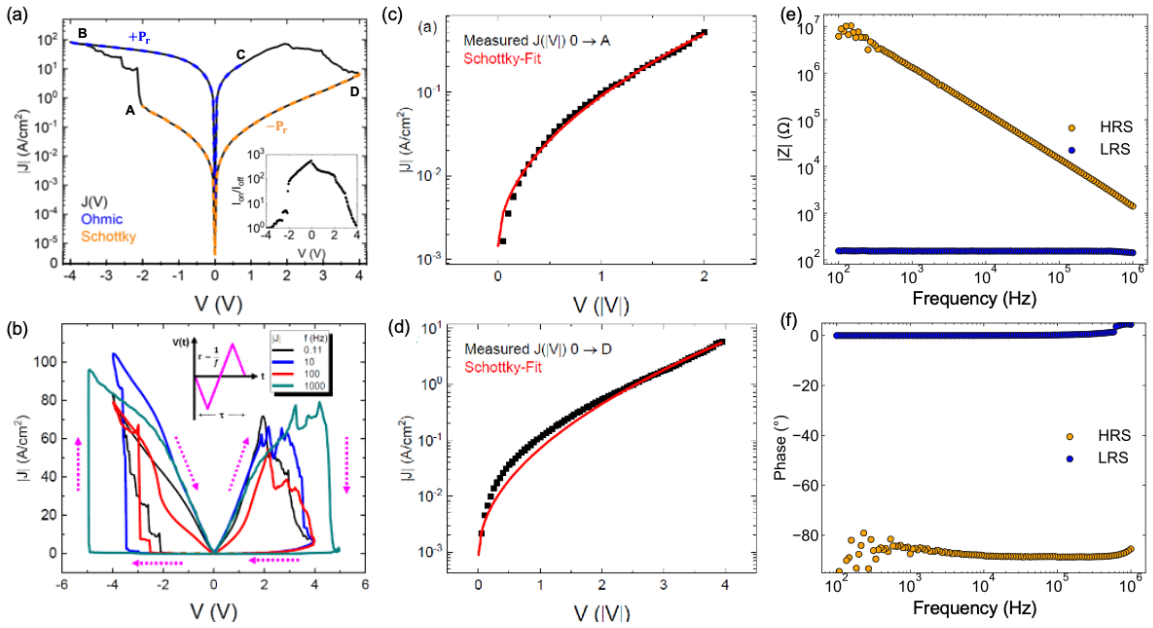

Figure 4.4: Resistance switching characteristic of the device stack a) *J-V* hysteresis at 0.1 Hz b) frequency dependent *J-V* hysteresis c) thermionic emission fit for section 0→A d) thermionic emission fit for section 0→D. e) Impedance magnitude of the HRS and LRS f) Impedance Phase of the HRS and LRS. Fig. reproduced from [173].

frequency difference. The invariance of the current density indicates that the measured current is predominantly a conduction current, rather than a displacement current. A ferroelectric switching peak is not observed here. In a similar system [139], an $\approx 35\mu C/cm^2$ polarisation at 1 kHz in a 5 nm HZO film resulted in a displacement current peak of $\approx 0.5\ A/cm^2$. Here, leakage currents are too large ($\approx 100\ A/cm^2$) to measure a ferroelectric polarisation reversal. It is important to note that the resistance switching hysteresis collapsed at 1-5kHz in similar epitaxial based HZO systems, where dielectric-breakdown related phenomena dominated the resistance change response [216, 217]. Furthermore, as the measurement frequency is increased, the switching voltage increases. In ferroelectric materials, the coercive voltage scales with increasing frequency as $f^{\frac{1}{6}}$ [218]. The observed switching voltage trend here is consistent with the theoretical prediction for coercive field scaling. However, the curve obtained at f = 100 Hz was measured at a different electrode dot and shows a lower coercive voltage. This variability may originate from local inhomogeneity in material or defect distribution.

Next, the nature of the conduction current was investigated. The LRS B→ C is linear in *J-V*, suggesting Ohmic conduction, while the HRS, A→D is highly non-linear. A number of conduction mechanisms were fitted to the observed HRS *J-V* relation, of which thermionic injection, gave a suitable fit see Fig. 4.4 c) and d). Thermionic injection is a commonly

observed conduction mechanism in nanoscale ferroelectrics [219], where the conduction is limited by a interface barrier and is described by equation 4.1

$$J = A^* T^2 \exp\left[-\frac{q}{k_B T}\left(\Phi_B^0 - \sqrt{\frac{qE}{4\pi\varepsilon_0\varepsilon_r}}\right)\right], \tag{4.1}$$

where $A*$ is the Richardson constant, T the temperature, q the elementary charge, k_B the Bolzmann constant, ϕ_B^0 the Schottky barrier height and the ε_r the relative permittivity. The fit parameters are summarised in Table 4.1.

	$0 \rightarrow$ A	$0 \rightarrow$ D
A^* (A/m^2K^2)	(9.5±0.3)*10^7	(6.6±0.2)*10^7
ϕ_B^0 (V)	0.68±0.01	0.69±0.01
ε_r	29.4±0.7	26.1±0.4

Table 4.1: Fit parameters for thermionic injection conduction mechanism.

The fit parameters are within the expected range of values for HfO_2 films, however require a temperature dependent measurement to fully confirm the conduction mechanism. It is important to note that the transport mechanism fit in the HRS could only be performed with reverse-biased thermionic emission. Similar barrier heights were obtained in both bias polarities. This may originate from two possibilities. Either, the device behaves like a symmetric MFM structure, with both interfaces having similar barrier height. Or, it suggests a high built-in voltage (V_{bi}) at the blocking interface. Forward-biased diodes follow a reverse-biased J-V relation below the V_{bi}. Yet, we would like to stress that the fitted J-V relation is, at best, an approximation of the true parameters and physical interpretation at this point is challenging. The observed linearity in J - $\sqrt{V}$ could also indicate Simmons modified Schottky emission, where strong recombination of carriers occurs. The Richardson constant A^* is replaced by $qN_V\nu_D$ with q being the charge, N_V the effective density of states in the valence band and ν_D being the drift velocity. Similarly, Poole-Frenkel conduction shows a similar linearity in J - $\sqrt{V}$ relation.

Next, Fig. 4.4 e) and f) show the impedance magnitude |Z| and phases spectra respectively for the HRS and LRS, which were recorded with an excitation amplitude of 100 mV. The significant on/off ratio observed during J-V cycling is also reflected in the |Z| spectrum, showing a disparity of almost five orders of magnitude at low frequencies, which gradually decreases towards 1 MHz. The phase signal reveals a distinct contrast between the two states, with the LRS exhibiting a $\theta \sim 0°$, indicative of a purely resistive behavior, and the HRS showing $\theta \sim$ -90°, characteristic of a purely capacitive response. Based on the impedance data in conjunction with the *J-V* relationship, we observe a reversible bias induced Schottky-

to-Ohmic transition (SOT). The impedance of the SOT will be thoroughly discussed in chapter 6.

Furthermore, the SOT switching mechanism exhibits stable resistance states and does not require a wake-up treatment, as present in polycrystalline ferroelectric HfO_2 based films [220, 221]. Endurance and retention measurements are discussed in Chapter 5.3. This behaviour is consistent with other epitaxial heterostructure devices based on HZO [139].

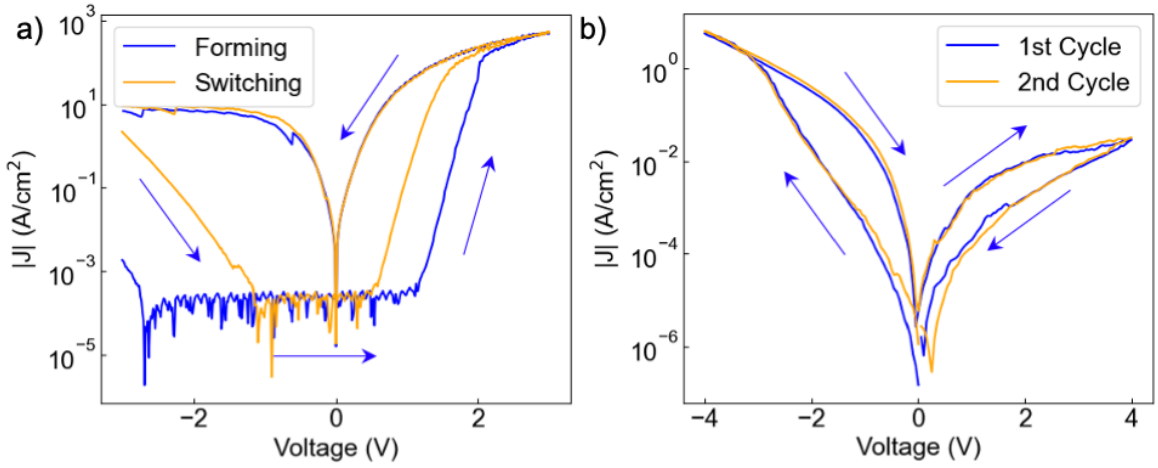

Figure 4.5: *J-V* transport properties of modified device stacks containing a) NbSTO|YHO|TiAu and b) NbSTO|LSMO|YHO|W. Fig. reproduced from [173].

Notably, YHO grown directly on NbSTO without the LSMO displayed poor crystallographic characteristics and did not show any ferroelectric properties in PFM, highlighting the crucial role of the bottom electrode [144]. Fig. 4.5 a) shows the *J-V* transport characterisics of a NbSTO|YHO|TiAu device stack. A forming process and large RS hysteresis is visible. The RS mode displayed a short-term retention of $\sim 10^3$s. A striking visual similarity exists between this RS mode and previously reported systems directly grown on NbSTO [101, 106, 107]. This effect was, therefore not pursued further. Similarly, SOT switching was absent when W top electrodes were used. Fig. 4.5 b) shows the *J-V* transport characterisics of a NbSTO|LSMO|YHO|W stack. The RS hysteresis is significantly diminished compared to the SOT. These findings underscore the significance of electrodes and interface chemistry in stabilising the SOT, which will be further explored in chapter 5.

Based on the available evidence thus far, that the YHO exhibits ferroelectric properties (as shown by PFM), the pristine state of the SOT is stabilised in an intermediate resistance range (not requiring a forming process), and the frequency dependence of the switching voltage being in accordance with expectation for ferroelectrics, we suppose the origin of the resistance change occurs due to a ferroelectric polarisation reversal. However, more evidence

is required to confirm this hypothesis, such as simultaneous measurement of capacitance and current during switching, as shown in chapter 5.

We now compare the observed SOT with structurally similar HfO_2 based ferroelectric heterostructures. We notice the on/off ratio here is significantly larger [202]. Two reported epitaxial ferroelectric tunnel junctions based on HZO reported on/off ratios of 4.4 for a 2 nm thick HZO grown LSMO buffered STO using Co top electrodes [222] and similar 2 nm thick HZO with LSMO-buffered $GdScO_3$ with Pt top electrode showed on/off ratio of 2.1 [223]. In both cases, current conduction was assessed using the tunnelling current through a trapezoidal barrier using the Wentzel-Kramers-Brillouin (WKB) approximation [224] and the Brinkman model[225]. Conversely, Yoong et al inspected an epitaxial 10 nm thick HZO on a LSMO|$LaAlO_3$ heterostructure with a Pd top electrodes and reported a large on/off ratio about 100 [226]. In this case the mechanism was attributed to interface barrier change of about 0.1 eV. However, the LRS J-V remained rectifying. Curiously the thickness of the LSMO electrode was only 10 nm, a thickness range at which confinement effects in the LSMO commence. Peijie et al. grew HZO directly on NbSTO, and successfully demonstrated ferroelectric polarisation-voltage loops despite the polycrystalline nature of the film and the presence of the monoclinic phase [227]. RS hysteresis was observed and showed the 8w switching rotation and a significant on/off ratio of 3-4 orders of magnitude. The large electro-resistance was attributed to the modification of the n-type depletion region within the NbSTO due to the ferroelectric field effect [228, 229]. However, caution must be exercised when interpreting these high on/off 8w systems due to the potential impact of interfacial charge traps [106] and atmospheric oxygen evolution [101]. Lastly, Luo et al. demonstrated a switchable diode effect, where the rectification polarity changes based on the direction of the ferroelectric polarization, based on a symmetric TiN/HZO/TiN stack. This phenomenon was described using a model in which the ferroelectric polarization controls the effective barrier height and width at each interface, thereby enabling only one barrier to block current at a time [62].

The aforementioned switching models do not fully capture the SOT observed here. Yet, Liu et al. predicted a ferroelectric polarisation mediated transition between a Schottky and an Ohmic contact [58], which is schematically illustrated in Fig. 4.6. In this model, a symmetric $SrRuO_3/BaTiO_3/SrRuO_3$ heterostructure was simulated using density functional theory. The $BaTiO_3$ was 6 nm in thickness and highly electron doped, 0.1 e^- per unit cell, yielding an effective carrier density of $\sim 10^{21} cm^{-3}$. At such high carrier concentration, the ultra-thin ferroelectric is not fully depleted, as with FTJs of similar thickness. The model predicts the redistribution of the free electronic charge carrier density $\rho^{(f)}$ within the ferroelectric in response the ferroelectric polarisation. This *internal* screening is dramatically

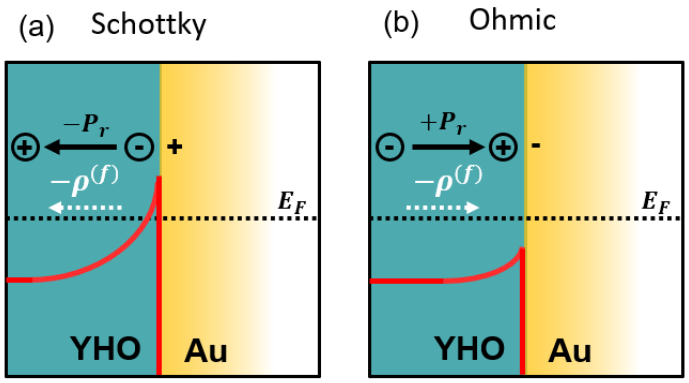

Figure 4.6: Schematic illustration of the Schottky-to-Ohmic transition at the ferroelectric-metal interface a) Schottky contact with polarisation pointing away from the interface b) Ohmic contact with polarisation pointing toward the interface. Fig. reproduced from [173].

different than the *external* screening by electrodes and resulting depolarisation field induced resistance modification observed in FTJs. A polarisation pointing toward (away) an interface causes negatively charged charge density $\rho^{(f)}$ to locally accumulate (deplete), modifying the interface barrier and resulting in Ohmic (Schottky limited) current conduction.

It is important to note that such a SOT at one interface in a symmetric heterostructure would cause one interface to have a Schottky barrier and the other an Ohmic contact. A polarisation reversal would switch the active interface and change the rectification polarity, giving rise to the switchable diode effect [62]. A SOT changing the current conduction across an entire device stack may have already been observed in the first reported ferroelectric diode as reported by Blom et al.[57]. But rather than Ohmic conduction, space-charge limited conduction was observed due to the large (>100 nm) thickness of the ferroelectric. The SOT model by Liu may apply to the presently studied system. However, free electronic charge carrier density in HfO_2 based systems is limited due to dopant compensation [40]. Yet, Y doping creates a single oxygen vacancy, V_O, per 2 Y atoms. These vacancies can create mid-gap states, which may locally trap electrons at the interface, modifying the potential barrier profile [230], which are investigated by HAXPES in section 5.6.

The memristive behaviour of the heterostructure was investigated by performing long-term potentiation – long-term depression (LTP-LTD) measurements, shown in Fig. 4.7. Bias pulses of increasing amplitude are applied to the device to determine whether analog resistance states are present. The device was first set into a HRS. Subsequently, 50 voltage pulses from -1.5 $\rightarrow$-4V with a stepsize of 50 mV and 10 ms pulse width were applied to the top electrode, decreasing the junction resistance, or potentiating the synapse. Between two voltage pulses, the resistance state is recorded at 0.5V for 200 ms. Following the potentiation, the synapse decreases in resistance, using the same voltage profile at positive

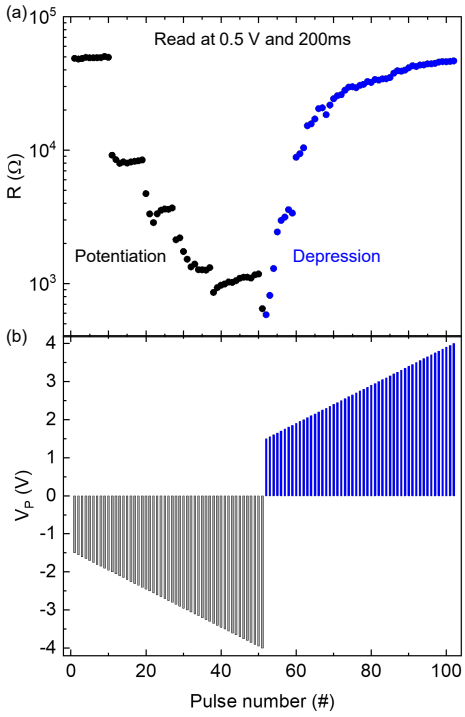

Figure 4.7: Memristive characterisation of the device stack a) resistance change from HRS upon application of a voltage pulse profile b). Fig. reproduced from [173].

polarity. Curiously, during potentiation step-like changes in resistance are observed. These resistance states are met again during depression. However, within the high resistance range of the depression, the device exhibits a continuous or analog change in resistance. The step-wise behaviour could be attributed the switching of a number of ferroelectric domains, whereas the analog regime is consistent with the motion of ferroelectric domain walls [194, 231].

Fig. 4.8 shows a further set of advanced neuromorphic function characterisation beyond analog behaviour in LTP-LTD measurements. Fig. 4.8 a) displays the resistance of the device upon a series of -2V voltage pulses, which was measured at 0.1V after each pulse. The resistance first remains stable in the HRS until it suddenly drops into the LRS and increases slightly again after the first ∼50 pulses. This behaviour emulates the 'integrate-and-fire' response associated with neuronal behaviour. Such effects have been observed previously in ferroelectrics and had been attributed to the nucleation-limited domain switching regime in HZO [232]. We subsequently investigated whether the resistance change in the device stack was timing-dependent. The inset of Fig. 4.8 c) describes the measurement procedure, where first the initial resistance R_0 of the device is measured and then two pulses with varying time interval (Δt) are applied. Afterwards, the final resistance R_f is measured. Paired pulse

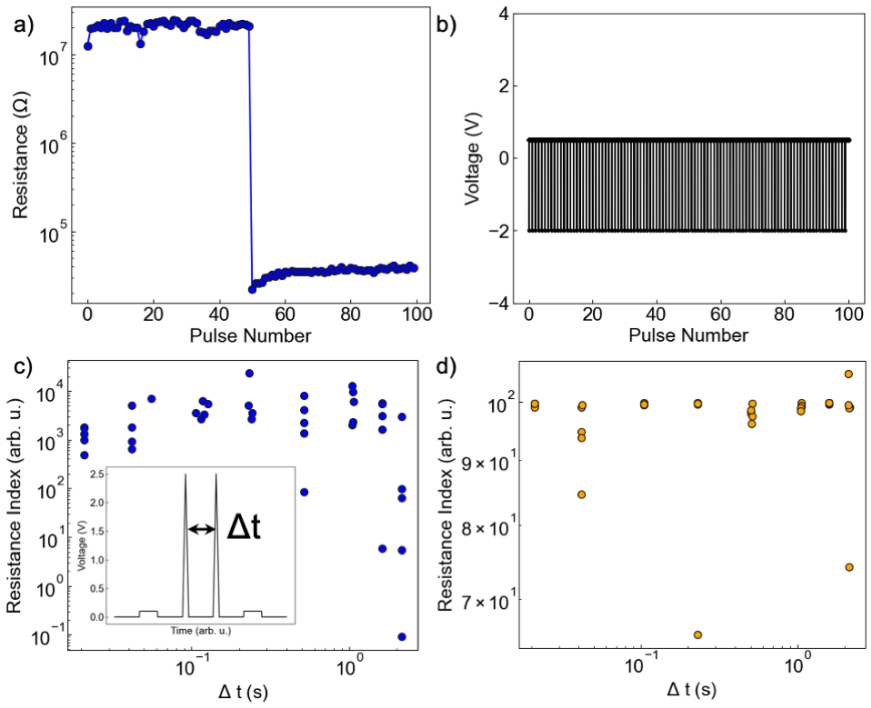

Figure 4.8: a) Demonstration of neuronal integrate and fire property achieved with b) pulse train c) Paired pulse facilitation measurement with measurement scheme shown in the inset d) paired pulse depression measurement

facilitation (PPF) or depression (PPD) is observed if the resistance index ($\frac{R_0 - R_f}{R_0}$) is larger for shorter time intervals. The time dependence of the resistance change would, therefore, indicate second-order behaviour [233]. Fig. 4.8 c) and d) show 5 iterations of PPF and PPD measurements. The resistance index does not change with a decrease in Δt. The SOT, therefore, displays first-order complexity within the measured time domain.

4.6 Conclusion

In conclusion, the growth of a high-quality epitaxial NbSTO|LSMO|YHO has been achieved. Ferroelectrity was demonstrated using PFM. A Schottky-to-Ohmic transition during resistive switching was observed, which showed memristive behaviour. The switching mode was stabilised in an intermediate resistance state and did not require an electro-forming process. Furthermore, no wake-up effect has been observed. The switching was proposed to be correlated to a ferroelectricity-modulated interfacial barrier modulation. Here, trapped charge carriers would internally screen the polarisation resulting in a change of transport properties at the interface, causing large on/off ratios. However, the influence of electronically active

defects, uncorrelated to ferroelectricity, in contributing to the observed resistance change within the device cannot be excluded and may play a significant role [234–237]. Particularly, in ultra-thin ferroelectric devices, a coupling between electrochemical and ferroelectric degrees of freedom can occur [206, 238]. Furthermore, the strong impact of the electrode interfaces on the switching behaviour has been demonstrated and requires further study. Lastly, further evidence is required to prove the ferroelectric origin of the resistance change.

Chapter 5

Schottky-to-Ohmic Switching via Electrode Design

Chapter Summary
This chapter presents an in-depth analysis of the interface chemistry of the device stack using material modifications, STEM and HAXPES. Carefully designed oxygen reservoirs were found to be required to stabilise the Schottky-to-Ohmic transition. Combined current and capacitance-voltage measurements indicated that ferroelectric polarisation reversal is not the dominant mechanism, rather the reversible oxidation and reduction of localised filaments drove the resistance change.
The results of this chapter are under review for publication.

Author contributions
PLD and electrical characterisation and analysis were performed by me. Cathodoluminescence measurements were performed by Gunnar Kusch and me. Photoluminescence measurements were performed by Nives Strkalj. STEM/ELNES measurements were performed by Simon Fairclough, analysis by me. HAXPES measurements were performed by Megan Hill, Nives Strkalj, Dibya Phuyal and Ji Soo Kim, fitting was performed by Megan Hill, and analysis by me.

5.1 Introduction

Resistance switching (RS) induced by ferroelectric (FE) polarisation reversal can have a multitude of origins. Polarisation surface charges affect tunnel barriers [64, 239, 240], depletion regions [57, 62, 219], alter the resistance of the underlying material through the ferroelectric field effect [228] and can lead to localised conduction through domain walls [241]. Disentangling and identifying these contributions to resistance change is paramount and relying solely on current-voltage (J-V) characteristics yields limited information. Techniques such as hard X-ray photoelectron spectroscopy (HAXPES) hold promise for independently confirming barrier height changes within these systems as well as offering a deeper understanding of the electrochemical behaviour at the nanoscale under polarisation reversal [205]. Furthermore, it is essential to determine whether the resistance change is genuinely driven by ferroelectric polarisation reversal or whether it contains coupled or coexisting ionic contributions. This often involves comparing the switching voltages from quasi-static J-V measurements to coercive fields observed during polarisation-voltage measurements (J-V). Yet, this approach is challenging to achieve if the leakage current is high or the RS hysteresis remains even at high measurement frequency, where ferroelectric displacement currents should dominate. The simultaneous measurement of capacitance and current-voltage relationships, therefore, offers a promising alternative to correlate ferroelectric and resistive switching[242]. The coexistence of ferroelectric and ionic switching in epitaxial [216, 217] and polycrystalline [220, 243–245] ferroelectric HfO_2 based systems has been described previously. These reports mainly concerned the evolution of a short-lived conductive filament within the ferroelectric material with low RS endurance. The ionic contribution interrupted the ferroelectric polarisation reversal, preventing the measurement of polarisation-voltage loops. The filaments were hypothesised to be formed along grain boundaries [245]. However, a simultaneous measurement of ferroelectric polarisation reversal and redox based resistance switching in HfO_2 systems, as far as we know, remains to be reported.

In the previous chapter, we described a resistance transition from Schottky to Ohmic conduction (SOT) in devices composed of ultrathin epitaxial ferroelectric $Hf_{0.93}Y_{0.07}O_2$ on $La_{0.67}Sr_{0.33}MnO_3$-buffered Nb-doped $SrTiO_3$ (NbSTO|LSMO) substrates [173]. This transition exhibited a significant on/off ratio and proved to be highly sensitive to the electrode environment. Further investigation is required to elucidate the underlying mechanisms of the SOT, as initial assessments were based solely on J-V characteristics. Lastly, endurance and retention performance parameters are required to gain a comprehensive understanding of the functionality of the device stack.

A key aspect of interest in the SOT is the pre-poling stage, where the pristine (unpoled) state of the device is close to the LRS, not requiring a forming process. By utilising simultaneous *C*-*V* and *J*-*V* curves, we find that the SET operation may be correlated with ferroelectric polarisation reversal due to an overlap of the switching voltage and capacitance maximum, while the RESET operation does not. Current measurements based on varying electrode areas reveal the HRS current is transported homogeneously across the entire electrode surface, while the LRS current is not area-dependent. Thus, the current transport is confined locally through the device stack through conductive channels or filaments. Finally, the SOT switching mode has a stable retention and an endurance of up to 10^5 cycles.

We further systematically vary the device stack to determine design principles for achieving a SOT. Replacing the YHO with $HfZrO_4$ (HZO) does not result in a change in RS characteristics. The lack of impact of the dopant was similarly confirmed by photo- and cathodo-luminescence measurements. Here, the optically active defect signatures were similar between the two compositions, indicating a common origin, possibly due to the common processing conditions. The impact of oxygen leaching at the top interface was assessed by modifying the electrode chemistry. The Ti|Au was first replaced by Pt, a material with high workfunction, low oxygen affinity that does not require an adhesion layer. In addition, a device stack with significantly larger Ti adhesion layer thickness was inspected, a material with a low workfunction and high oxygen affinity. Using Pt top electrodes prevented the SET operation, whereas the thick Ti interlayer prevented the RESET operation of the SOT. We therefore conjecture that a precisely designed oxygen reservoir is required to stabilise the SOT. In conjunction, the thickness of the LSMO bottom layer plays a critical role and is required to be thin (<11 nm) for the SOT operation, indicating a role of the complex interface between LSMO and YHO during the resistance switching process.

Finally, we assess structural and electrochemical aspects of the device stack in different resistance states by inspecting energy loss near edge structure (ELNES) in scanning transmission electron microscopy (STEM) and performing hard X-ray photo-electron spectroscopy (HAXPES). We find that the Ti interlayer is fully oxidised already in the pristine state and penetrates significantly into the YHO, indicating a degree of oxygen scavenging. Furthermore, oxygen is found to move in and out of the YHO layer during the RESET and SET process, respectively, by detecting the oxidation of both LSMO and Ti in the LRS. Overall, we demonstrate the intricate electrochemical balance present in the SOT and propose design rules to stabilise the switching mode to create devices with high and stable on/off ratio.

5.2 Experimental methods

Fabrication and Current-Voltage Measurements

Details have been described in section 4.2.

Capacitance-Voltage Profiling

CV measurements were performed using a Ametek Solatron Impedance analyser with a sweep frequency of 0.01 Hz and a measurement frequency 1 MHz.

Luminescence

Cathodoluminescence was performed using a FEI-XL30 FEGSEM with a Gatan MonoCL cathodoluminescence (CL) system. An acceleration voltage of 1 keV and a 5 nA beam current and an integration time of 5s per step was used.

STEM

STEM was performed using a probe-corrected ThermoFisher Spectra 300 at 300kV and 40 pA. A Gatan Continuum EELS spectrometer was attached. Images were obtained at a convergence angle of 24 mrad. EELS spectra were acquired using a dwell time of 1s and a beam current of 100 pA. EELS spectra are sensitive to plural scattering events. This effect was evaluated using the ratio-log technique, which gives the ratio of the thickness of the sample, t, to the inelastic mean-free path of electrons, λ. A $\frac{t}{\lambda} = 0.7 \pm 0.05$ was obtained, indicating an ejected electron is on average scattered less than once when passing through the lamella. Therefore the effects of plural scattering are expected minimal in the EELS spectra. The EELS map was obtained along 20 nm out-of-plane of the device and 5 nm in-plane. Spectra were summed and averaged in-plane to improve signal to noise. A power-law background was removed for each core loss spectrum and calibrated in a region of 10 nm before the onset of the individual peak [197].

HAXPES

Hard X-ray photoelectron spectroscopy (HAXPES) measurements were performed at the I09 Beamline of the Diamond Light Source. The beam was confined to a spot size of 100 μm and an acceleration voltage of 5.9 keV was used. Two configurations were tested: the bare film of the heterostructure without electrodes (allowed the the top surface of the NbSTO to be sampled) and the heterostructure in device configuration with an ultrathin 6 nm TiAu top electrode (allowed the top surface of the LSMO to be sampled). A full summary of the calculated penetration depths is given in the Table 5.1. Each of these configurations were in the pristine state, LRS and HRS. The state of devices with top electrodes was set by using a probe-station, whereas the bare film was modified by switching the ferroelectric polarisation direction across large areas using PFM. The bare film did not show any resistance changes.

5.3 Electrical Characterisation

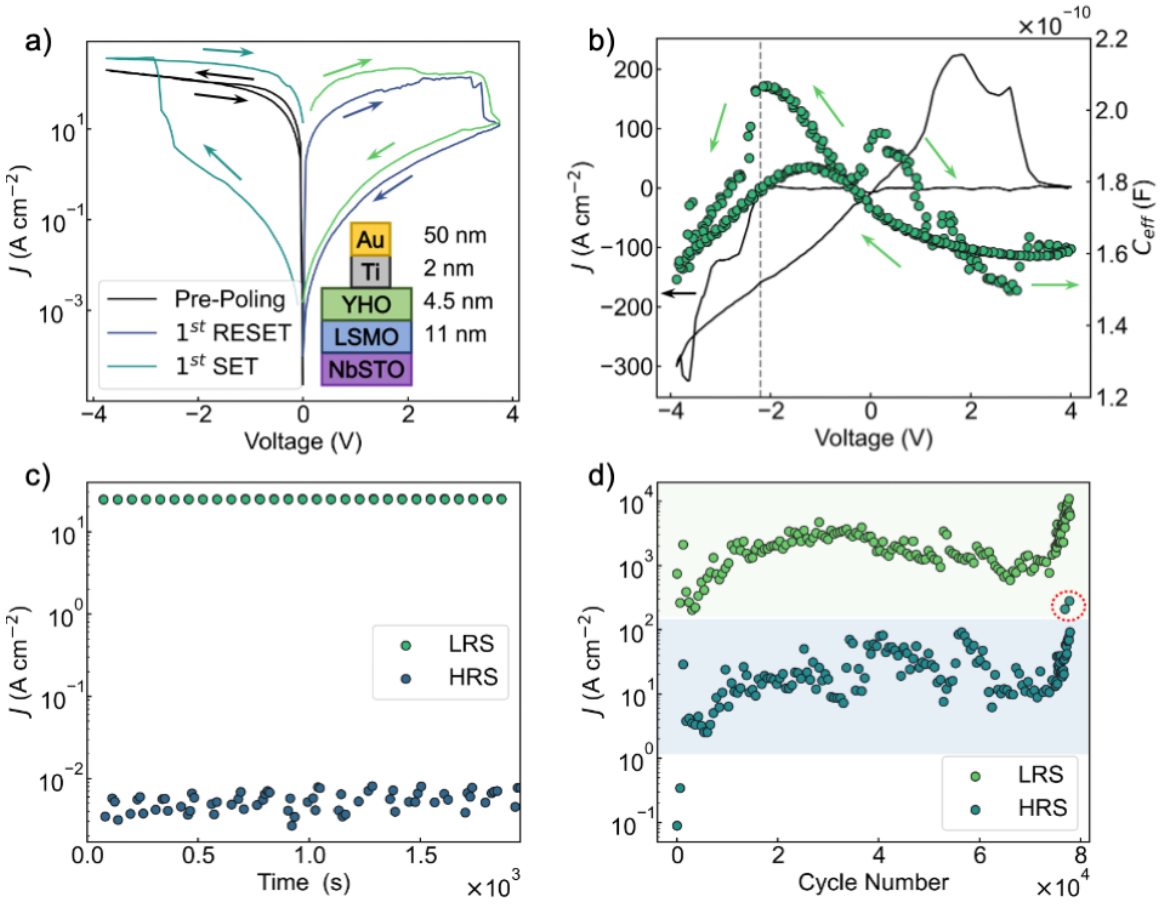

Figure 5.1: a) *J-V* profile of the SOT switching with the pre-poling stage b) Simultaneous measurement of *J-V* and *C-V*, showing the correlation between SET voltage and coercive voltage. Current dependence on electrode area measured at -1V, averages are shown in colour while raw data is illustrated in grey c) LRS d) HRS.

We begin by outlining the operational principles of the SOT, details on the pristine resistance state, area-dependence, capacitance-voltage and performance metrics of retention and endurance are discussed. SOT switching commences after the application of a bipolar *pre-poling* step, shown in Fig. 5.1a). The device is first poled from 0 →-4V and subsequently -4 → 0V. An already high current density, close to the LRS, is observed in pristine state, with no evidence of sharp changes occurring, which would be indicative of electro-forming behaviour. As the device is poled from 0 → 4V and back, a sharp decrease in current is observed and the device is RESET into the HRS. The SOT switching continues in subsequent cycles, where the current increases sharply around -2.5V during the SET process and drops

more gradually around 3.7V during the RESET process. The SOT therefore has a counter 8 wise (c8w) switching rotation.

We now consider Fig. 5.1b), where the simultaneous measurement of the *C*-*V* relation during the *J*-*V* measurement of the SOT is shown. The *C*-*V* shows a characteristic ferroelectric butterfly loop, confirming the ferroelectric nature of the YHO. The loop exhibits two maxima at -2V and 0.5V, corresponding to the coercive voltages of the ferroelectric. The asymmetry in coercive voltage indicates the presence of an internal bias field across the device structure, characteristic of imprint behaviour [246] due to defective surfaces or an asymmetry in electrodes. We further notice that the capacitance at positive polarity is significantly suppressed. This feature is indicative of an additional capacitance being present in series with the YHO capacitance [247], possibly a depletion region. In a semiconductor, the depletion region W_d width depends inversely upon charge carrier concentration, N_a.

$$W_d = \sqrt{\frac{2\varepsilon_0\varepsilon_{sc}\phi_{sc}}{qN_a}} \tag{5.1}$$

Here ε_0 is the permitivity of free space, ε_{sc} the permitivity of the semiconductor, ϕ_{sc} the semiconductor workfunction and q the elementary charge. The depletion region capacitance C_{W_d} per unit area is inversely proportional to the depletion region width.

$$C_{W_d} = \frac{\varepsilon_0\varepsilon_{sc}}{W_d} \tag{5.2}$$

For a p-type semi-metal, such as LSMO, hole charge carriers are depleted at positive voltages. As such a space-charge region may be present at the LSMO|YHO interface. Furthermore, the saturation capacitance measured at -4V corresponds to a relative permittivity ε = 15.7. The magnitude is quite low compared to 35 expected for the orthorhombic phase in polycrystalline films [248]. A range of factors could result in a low dielectric constant, such as the presence of a smaller series capacitance, the presence of phases with low permittivity, such as the monoclinic phase, or incorrect assumptions about the film thickness or electrode area.

Finally, considering the simultaneous *C*-*V* and *J*-*V* measurement, we notice that the SET voltage and the coercive voltage at negative polarity overlap, whereas the RESET voltage and the coercive voltage at negative polarity do not. This therefore clearly demonstrates that ferroelectricity alone is not responsible for the SOT switching. However, the overlap of switching voltages suggests that the ferroelectricity and RS behaviour may be inter-related.

Next, we examine the dependence of the conduction current in the HRS and LRS upon a change in the electrode area, see Fig. 5.1 c) and d) for LRS and HRS respectively. We find the

HRS current scales with the electrode area, indicating the current is conducted homogeneous across the electrode area. In contrast, the current in the LRS does not change significantly, conduction therefore is confined and occurs along local paths. This behaviour is consistent with typical filamentary RS modes, where the growth and dissolution of a conductive path govern the resistance state. From here on we will use the 'filament' nomenclature to refer to any type of conductive path present. However, SOT RS modes do not require a forming process and the systems are grown close to the LRS, suggesting the filaments are already present in the pristine state. This is in stark contrast to the aforementioned examples, which exhibit both ferroelectricity and filamentary switching. These examples reported their systems to be in the HRS, or even lower resistance, in the pristine state. The presence of the conductive paths in the pristine state may originate from a defective top surface, induced through highly energetic sputter deposition of electrodes, or from oxygen scavenging by top electrodes. Additionally, incoherent grain boundaries, which have been indicated to be more conductive than the grains, could serve as the conductive paths themselves or act as preferential sites for filament formation [92, 245, 249]. This will be investigated in detail shortly. Finally, a correlation between ferroelectricity and filamentary switching may be caused by the ferroelectric displacement current creating additional heat, which drives filament growth or dissolution. Furthermore, a strong depolarising field and piezoelectric effects at grain boundaries may alter or favour the migration of ions in specific directions, favouring certain local stoichiometry configurations and could therefore help trigger filament formation.

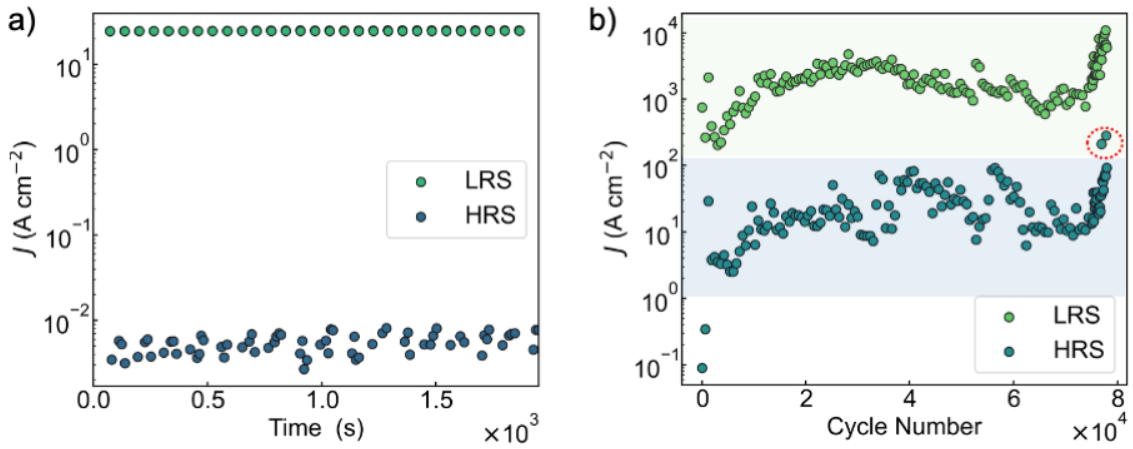

Figure 5.2: a) Retention measurement obtained at V_{read} = -0.1V b) Endurance measurement up to $8*10^4$ cycles showing every 500 measurements for clarity.

The key performance metrics of the SOT are assessed in Fig. 5.2a) in terms of state retention and endurance. The retention was conducted by recording the state at -0.1V after the device had been biased by ±4V to determine the resistance state. Over time, both HRS and LRS are very stable and both only becoming slightly less resistive over time. The time, t, dependent current, $I(t)$ could be modelled by a power-law, $I(t) \propto t^{-n}$. The exponent n corresponded to extremely low values of $n = 0.002$ and $n = 0.083$ for HRS and LRS respectively. This behaviour may be indicative of Curie-von-Schweidler type behaviour of electronic polarisation relaxation. Endurance was tested by applying pulsed voltages of ±4V for 10 ms, state readout was performed after every pulse 0.5V, followed by full *J-V* sweeps every 200 cycles to assess degradation. The device exhibited relatively stable performance initially, but resistance increased over time, as detailed in Fig. 5.2b). This endurance is significantly more stable compared to comparable HfO_2 ferroelectric-filament RS devices but does not match the stability seen in purely ferroelectric systems.
To establish the design rules governing the stabilisation of the SOT, we modify the materials in the stack and observe the resulting RS behaviour. We first modify the defect chemistry present in the ferroelectric and compare the device stack using $HfZrO_4$ (HZO) instead of YHO. Unlike the aliovalent Y^{3+} ion in YHO, the Zr^{4+} ion in HZO is isovalent and therefore does not create electronic dopant-compensating vacancies. As shown in Fig. 5.3 a), the HZO-based device stack still exhibits the SOT and is indistinguishable from those with Y doping. Therefore, the SOT does not rely on the internal composition and aliovalent dopant-induced oxygen vacancies play a negligible role in influencing the SOT RS characteristics. The defect levels of HZO and YHO device stacks are further inspected by using cathodoluminescence and photoluminescence later on.

Next, we modify the top interface by depositing Pt top electrodes instead of Ti|Au. Pt, like Au, is a noble metal and has a high work-function. However, its use eliminates the need for an adhesion layer to bridge the electrode and the material of interest, therefore allowing probing of the effect of the adhesion layer on the RS characteristics. Furthermore, Pt has a much lower oxygen affinity than Ti and the scavenging of oxygen is therefore expected to be diminished [103]. However, despite its low oxygen affinity, Pt can adsorb oxygen within under-coordinated grain-boundaries and lead to catalytic activity with water [99, 101]. Inspecting the RS behaviour in Fig. 5.3 b), we again observe a high current in the first negative sweep, indicating that the pristine state is still in the LRS. This would suggest that the conductive nature of the pristine state originates from the LSMO|YHO heterostructure. However, after the device has been RESET into the HRS, it does not switch into the Ohmic regime, being unable to complete a SET operation.

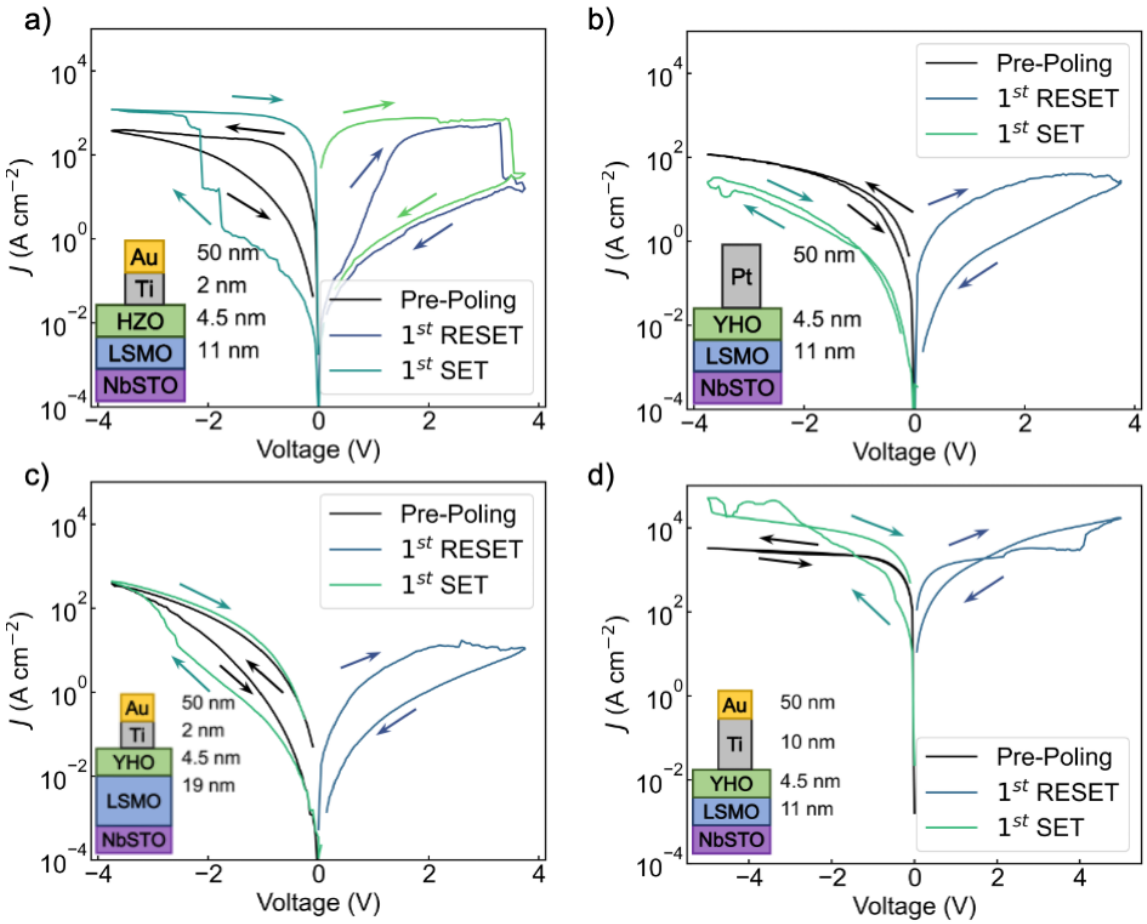

Figure 5.3: a) *J-V* of a device stack using HZO instead of YHO ferroelectrics b) *J-V* of a device stack using Pt instead of TiAu top electrodes c) *J-V* of a device stack using 19 nm LSMO instead of 11 nm LSMO d) *J-V* of a device stack using 10 nm Ti instead of 2 nm Ti as an interlayer.

In contrast, we inspect the role Ti interlayer by depositing 10 nm Ti rather than 2 nm, while keeping the Au top electrode. Fig. 5.3 d), shows a dramatic increase in overall current density. The pristine state exhibits slightly higher currents but upon a bipolar voltage sweep, the device is unable to reset. This clearly shows that the interlayer of the Ti|Au top electrode plays an important role in stabilising the SOT. A carefully balanced volume of oxygen scavenging is required to allow for both the SET and the RESET operation.

Finally, we investigate the impact of the LSMO bottom electrode. Fig. 5.3c) shows the *J-V* relation of a device stack with 19 nm of LSMO rather than 11 nm. Thicknesses of 20 nm and above are more commonly used for testing ferroelectrics. We clearly observe that the 19 nm LSMO does not stabilise the SOT and rather exhibits a much smaller RS hysteresis, which only persists for 5 cycles. The results here are similar to those reported by Knabe et al.

[216]. This points to a complex role of LSMO in stabilising the SOT and is investigated in more detail by ELNES and HAXPES.

5.4 Luminescence

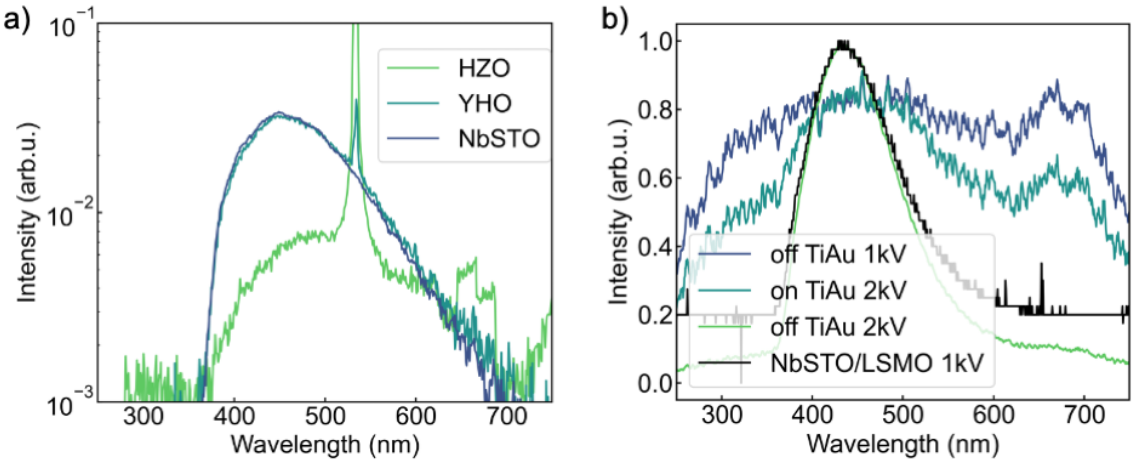

Figure 5.4: a) Photoluminescence spectra of NbSTO substrates, NbSTO|LSMO|YHO and a STO|LSMO|HZO heterostructure b) Cathodoluminescence spectra of a NbSTO|LSMO substrates and a NbSTO|LSMO|YHO with ultrathin 6nm Ti|Au electrodes.

Defect states in the heterostructure were accessed using two optical techniques, photoluminescence (PL) and cathodoluminescence (CL), illustrated in Fig. 5.4 a) and b) respectively. PL was performed with an excitation wavelength of 260 nm. Three samples were tested, the NbSTO substrate, a NbSTO|LSMO|YHO and a STO|LSMO|HZO heterostructure. Each spectrum displays a sharp peak at 520 nm, which occurs due to the origin of the excitation laser being the second harmonic generation from the 520 nm laser. The NbSTO shows a broad emission between 350-700 nm, which obscures any signal originating from the NbSTO|LSMO|YHO system. In undoped STO, the broad emission has a significantly weaker intensity and a small emission doublet around 670 nm can be identified in the STO|LSMO|HZO system. In contrast to PL, CL allows the user to tune the interaction volume of the incident electron beam by manipulating the acceleration voltage. Fig. 5.4 b) shows the CL spectra in 4 different conditions. First, the NbSTO|LSMO reference sample still shows a broad emission between 300-600 nm when measured at 1 kV. Measuring the bare, electrode-free heterostructure at an acceleration voltage of 2 kV, shows a dominant signal from the substrate, however decreasing the acceleration voltage to 1 kV, confines the beam within the 5 nm of YHO and again shows an emission doublet at 670 nm. In addition,

a thin 7 nm Ti|Au top electrode can be used to raise the electron interaction volume from the NbSTO into the YHO by recording the spectrum at 2 kV. CL signal was acquired underneath electrodes, which were poled into HRS and LRS respectively, but showed no discernible difference. The existence of the emission around 670 nm in both HZO and YHO shows that the optically active defect measured here does not come from defect complexes [250], but rather originates from the fabrication conditions. The emission signal at 670 nm had been previously identified to originate from oxygen vacancies and plays a crucial role in the ferroelectric wake-up effect [134, 251]. Interestingly, Perevalov et al observed a strong emission at 475 nm and correlated oxygen-vacancy-mediated phonon-assisted tunnelling between traps in ferroelectric La-doped HZO [252, 253]. However, the strong signal of the substrate in this wavelength region obscures the measurement in the present study.

5.5 Transmission Electron Microscopy

To investigate the structural and chemical properties of the pristine state of the device, scanning tunnelling electron microscopy (STEM) and electron energy loss spectroscopy are performed. Fig. 5.5 a) shows the high angle annular diffraction (HAADF) proportion of the image along the [110] zone axis of NbSTO. The bottom two materials, NbSTO and LSMO show a flat, coherent interface with a cube-on-cube epitaxial relationship. The YHO|LSMO interface on the other hand shows a two monolayer coherent and epitaxial interface region. This has been reported previously and has been attributed to a tetragonal phase, which is critical to stabilise the polar phase [139]. The YHO on top shows a different crystal periodicity. Large areas of the scan were analysed using fast Fourier transforms to determine the lattice parameter of the materials. The lattice parameters were determined to be 3.07 Å and 2.26 Å for (111) and (11-1) YHO and 4.05 Å for (001) LSMO. These are consistent with the measurements performed previously using XRD, see section 4.3. The YHO above the epitaxial interface layer is observed to contain sections of varying orientations, with coherent regions being 5-6nm in size, see appendix A.1, which correlated with the topography observed using AFM. Although the film is not strictly epitaxial, this manuscript will continue to use the term, as these observations align with previous reports on *epitaxial* HfO_2. The discontinuities between incoherent crystalline sections of the YHO film may pertain to a number two dimensional defects, this manuscript term these defects as grain-boundaries. To assess the extent of chemical and structural changes within the device stack, energy loss near edge spectra (ELNES) of the Ti L_{23} (L_2: 462 eV, L3: 456 eV), O K (532 eV) and Mn L_{23} (L_2: 651 eV, L_3: 640 eV) core-losses are shown in Fig. 5.5 b). Transition metal L edges originate from excitations of 2p to 3d orbits. Spin-orbit coupling causes the 2p

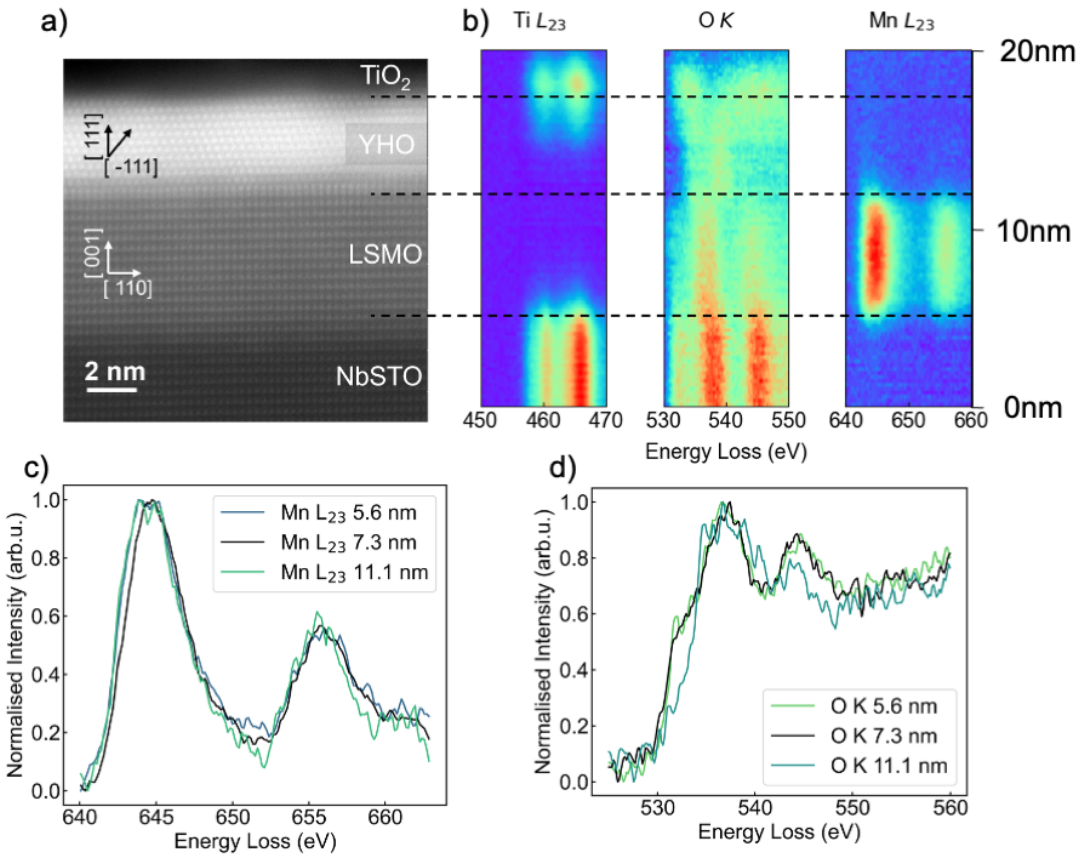

Figure 5.5: a) HAADF STEM of the device stack along the (110) zone axis of NbSTO b) spatial extent of the ELNES signal for Ti L_{23}, O K and Mn L_{23} core losses c) Mn L_{23} core losses at the YHO|LSMO interface, the centre of LSMO and the NbSTO|LSMO d) O K core losses at the YHO|LSMO interface, the centre of LSMO and the NbSTO|LSMO.

electrons to lose degeneracy and split $2p_{\frac{1}{2}}$ and $2p_{\frac{3}{2}}$ orbitals, corresponding to L_2 and L_3 edges respectively. Furthermore, the influence of the crystal field splits the 3d electrons orbitals into t_{2g} and e_g orbitals, further splitting each L edge. However, the current measurement resolution is not sensitive enough to detect the crystal field splitting. The O K edge displays excitations from O 1s to 2p orbitals and exhibits a rich fine structure, which is very sensitive to local coordination and bonding changes and hence is dependent on the material. For STO, the O-K edge fine structure contains 4 main peaks. The pre-peak corresponds to orbitals hybridised Ti 3d, the 2nd peak likely originates from Sr-O interactions, and the 4th peak from Ti 4s hybridised states [254]. In LSMO, the pre-peak has Mn 3d character, 2nd peak corresponds to La 5d and the 3rd peak originates from Mn 4sp hybrids [255]. Finally, for non-perovskite TiO_2, the pre-peak again has Ti 3d character, whereas the second peak is

sensitive to 4s and 4p states [256]. The pre-peak is therefore highly sensitive to valence electronic structure and its intensity is often used to assess the relative oxygen deficiency [75, 101].

The spatial extent of the respective elemental signatures can now be used to assess the degree of interdiffusion between the materials. At the NbSTO|LSMO interface, sharp chemical changes between Ti and Mn L_{23} edges indicate homogeneous interfaces with little interdiffusion. For Ti interlayer, on the other hand, the signal penetrates significantly into the YHO, possibly due to the high kinetic energy during sputter deposition. Furthermore, the presence of a significant O K intensity concomitantly with the Ti L_{23} would suggest the Ti is oxidised. The O K signal also changes gradually towards a HfO_2-based signal, whereas at the LSMO|YHO interface, the O K edge changes occur more abruptly, indicating a lesser degree of interdiffusion at the bottom interface. A more detailed assessment was performed by taking line scans of Fig. 5.5 b) at specific positions to inspect chemical changes at the interface. The centre of the LSMO (7.3 nm) is compared to the NbSTO|LSMO (5.6 nm) and LSMO|YHO (11.1 nm) interfaces. Fig. 5.5 c) shows the normalised Mn L_{23} edges. For both interfaces, the L_3 whiteline slightly shifts towards lower energies. By fitting the peak positions with a Gaussian function, the shifts were determined to be 0.4 eV at the bottom interface, and 0.8 eV at the top interface. The L_3- L_2 separation increased slightly, yet the relative intensity ratio remained consistent. A shift towards lower energy indicates an increased negative charge carrier density, consistent with the formation of a depletion region within the LSMO. These changes occurred over $\sim$2 nm, which is larger than expected for the typical screening length of 1.2 nm in fully metallic LSMO [257]. The O K edge for the LSMO centre and the NbSTO interface did not show any significant changes. However, at the LSMO|YHO interface, the O-K pre-peak completely disappears and the 2nd peak loses intensity. As the pre-peak intensity is correlated with stoichiometry, the LSMO|YHO interface is oxygen depleted [258]. This deficiency has been reported previously in LSMO|HZO heterostructures, it has however not been correlated to RS effects and typically is confined to a thinner region at the interface [142, 145, 146, 259].

Next, the Ti interlayer is assessed at its centre (17.8 nm) and close to the YHO (16.1 nm) for Fig. 5.6 a) the Ti L_{23} edge and b) the O K edge. The Ti L_3 slightly decreases in intensity and broadens toward the interface. O K is first well separated into two peaks at the centre but subsequently loses its fine structure toward the interface. Both the peak-broadening and the loss of fine structure are indicative of significant increase in structural and electronic disorder, which is accompanied by a decrease in stoichiometry. These changes occur gradually, indicating an oxygen gradient being present, where the top of the Ti interlayer is well oxidised [260, 261]. Finally, the NbSTO side of the NbSTO|LSMO interface (4.8 nm) is

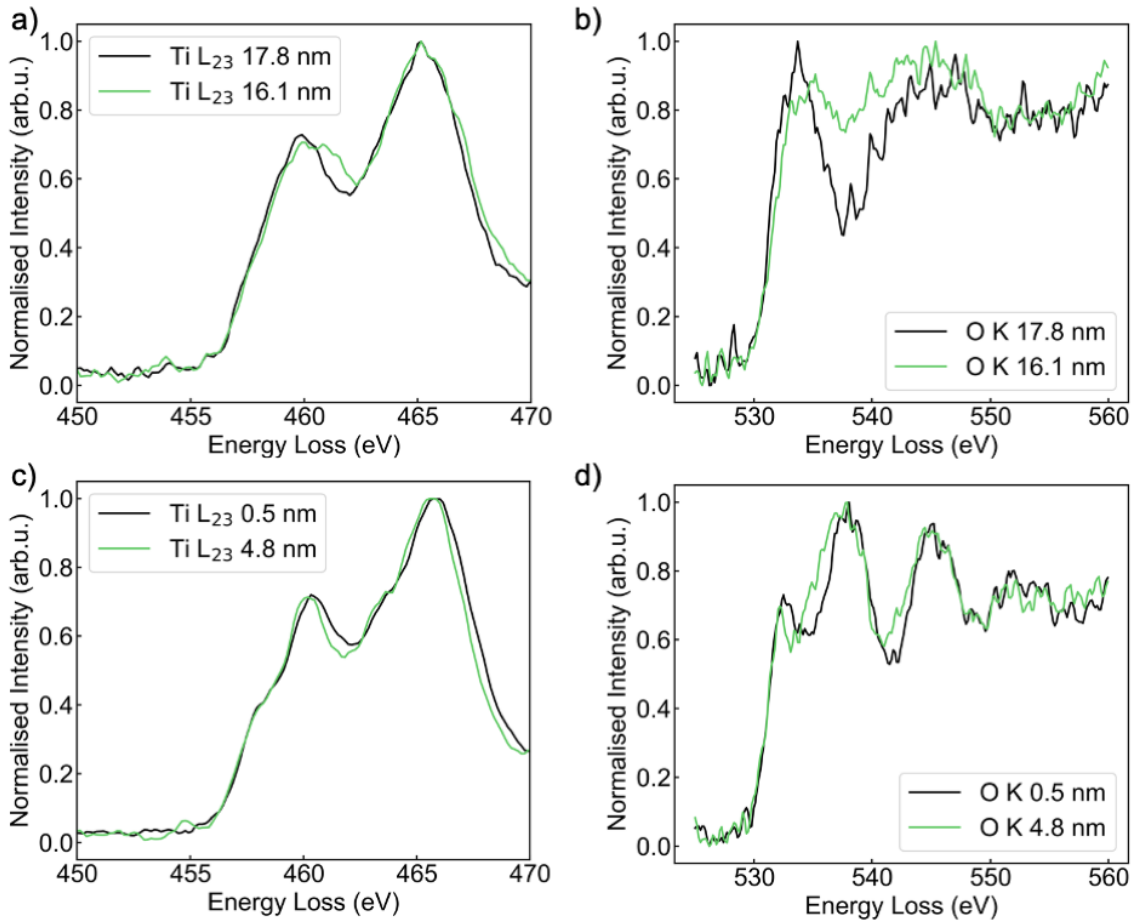

Figure 5.6: a) Ti L_{23} core losses at the YHO|TiO_2 interface and the centre of TiO_2 b) core losses at the YHO|TiO_2 interface and the centre of TiO_2 c) Ti L_{23} core losses at the NbSTO|LSMO interface and the centre of NbSTO d) core losses at the NbSTO|LSMO interface and the centre of NbSTO.

inspected and shown in Fig. 5.6 c) and d). The Ti L_{23} shifts towards slightly lower energies at the interface, by 0.4 eV. Peak intensities and splitting remain similar. Again a decrease in the pre-peak intensity of the O K edge is observed. These data suggest that the surface of the NbSTO is also oxygen deficient. A Ti L_{23} peak shift of 0.4 eV can be related to an oxygen deficiency of $\delta \approx 0.1$ in $NbSTO_{3-\delta}$ at the surface [262]. This deficiency may originate from the vacuum annealing step or PLD deposition of LSMO.

5.6 Photoelectron Spectroscopy

To detect and compare electrochemical changes between the pristine state and the HRS and LRS, we performed hard X-ray photoelectron spectroscopy (HAXPES). Details of the measurement procedure are found in section 5.2. So far, HAXPES studies on ferroelectric HfO_2 focused mainly on inspecting stoichiometry [87, 263–265] and band alignment [79, 266, 267] in a single polarisation direction rather than the effects of polarisation reversal. Matveyev et al. studied the polarisation reversal in a non-RS ferroelectric capacitor structure and indicated redox reactions occur at the interfaces [268]. In this thesis, we aim to correlate the resistance states to electrochemical changes to gain a deeper insight into the SOT switching mode.

We compare core-level spectra of Hf-4f, O-1s and Ti-2p in device configuration and inspect the valence band (VB) spectra obtained from the bare film. Critically no changes in resistance state were observed by measuring the bare film with conductive AFM after changing the ferroelectric polarisation direction by PFM, indicating the critical role of the top electrodes in stabilising the SOT. Using the approach described in section 5.2, measuring the HAXPES spectra with thin TiAu top electrodes and on the bare film, the signal depth sensitivity is altered. The penetration depths were performed using the electron inelastic mean free path and are summarised in Table 5.1.

Sample	Energy (keV)	TiAu	YHO	LSMO	Max depth
YHO - Au	5.9	70-80 %	10-14 %	8-11%	7 nm into LSMO
YHO - PFM	5.9	N/A	47%	31%	Into NbSTO

Table 5.1: Estimated elemental signal contribution and electron escape depth in HAXPES experiments for areas under the Ti|Au electrode and the bare film.

The Hf-4f spectra are shown in Fig. 5.7 a). Both peaks can be fitted well with a single Voigt-function and their positions correspond to fully oxidised Hf^{4+}. Hence no evidence of substoichiometry is present and this does not change upon a change in resistance state. The lack of change in stoichiometry would therefore exclude homogeneous redox reactions occurring at the YHO surface or across electrode interfaces [266, 268]. Furthermore, no shift in peak position is evident, which is indicative of a lack of change in band bending, typically associated with charge trapping [269] or ferroelectricity-induced potential barrier changes [205]. However, the lack of change in the Hf-4f signal may not exclude redox reactions occurring. A conductive filament is typically only 10-100 nm in diameter, whereas the X-ray illuminated area is significantly larger with a spotsize of 100 μm. Therefore non-switching YHO may drown out the filamentary signal.

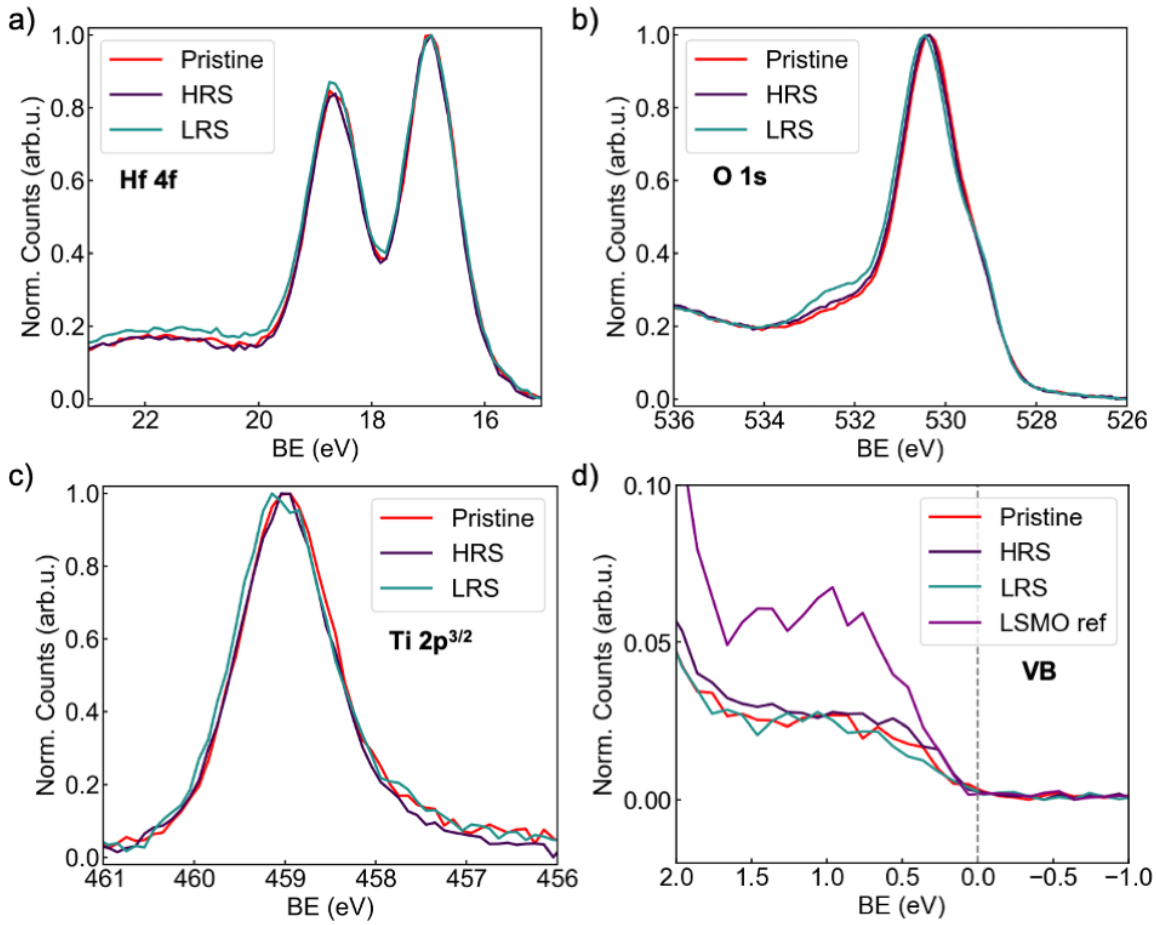

Figure 5.7: a)–c) HAXPES spectra measured at 5.9 keV underneath Ti|Au electrodes in the pristine, LRS and HRS for Hf-4f (b), O-1s (c), Ti-2p (d) spectra of the valence band (VB) without top electrodes spectra in the pristine, LRS and HRS state valence band (VB).

Conversely, O-1s spectra in Fig. 5.7 b) show significant changes upon resistance state reversal. The O-1s signal consists of 3 components, the primary metal-oxygen (primarily Hf-O) bonding at a binding energy of 530.2 eV, a 'non-lattice oxygen' (NLO) signal at 531.9 eV and a La-O shoulder at 529 eV. Each of the components is fitted with a separate Voigt function and allows for the relative quantification of the signal changes between resistance states. The Table 5.2 summarises the areal contributions to the O-1s signal, Hf-O, NL-O and La-O, and show significant relative changes between resistance states. These contributions are deconvoluted by fitting each component with Voigt functions after a Shirley background has been removed. The NLO component refers to oxygen species which are not bound to metal cations [270]. This signal doubles from the HRS to the LRS and is also visible in PFM-poled areas. Since this behaviour is visible in both non RS PFM-poled areas and

in RS device configuration, we conclude the NLO does not contribute to the observed RS response. The shoulder peak associated with La-O bonds, indicative of oxygen bound in LSMO, increases in the LRS and decreases in the HRS. This behaviour is not observed in the PFM-poled areas, suggesting that the change La-O is related to changes in resistance states, indicating the oxidation of LSMO in the LRS and reduction in the HRS. Considering that during the SET process, a negative voltage is applied at the top electrode, negatively charged interstitial oxygen (positively charged oxygen vacancies) would migrate toward (away) from the LSMO. The direction of oxygen is hence consistent with field-enhanced ionic transport.

	Hf-O	NL-O	La-O
Pristine	81.9	4.5	13.6
LRS	71.7	9.2	19.2
HRS	80.8	5.8	13.5

Table 5.2: Percentage contribution to the O-1s signal area in the pristine states, HRS and LRS.

Inspecting the Ti-2p core-level spectra, the peak position confirms that Ti remains fully oxidized in the Ti^{4+} state across both resistance states, as already indicated by ELNES for the pristine state. Again, no evidence of sub-stoichiometry is present. However, notably a 0.1 eV shift towards higher energy in the LRS compared to the HRS, indicating increased negative charge density, potentially due to a higher density of non-lattice oxygen (NLO) in the LRS. If the TiO_x were the primary resistance limiting element, it would be more oxidised in the HRS, whereas here we observe the TiO_x to be more oxidised in the LRS [108]. The observed redox changes in TiO_x are inconsistent with field-enhanced ionic migration. Instead, Joule heating-induced thermal effects, such as Soret thermophoresis, might drive oxygen migration away from the filament, since temperatures at filament tips can reach up to several hundred Kelvin at high power dissipation [271, 272].

Finally, the valence band (VB) in the PFM poled region is analysed. States near the Fermi level originate from the LSMO. Intriguingly, these states do not cross the Fermi level, indicating LSMO's semiconducting nature. Previous evidence of larger than expected depletion region widths at both LSMO interfaces is therefore corroborated. Based on the current-voltage (J-V) characteristics, energy loss near edge structure (ELNES), and hard X-ray photoelectron spectroscopy (HAXPES) data, it is hypothesized that the enhanced RS performance of the SOT containing a thin LSMO layer is due to a thickness-induced decrease in conductivity. The LSMO may act as a series resistor, setting a compliance current and preventing irreversible dielectric breakdown. Additionally, the LSMO may experience a larger voltage drop, enhancing oxygen exchange with YHO. Thickness-induced

crystallographic differences in LSMO may also influence the growth mode and the amount of monoclinic phase present in the YHO, affecting polarization magnitude and grain boundary density [158].

5.7 Conclusion

To conclude, we demonstrated that SOT is not dominantly driven by interfacial barrier changes from ferroelectric polarisation reversal because no evidence of a change in band-bending has been observed. Area dependence measurements indicated localised conduction paths in the LRS. However, no forming process was observed and the device was grown close to the LRS in the pristine state. This will be subject to further investigation. Furthermore, design rules were determined, which established that the Ti adhesion layer plays a critical role as an oxygen reservoir, whose capacity needs to be optimised to stabilise the SOT. Additionally, the thickness of the LSMO was determined to be important. Significant depletion regions in the LSMO were recognised and attributed to a degradation in conductivity in the LSMO. The precise role of the LSMO during the switching process will be discussed in the following section 6.5.

Chapter 6

Disentangling Resistance Contributions during Schottky-to-Ohmic Switching

Chapter Summary

This chapter present an impedance spectroscopy based analysis of the Schottky-to-Ohmic (SOT) switching mode. Two relaxations were identified and were attributed to the YHO film and the LSMO|YHO interface region. The pre-poling procedure and gradual changes in resistance during pulsed switching revealed that both the in both the YHO layer and the interface region contribute to the observed resistance switching response. The conduction in the pristine state was indicated to be confined to conductive paths, bypassing inter-grain transport. Furthermore the SOT is hypothesised to be stabilised due to an enhanced defect concentration at the LSMO|YHO when the thickness of LSMO is reduced. Transport analysis suggests that the current flow through the device is limited by a polaronic hopping regime.

Author contributions

I performed PLD growth, electrical characterisation and analysis.

6.1 Introduction

The previous chapter clearly demonstrated that a careful design of the YHO interfaces drives conductive channel formation and dissolution during the Schottky-to-Ohmic transition (SOT). Oxygen scavenging due to the Ti interlayer deposition and an LSMO depletion region had been identified as the main ingredients for the stabilisation of the SOT. Yet, a number of key questions remain, which have been grouped into two topics:
First, a microscopic understanding of the resistance switching processes. How is the pristine state different to the high resistance state (HRS) and low resistance state (LRS) - why does the pristine state occur in an intermediate resistance range? The SET process may be correlated to ferroelectricity, however the RESET is not and occurs in two separate stages - do multiple layers contribute to the resistance change?
Second, what is the role of the LSMO during the switching process? How does the depletion region participate during resistive switching? Why is the SOT only possible with thin LSMO? Does a metal-insulator transition within the LSMO contribute to the resistance change?

The device configuration used to achieve the SOT is rather complex; each of the layers within the stack can individually display a significant resistance change through a plethora of mechanisms. Nb-doped $SrTiO_3$ (NbSTO) as a substrate can show charge-trapping-based resistance switching, governed by imperfections at the interface with a metal electrode [106] or dielectric [107]. For LSMO it is well known that electronic correlations play a key role in its properties, e.g., to induce metal-insulator transition (MIT) [151]. The MIT can also be tuned through magneto-electric coupling, where ferroelectric charge or strain mediate the resistance change [273], or magneto-ionic coupling, by interfacial redox reactions [163]. Furthermore, the use of Ti as an interlayer has the potential to reversibly oxidise and form an insulating tunnel barrier for electrons [108]. Finally, the switchable ferroelectric polarisation may cause an additional resistance-changing effect [57, 65, 239]. Therefore, the SOT can potentially be governed by multiple resistance switching effects in addition to a localised breakdown. These cannot be separated solely by quasi-static IV analysis.

Impedance spectroscopy is a widely used technique to assess resistance and capacitance changes across a wide frequency range [274]. An impedance spectrum typically contains multiple components each with a characteristic relaxation frequency, which is visible as a semicircle in the Nyquist plot or a change in slope in the impedance formalism. Elements such as grains, grain boundaries, interface layers or mobile domain interfaces can be separated. This technique therefore allows insight into which components govern the overall device resistance. Coupling impedance spectroscopy with variations in stack chemistry and temperature can therefore become a powerful combination to assess memristive switching mechanisms. In this chapter, the resistive switching behaviour of the SOT and its associ-

ated switching modes are disentangled by means of impedance spectroscopy. Successive switching experiments helped identify and correlate the nature of the pristine state and revealed stable intermediate resistances between LRS and HRS. The critical role of the LSMO to the SOT switching was identified and its contribution to reversible and irreversible resistance changes was dissected. Changes in film chemistry allowed to pinpoint the origin resistance changes and identify the underlying conduction mechanisms, which was aided by temperature-dependent experiments. All impedance spectra were obtained at frequencies f between 1 MHz - 100 Hz at an AC amplitude of 100 mV using an Ametek Solartron impedance analyser.

6.2 Model Development

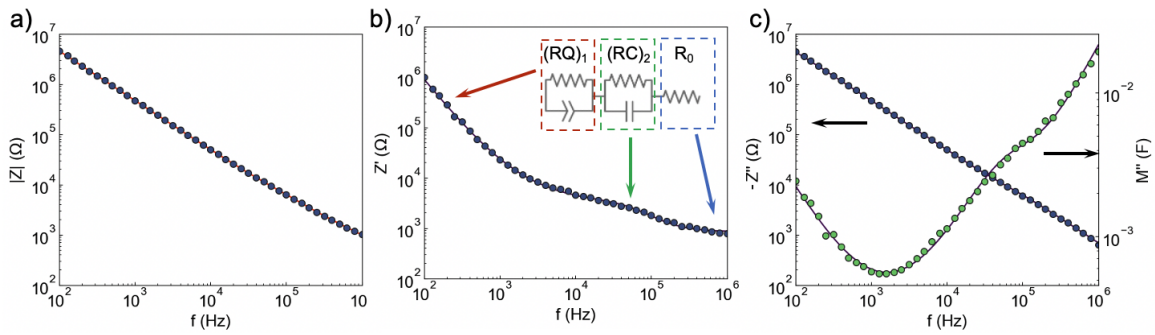

Figure 6.1: a) Impedance magnitude $|Z|$ with Kramers-Kronig transform b) real impedance Z' with equivalent circuit fit c) Imaginary impedance Z'' and modulus M'' with equivalent circuit fit.

In the first instance, a device was poled into the HRS and impedance spectra were measured, which are shown in Fig. 6.1. To verify the spectra were collected in a stable, causal and linear perturbation regime, a Kramers-Kronig (K-K) transform was applied [275]. The resulting data is plotted in Fig.6.1 a) in red. The K-K transform shows excellent agreement with experimentally acquired $|Z|$ shown in dark blue. A small mean squared weighted deviation of $\chi^2 = 0.0054$ was obtained, indicating the experimental conditions are suitable for the subsequent analysis.

The development and assignment of an equivalent circuit to describe impedance data is a crucial step in the analysis. However, care needs to be taken that the model is both physically relevant and does not overfit the data. The approach taken here was to first compare the real part Z', Fig. 6.1 b), and imaginary part Z'' impedance formalism with the modulus formalism M'', Fig. 6.1 c), as defined in section 3.4. The combined use of Z'' and M'' emphasises

different constituents, since their magnitude scales with the largest resistance and smallest capacitance respectively [186]. Once these relaxations are identified, they can be expressed as equivalent-circuit elements and subsequently correlated to layers within the device stack. Inspecting Fig. 6.1 b) for the Z', two relaxations are visible, a low-frequency relaxation, a drop in Z' between 10^2 to 10^3 Hz and a high-frequency relaxation, a plateau between 10^3 and 10^5, which subsequently drops further in magnitude. The RC time constant of the low-frequency relaxation is outside of the measurement range. Conversely, the imaginary part, Z" in 6.1 c), only shows a single frequency dependent power-law dispersion f^{-n}, which scales with n = 0.95 and corresponds to the low-frequency relaxation. The exponent of n indicates the system only deviates slightly from the ideal Debye-relaxation of n = 1. The combination of Z" with M" highlights the high-frequency relaxation as a shoulder peak. The rise of M" towards the high-frequency limit suggests the presence an additional relaxation with a small capacitance outside of the measurement range.

From these relaxations, we develop an equivalent circuit model, which is illustrated in the inset of Fig. 6.1 b). The low-frequency relaxation is described by $(RQ)_1$, corresponding to a parallel resistor and phase element (CPE), with the free parameters Q and α. The relaxation is attributed to the YHO layer, since its magnitude correlates with YHO film thickness, as shown in Appendix B.2. The high-frequency relaxation around 10 kHz is modelled as the $(RC)_2$ element and corresponds predominantly to the YHO|LSMO interfacial layer, as will be discussed in section 6.5. Finally, the series resistance R_0 is used to model resistances from measurement cables and electrode contacts. Specific relaxations from the NbSTO substrate, the TiO_2 interlayer or Au top interface are not explicitly accounted for. Relaxations from these layers may be present in the R_O or $(RC)_2$ but could not be separated. Fit parameters are summarised in Table 6.1. The results of the fitting will be discussed in more detail while comparing to the LRS additional switching modes in section 6.3.

	R_1 (MΩ)	Q_1	α_1	C_1 (nF)	R_2 (kΩ)	C_2 (nF)	R_0 (kΩ)	χ^2
As Grown	-	-	-	-	7.16	0.319	0.864	0.12
Pre poled	-	-	-	-	72.8	0.375	0.723	0.25
HRS	24.9	$3.89 * 10^{-10}$	0.98	0.361	2.35	0.965	0.868	0.028
LRS	-	-	-	-	0.18	0.119	0.868	0.24

Table 6.1: Summary of impedance fit parameters for the first 4 resistance states during the SOT.

In previous reports of using impedance spectroscopy to investigate ferroelectric HfO_2, a capacitor was used to describe the ferroelectric film and the use of the constant phase element (CPE), was reserved to describe interfacial layers [276, 277]. Here, we use the CPE to account for the departure from ideality in the frequency dispersion of Z". These dispersions can stem from dispersions in the dielectric permittivity, which is caused by the pinning of domain walls in a random energy landscape, particularly prevalent in ferroelectric thin films. [184, 195, 278] Yet, domains do not necessarily need to be ferroelectric but can more generally relate to other mobile interfaces such as the presence of interphase boundaries inside individual grains [279]. Becker et al. developed an equivalent circuit element to describe domain wall pinning and extract physically meaningful parameters [194]. We performed a fit of the HRS impedance data using the domain wall pinning element Z_{DWP}, see Fig.B.1 in the appendix, which showed excellent agreement with the experimental data and gave fit parameters similar to those obtained in ferroelectric HfO_2 based systems. This is a strong indication that the low frequency feature in the HRS and its frequency dispersion do indeed originate from the YHO film. Yet, Z_{DWP} is mainly used in a Rayleigh analysis to assess domain wall mobility by varying the AC amplitude [195, 278]. We attempted such an analysis, however due to sample degradation during high AC amplitude measurement, this was not considered further. For the sake of simplicity, we therefore resort to the CPE to describe observed dispersion. Lastly, attempting a fit to the above spectrum while accounting for the high-frequency relaxation with a CPE and the ferroelectric with a conventional capacitor, resulted in large errors and a CPE α exponent between 0.65-0.7, which was deemed to be very low. Therefore the CPE was chosen to represent the low frequency relaxation, whereas the a capacitor was used for the high frequency relaxation.

We now consider the equivalent capacitance of Q_1 and the calculated dielectric permittivity from the CPE fit of the YHO layer. The fit parameters Q_1 and α_1 of the CPE were converted to an equivalent capacitance, using $C_1 = \frac{(R_1 Q_1)^{\alpha}_1}{R_1} = 3.61 * 10^{-10}$ F and thus a permittivity of 14.5 is calculated for the YHO layer. This value is significantly lower than anticipated for the ferroelectric HfO_2 phase. Ordinarily, the dielectric constant in doped HfO_2 increases across the monoclinic (19-25), ferroelectric orthorhombic (25-33) and tetragonal phase (24-57). [248, 280, 281] A low permittivity is often associated with an increased fraction of the monoclinic phase present in the film [282]. Yet, there is no evidence for a significant concentration of the monoclinic phase present in this film from either TEM nor XRD, similarly to other epitaxial ferroelectric HfO_2 systems [283]. Furthermore, the permittivity is low even for a purely monoclinic phase, which suggests an extrinsic origin to this phenomenon. Support for this hypothesis is illustrated in Appendix B.3, where a

dopant-free HfO_2 film with visibly larger monoclinic phase content, has a larger permittivity than the present film.

One could consider an additional capacitance in series with the film, which has not been accounted for within the impedance model. These could originate from space-charge regions, such as the NbSTO|LSMO interface, or thin insulating oxide films within the stack, such as TiO_2. However, these layers are extremely thin, thus would lead to a very large capacitance. Yet, considering a large series resistance of R_0 = 838 Ω and a large peak in the M" formalism at $f > 1$MHz, could provide weight towards this hypothesis. Equally, the film possesses a high density of columnar grains with associated grain boundaries, which could adversely affect the permittivity [284, 285]. Finally, incorrect assumptions about stack geometry, particularly the effective electrode size in films with conductive filaments, can have a dramatic impact. However, even on devices, which did not show resistive switching behaviour, data not shown, the permittivity remained in a similar range. However, it is not possible to differentiate between these options.

6.3 Switching Modes

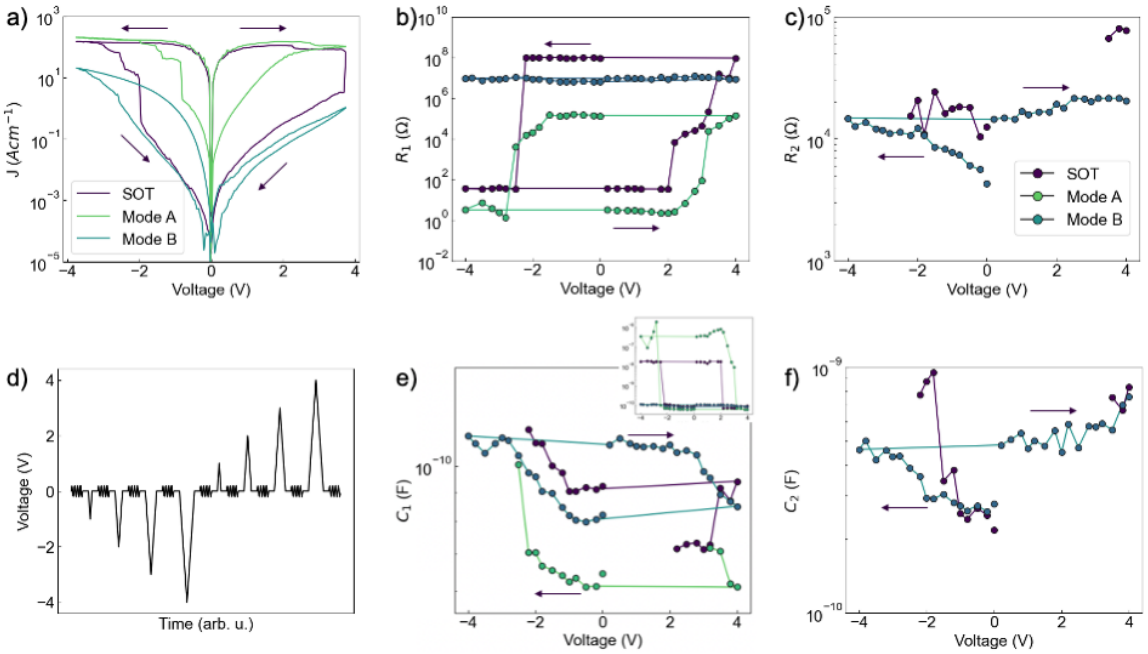

Figure 6.2: a) J-V relation of the SOT, RS Mode A and Mode B b) Extracted R_1 c) Extracted R_2, d) Illustration of measurement scheme e) Calculated capacitance C_1 f) extracted capacitance C_2.

The developed impedance model can now be applied to study the stages of resistance change during SOT. Of key interest is how each layer contributes to the switching process. It is important to note that RS mechanisms were not homogeneous across multiple devices on a single film. Different switching modes can be observed in addition to SOT. The current density - voltage (J-V) curves of the two most prominent additional modes, A and B, are illustrated in 6.2 a). Each switching mode has the same switching polarity and can occur either individually or on the same device, where the SOT turns into such a switching mode. Their co-occurrence indicate close relation between the modes and may allow to simplify and disentangle the complex switching processes observed here. To achieve this, separate devices exhibiting each of these modes were poled into intermediate states using a measurement scheme illustrated in Fig 6.2 d). Here, voltage sweeps of increasing amplitude were applied to the device and an impedance spectrum was measured after each voltage sweep.

We begin by first considering the SOT reset to a HRS. As small negative voltages are applied, both the extracted resistances R_1 and R_2 in Fig. 6.2 b) and c) remain roughly constant. Yet, both capacitances C_1 and C_2 increase, where the C_1 increases only slightly and C_2 more than quadruples, as seen in Fig. 6.2e) and f) respectively. Subsequently, a sharp SET occurs, where the resistance drops by 6 orders of magnitude and only one relaxation remains visible in the impedance spectrum. Concomitantly, a sharp rise by 2 orders of magnitude in C_1 is observed, as shown in the inset in Fig. 6.2 e). During the reset process, as the device is poled with positive voltages, the R_1 increases gradually up to ~ 100 kΩ, while still being modelled as part of a single RC element. Finally, as the poling voltage increases further, a sharp reset occurs, rapidly increasing the device resistance and restoring both the YHO and interface relaxations.

Next, mode A is examined, which has a LRS of a similar magnitude the SOT. In the $J-V$ curve sharp SET process is evident at negative voltage, albeit at significantly lower magnitude than the SOT. Neither the HRS nor the LRS of mode A have currents dependent on the electrode area, indicating localised conduction in both resistance states, see Fig. 6.3 a). Similarly, a gradual RESET process is evident around 2.5 V comparable to the SOT. However,the sharp RESET process at 3.5V is missing. Each impedance spectrum of mode A can be satisfactorily modelled only using a single RC-R element, whose resistance is in a similar magnitude to the LSMO|YHO interface layer, R_2, observed during the SOT. The intermediate states impedance of mode A in resistance and capacitance overlap closely with those observed during the SOT.

In contrast to the SOT and mode A, mode B switches more gradually and operates in the HRS range of the SOT. In addition, the $J-V$ curve is more asymmetric, where the majority of the hysteresis occurs at negative polarity. Critically, as with the SOT, only the LRS of

mode B is not dependent upon electrode area, indicating a similar filamentary process, see Fig. 6.3 b). However, the reversible changes in R_1 and C_1 are significantly smaller than those in the SOT and A modes. Interestingly, when the device is first biased negatively, both R_2 and C_2 increase. However, on application of an increasing positive bias, the initial R_2 and C_2 values are not recovered and even increase further. This is in contrast to R_1 and C_1 which fully recover their original values and are reversible. This would be indication of an irreversible process taking place within the interface layer, which is discussed further in section 6.5.

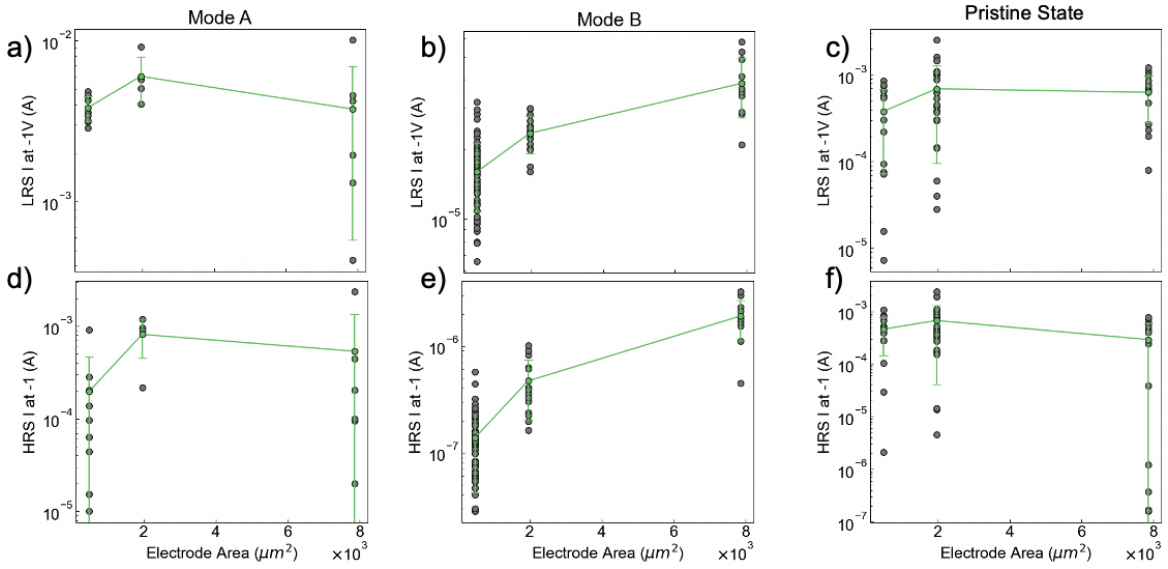

Figure 6.3: Area dependence of currents in the a),d) mode A b),e) mode B and c),f) the pristine state.

Based on these observations a model of the switching processes occurring during the SOT is proposed, beginning with mode A. The similarity in $J-V$ and the LRS magnitude, suggests that the mode A and the SOT have a common LRS. Impedance spectra of mode A can be modelled with a single RC-R element and the extracted resistance and capacitance are of similar magnitude to R_2 and C_2 attributed to the LSMO|YHO interface within the SOT mode. However, a sharp reset at high voltage is not observed and the HRS of the SOT is not fully recovered during mode A operation. We therefore consider mode A to be an incomplete RESET mode of the SOT. Since conduction current in mode A is independent of electrode area in both resistance states and the current limiting R_1 is not observed in mode A, we propose that the YHO layer here is shunted by a filament or conductive grain boundaries, which remain present during switching operation. The resistance changes are solely governed by changes in the LSMO|YHO interface layer.

The observed phenomenona can be described by a virtual cathode model in filamentary systems[70, 91, 286, 287]. After a forming process, a strong filament through the insulator remains and the resistance changes occur solely between a filament tip and electrode-insulator interface region [71]. The sharp SET and gradual RESET are also typical features of filamentary systems. During the SET operation at negative bias, possibly a combination of self-reinforcing field-enhanced drift and Soret thermodiffusion-induced migration of oxygen vacancies towards the filament tip causes this to grow and pierce through the interface region and shunting the electrode contact. The residual mobile oxygen is then absorbed by the LSMO as observed by HAXPES, in section 5.6. The resistance in the LRS is then limited either by a thin metallic filament or the contact resistance of the electrodes. Conversely, during the RESET operation, a positive bias causes positively charged oxygen vacancies to migrate away from the filament tip and into the LSMO.

The SOT is described as an extension of mode A, where the LRS of both modes are the same. The SOT shares a gradual RESET operation around 2V with mode A, which restores the interfacial layer. However, at high positive voltage, an abrupt drop in current also restores the resistance of the YHO layer. This is indicated through the current in the HRS of the SOT being dependent on the electrode area and the impedance spectra showing two relaxations, indicating homogeneous conduction across the YHO. The sharp nature of the resistance change suggests a sudden rupture of the conductive paths in the YHO layer. A possible origin of this may be the significant Joule heating present at high currents and voltages, which may cause thermal Fick diffusion to alleviate concentration gradients [288] and dissolve local conduction paths. The SET process on the other hand is also sharp and breaks through the YHO and LSMO interface simultaneously and may be aided by ferroelectric polarisation reversal, as discussed in section 5.3.

6.4 Pristine State and Pre-Poling

Having identified the nature of the switching process during full SOT operation, we proceed to investigate the low resistance of the pristine state and the initial poling stages. The *pre-poling* process was defined as the application of a full bipolar voltage sweep necessary before the commencement of SOT operation. Fig. 6.4 a) shows the pre-poling procedure. Successive half-cycle operations are numbered 1-4, the corresponding $J-V$ relation is displayed in 6.4 b). Before each half-cycle, an impedance spectrum is measured, which is shown in Fig. 6.4 c). The fit parameters obtained from the impedance spectra are summarized in Table 6.1 and displayed in 6.4 d). The device is first poled with negative bias and the current amplitude rises to an intermediate level between LRS and HRS. The reverse sweep, -4V $\rightarrow$ 0V, shows a

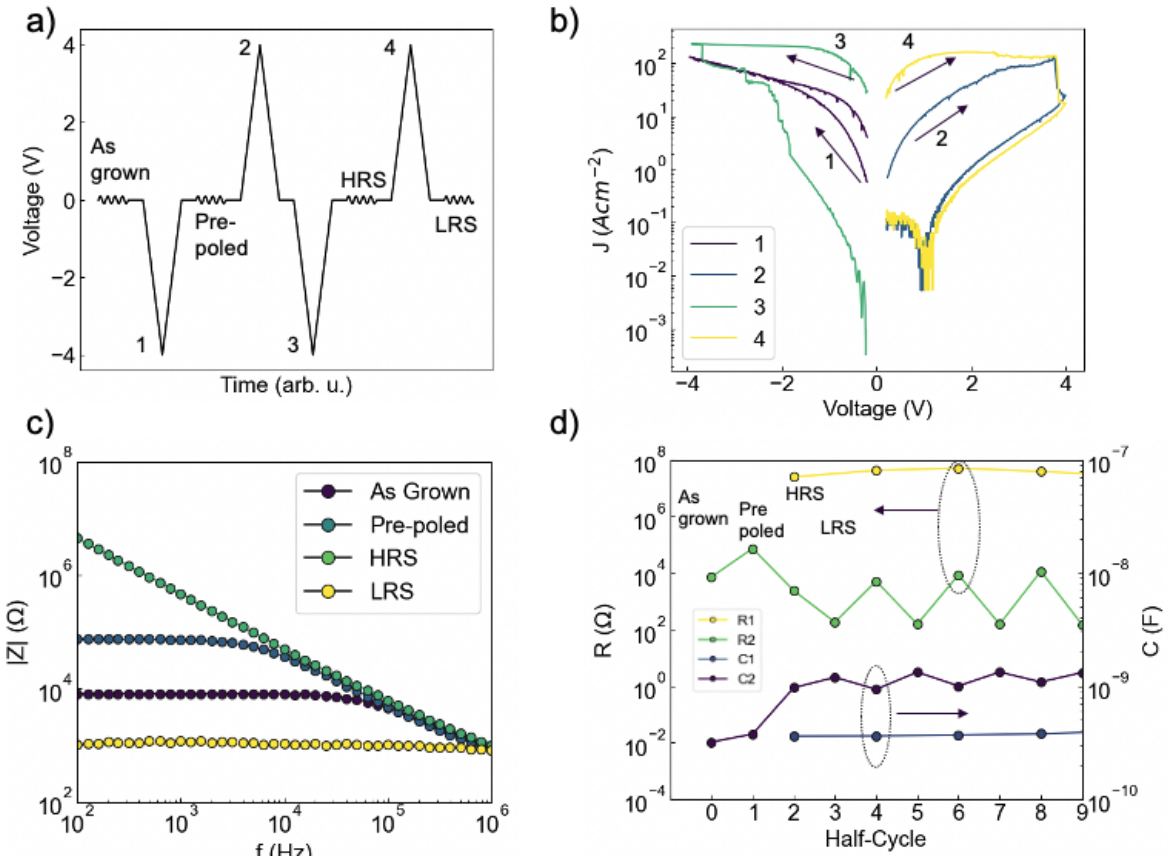

Figure 6.4: a) JV Curve showing the pre-poling stages before the SOT switching begins b) measurement methodology c) Z' of the pre-poling stages d) Z" of the pre-poling stages.

small hysteresis, with the current of the down sweep being lower than the up sweep. Next, the device is biased positively, which occurs smoothly until a sharp drop in current is observed around 3.8V, resulting in the HRS. The positive bias sweep shows similarity to the RESET process observed during SOT, and possibly occurs through a similar process. However, the device is not fully in the LRS, suggesting a current limiting element remains. SOT type switching resumes after the pre-poling process. Considering now the impedance spectra of the pristine and the pre-poled state. In contrast to the HRS, both spectra can be fitted satisfactorily with a single RC-R element. The Z_{DWP} was unsuccessful in fitting neither the pristine nor the pre-poled state and the current of sweep 1 does not scale with the electrode area, see Fig. 6.3c) and f). This indicates that the observed pristine and pre-poled impedance do not correspond to the grains of the YHO layer. Following the negative pre-poling sweep, pristine $\rightarrow$ pre-poled, a small increase in capacitance and one order of magnitude increase in resistance is observed. After the positive sweep, both the resistance and capacitance of the

pre-poled state decrease significantly and a low-frequency relaxation emerges, the HRS is obtained.

Fig. 6.5 displays the transition from the pre-poling stage, shown in red, over the SOT to mode A over multiple switching cycles. As visible in Fig. 6.5a) the current density during the pre-poling stage clearly corresponds to the HRS of mode A and is consistent with area dependence measurements. Inspecting the phase of the impedance spectra in Fig. 6.5 b), the phase through of the pristine state is similar to the mode A HRS. The evidence strongly suggests that in the pristine state, the LSMO|YHO interface is the current limiting element. Furthermore, both the real and imaginary part of the impedance show an increase in the magnitude of the LSMO|YHO feature, shown Fig. 6.5 c) and d) respectively, during consecutive cycling. Similarly to the increase in both resistance and capacitance observed for the mode B switching, this suggests a degradation of the interface properties and is further discussed in section 6.5.

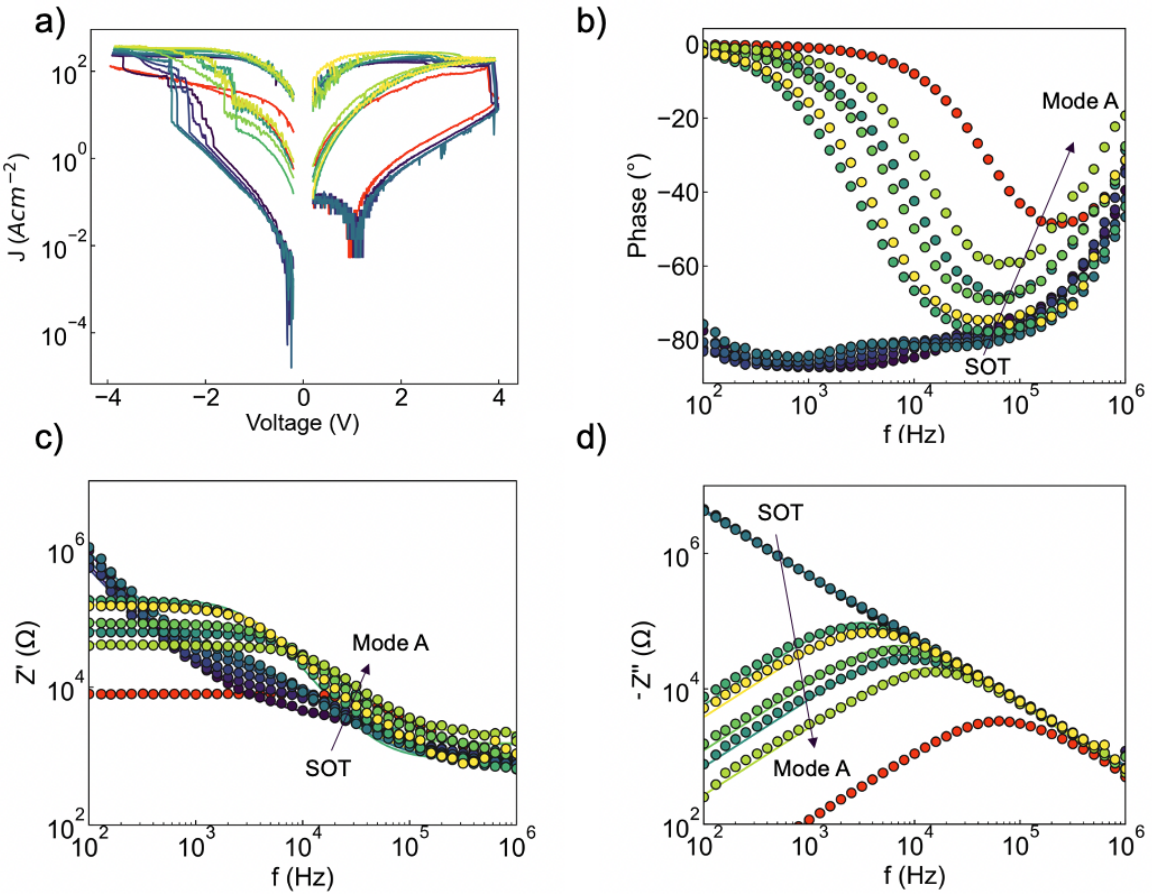

Figure 6.5: 20 consecutive switching cycles from pre-poling (red) to SOT switching (blue) and to mode A switching (green-yellow) are shown for a) JV, b) the impedance phase of the HRS, c) real impedance Z' of the HRS and d) imaginary impedance Z'' of the HRS.

A resistive switching mechanism with a pristine state between the LRS and HRS is in stark contrast to typical filamentary systems. These usually require a forming process. Several approaches have been employed to mitigate the forming process in HfO_2, such as significantly increased bottom electrode roughness, thereby increased grain boundary density [97, 98] or oxygen deficiency [289]. Yet, these devices were all found to be grown in the HRS. The coexistence of ferroelectric and filamentary switching has been reported on epitaxial and polycrystalline hafnia systems [216, 243]. Here again, the devices are grown in the HRS and spontaneously switch towards filamentary resistive switching. Recently, grain-boundary conduction through epitaxial monoclinic and oxygen-deficient rhombohedral HfO_2 was examined by conductive atomic force microscopy (cAFM). Conductive grain boundaries were found to exist regardless of crystalline phase and oxygen stoichiometry [249]. We therefore considered the conductivity of the bare film using cAFM, data not shown. No evidence of conductive grain boundaries was detected. Furthermore, poling the ferroelectric using PFM, did also not result in a measurable change in cAFM conductivity, neither on grain, on grain-boundary nor in-between ferroelectric domains. Thereby, we exclude major differences in grain boundary and domain-wall conduction to the YHO grains/domains. Intriguingly, a similar pristine state was reported in a CeO_2-HfO_2 phase segregated vertically aligned nanocomposite [290]. The material boundaries served as mixed electronic-ionic conduction paths. Yet, no evidence for HfO_2-Y_2O_3 phase segregation has been observed in the SOT device stack. Incoherent crystallographic phase boundaries between monoclinic and orthorhombic $HfZrO_4$ phases had been proposed to serve as electronic and ionic conduction paths and lead to significant RS hysteresis [244, 245]. We examined a device stack with undoped HfO_2, which displays a significant monoclinic and orthorhombic phase coexistence, Fig. B.3. However, changes in current density or SOT mode yield were not significantly different compared to samples with 7 mol% Y doping. The conductivity within the pristine state possibly arises as a result of the top-electrode surface interaction in addition to a high density of grain boundaries, which may scavenge oxygen from pre-existing grain boundaries, rendering these more conductive. However, it cannot solely originate from the potential oxygen-scavenging properties of the TiO_2, since this intermediate pristine state has been observed when using Pt electrodes, see section 5.3. Yet, while care was taken to ensure minimal kinetic energy during contact sputtering, slight sub-optimal conditions during deposition can still result in significant defects, which promote resistance-switching behaviour [106].

Finally, an increase in resistance after negative pre-poling cannot be attributed to a redox reaction between the TiO_2 adhesion layer and the YHO film: Both electron energy loss spectroscopy (EELS) and hard Xray photoelectron spectroscopy (HAXPES) measurements

show already oxidised TiO_x in the pristine state. This would leave the LSMO|YHO interface to be responsible for the change in resistance. One could consider the field-enhanced migration of oxygen anions across the LSMO|YHO interface. Since the resistance of LSMO is highly susceptible to a change in oxygen stoichiometry, an O deficiency can cause a significant increase in resistance. [162, 163]. Here positive (negative) bias applied at the top electrode would let oxygen anions migrate away from (towards) the LSMO bottom interface. However, this does not correlate with the observed behaviour here. Next, a ferroelectric field effect on the LSMO can be considered. Applying a positive (negative) bias, switches the ferroelectric polarisation toward (away from) the LSMO, having a positive (negative) surface charge on the bottom interface, causing the holes in the LSMO to deplete (accumulate). This again does not correlate with the observed behaviour. The observed resistance changes may be explained by the filling and emptying of trap states at the YHO|LSMO interface, where positive (negative) bias causes charge carriers to be released (trapped) at the interface, enabling (preventing) further current flow and thereby decreasing (increasing) the resistance. Therefore, charge trapping is a possible explanation for the resistance change during the first negative bias sweep.

6.5 LSMO Thickness Dependence

Each of the previous sections has highlighted the importance of the LSMO|YHO interface in participating in the SOT switching operations. This is now examined in more detail. A facile method to tune the electrical properties of the LSMO is to reduce the film thickness during growth resulting in the electrical dead-layer playing a more pronounced role and the loss of the metallic properties of LSMO [151]. The device geometry so far used a LSMO film thickness of 28 unit cells (uc), which exhibited in a significant depletion region at the LSMO|YHO interface, as shown by ELNES in section 5.5. It was attempted to enhance or suppress this depletion region by growing a set of films with three different thicknesses of LSMO: 10, 28 and 50 uc.

The structural differences between the three films are portrayed in Fig. 6.6 a). Each of the $2\theta\omega$ scans shows the dominant YHO [111] peak just below 30°. The YHO d_{111} lattice parameter increases slightly (3.006 Å→ 3.02 Å) with increasing thickness of LSMO. Laue oscillations are observed for each peak, indicating high crystalline quality and no evidence of parasitic phases. In contrast, the LSMO d_{001} lattice parameter decreases with increasing LSMO film thickness (3.91 Å → 3.86 Å). Intriguingly, the changes in the lattice parameter occur in opposite directions. Next, the permittivity-voltage hysteresis at 1 MHz is examined in Fig. 6.6 b). The characteristic ferroelectric butterfly loop is still present in

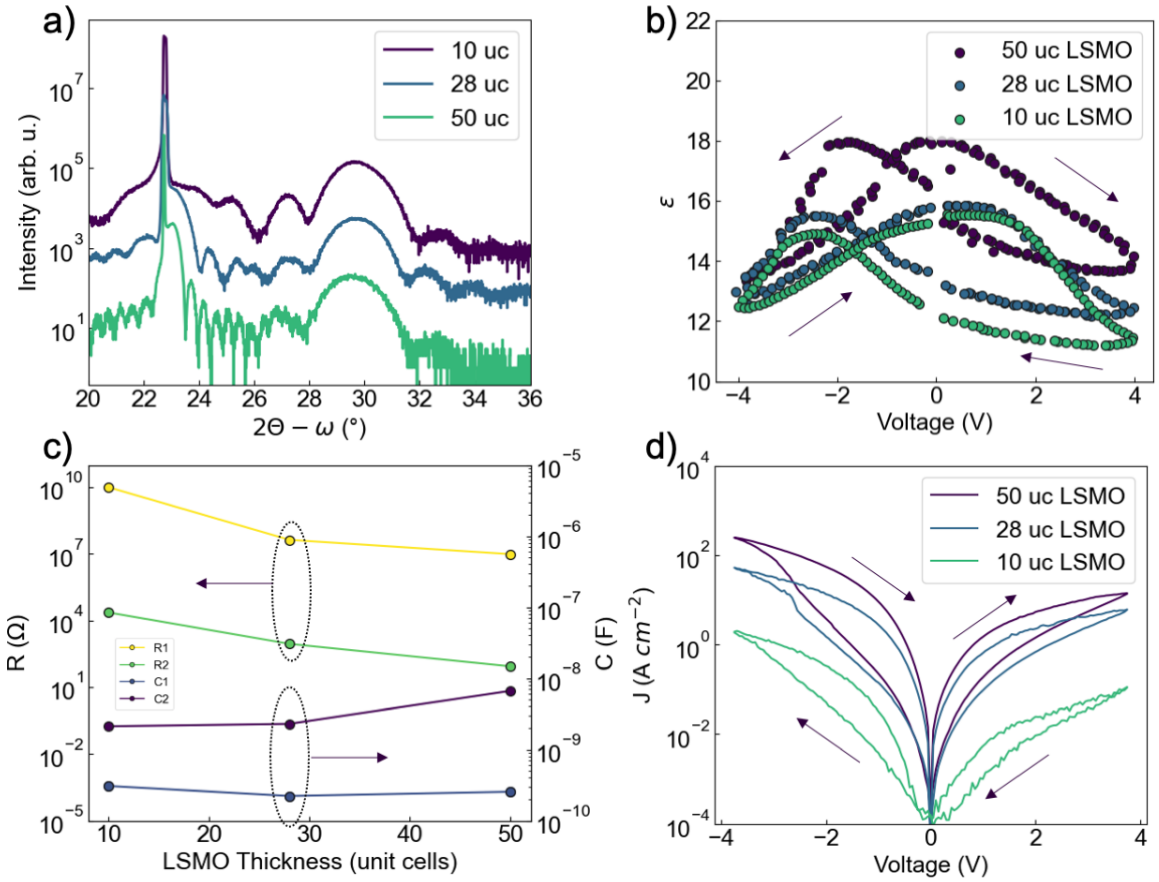

Figure 6.6: a) $2\theta\omega$ scans for device stacks with different LSMO thicknesses b) Permittivity-Voltage scans c) Capacitance and resistance extracted from impedance measurements d) J-V relation.

all three devices, indicating that at this frequency, the system can be considered as a metal-ferroelectric-metal structure. Metal-ferroelectric-semiconductor type permittivity-voltage relation with characteristic accumulation, depletion and inversion regimes of the capacitance are not observed here [291]. The saturation permittivity at 4 V decreases with decreasing LSMO film thickness. Furthermore, the loop asymmetry and tilt increase towards positive voltage. Equally, the switching voltages increase significantly, 1 V on positive polarity and -0.75 V on negative polarity. Finally, the imprint field becomes more significant as the thickness of LSMO is decreased. Further insight into the electronic properties is shown by the extracted resistances and capacitances from impedance spectroscopy. Fig. 6.6 c) clearly shows that both R_1 and R_2 decrease with increasing LSMO thickness. The C_1 on the other hand, remains roughly constant, while C_2 increases significantly. Finally, the $J-V$ relation of the devices is shown in 6.6 d). The SOT could not be stabilised in the device stack with 50 uc of LSMO, only mode B switching was observed. Similarly to the 50 uc LSMO sample, a

device grown on undoped STO with 28 uc LSMO cannot stabilise the SOT, data not shown. Furthermore, impedance spectra still displayed the high frequency relaxation. Hence, the relaxation does not correspond to the NbSTO|LSMO interface. For sake of consistency, 10 mode B devices from each film were averaged and are displayed. It is clearly visible that J decreases significantly, with decreasing LSMO film thickness. The static properties of an increase in R_2 with decreasing LSMO thickness are in line with expectation.

The LSMO film thickness therefore has a significant impact on the electronic properties of the device stack and a slight change structurally. One could consider if the electronic changes originate from structural changes. This may be influenced by a domain-matching epitaxy mechanism or complex chemical reconstruction at the interface [141, 259]. LSMO transitions from an insulating paramagnetic to a metallic ferromagnetic state with increasing film thickness, which is accompanied by hierarchical strain relaxation mechanisms. [157] These relaxation mechanisms are reported to occur from a small thickness, 2.5nm (7 uc), where the film consists primarily of an electronic dead layer and energy is gained by removing orbital degeneracy, concomitantly changing the Mn oxidation state. As the thickness increases beyond 10nm (26 uc) energy is gained through the compression of the octahedral framework, whereas beyond 25nm (64 uc) the main relaxation mechanism occurs through octahedral tilts. These thickness-dependent transitions simultaneously manifest themselves in a change in symmetry from a monoclinic tilt to a rhombohedral distortion [158], evident though a reduction in the [001] out of plane lattice parameter of LSMO, which are of similar magnitude to those observed here. The increase in YHO d_{111} with decreasing LSMO thickness may indicate a change in the rhombohedral distortion of the YHO. Although the changes in the YHO d_{111} are very small and would require a comparison between in plane and out of plane lattice parameter to quantify a subtle change in rhombohedral distortion. A correlation between a rhombohedral distortion in LSMO influencing the rhombohedral distortion of the YHO is outside the scope of this work, is further complicated by the challenge of the definite YHO phase assignment, as discussed in the appendix A.1 and would require a precise measurement of rhombohedral distortion of the LSMO. Nevertheless these results point towards the subtle but important role of symmetry requirements in stabilising the polar phases in hafnia [292, 293].

Next, the changes in the permittivity-voltage relation are consistent with a more significant p-type depletion capacitance within LSMO at the YHO|LSMO interface [247], as similarly observed for the extracted capacitances from impedance spectra. The internal carrier concentration of LSMO decreases with decreasing film thickness, consequently decreasing the depletion capacitance [294]. Yet, the large magnitude of the internal bias field or imprint field needs to be considered, as it is significantly larger than in comparable structures with Pt

electrodes [216, 295]. First, the direction of the field is consistent with the work-function difference between LSMO and Au. However, internal fields are complex and can have a variety of origins, from interface-trapped charges, pinned domains, oxygen deficiency or charged grain-boundaries [246, 296–299]. This again is consistent with the oxygen-deficient interface as observed by ELNES in section 5.5. Interestingly, within the impedance spectra, the resistance of the YHO layer, R_1, and the interface region, R_2 change concomitantly. The increase in R_2 was discussed previously. However, an increase in R_1 is unexpected. One possibility is to apply the interpretation of the pristine state, discussed in section 6.4. Here the interface region can act as a current blocking layer to grain boundary leakage current [244].

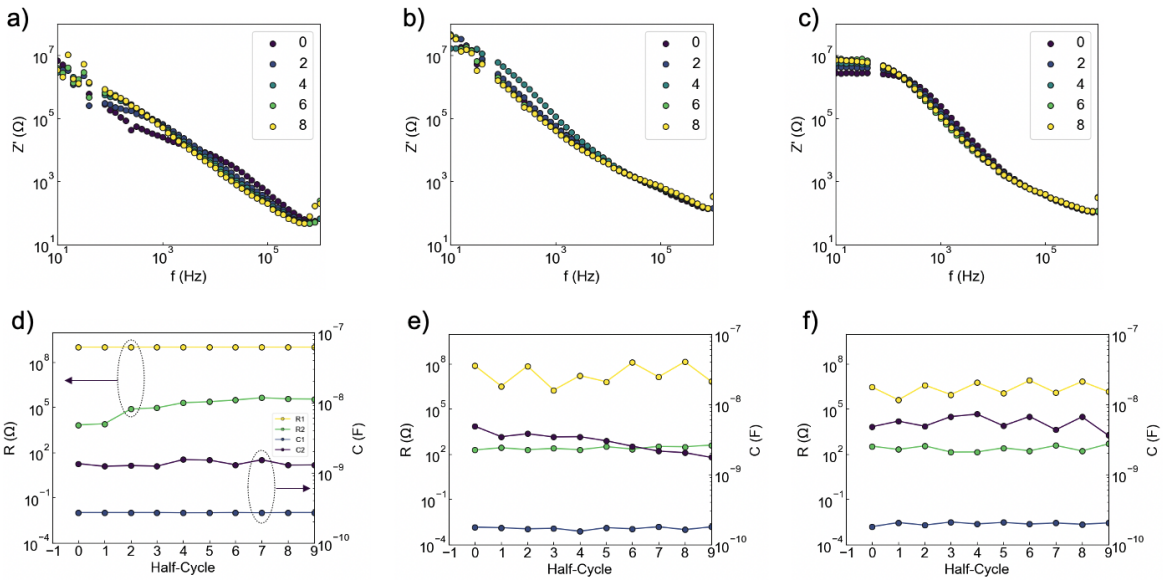

Figure 6.7: a-c) Z' of the HRS of devices with different LSMO thicknesses, d)-f) Extracted resistances and capacitances during the first 10 half-cycles of switching for a),d) the 10 uc LSMO device b),e) the 28 uc LSMO device c),f) the 50 uc LSMO device.

We now consider the dynamic properties of the device stacks and how impedance changes across multiple mode B switching cycles. Fig. 6.7 a), b) and c) show an increase in the high-frequency regime in Z' of the HRS during cycling for the 10, 28 and 50 uc LSMO HRS respectively. The Z' was chosen, since in Z", R_1 masks changes in R_2, which also translates into the $|Z|$ magnitude. The extracted parameters during cycling are shown in d), e) and f) for 10, 28 and 50 uc LSMO. Similarly to section 6.3, an irreversible process occurs during switching, which increases R_2 over time. Over 10 half cycles, the R_2 increased 5200% in 10 uc LSMO, 210% in 28 uc LSMO and only 42% in 50 uc LSMO. Therefore, not only is the R_2 larger in thinner LSMO but change in R_2 is much more pronounced during switching.

This suggests that thinner LMSO *participates* more during resistance switching. Comparable cycling related phenomena have been observed by other groups on epitaxial LSMO|HZO device stack, such as a *training* effect [245] or the lack of RS endurance [216]. The increase in participation likely originates from a higher defect density at the top surface of the LSMO. As epitaxial films get closer to the substrate interface, strain can no longer be accommodated elastically and defects form. Apart from the previously mentioned symmetry and tilt changes, defects such such as oxygen vacancies, cation-segregation [300, 301], inter-diffusion [302] and misfit dislocations can occur [95]. Each of these features can contribute to the dead-layer in LSMO, which dominates the electronic properties of the film at reduced thickness [156]. The tensile strain and defects not only make the LSMO more resistive, but also have been shown enhance oxygen surface transfer [303]. A larger concentration of defects in thinner films may therefore facilitate oxygen exchange across the LSMO|YHO interface, which has been shown by HAXPES in section 5.6 to play an important role during the SOT. Finally, the cycling induced resistance increase could therefore be related to an agglomeration of oxygen vacancies within the LSMO, which in turn makes the material more resistive, and would be consistent with the smaller oxygen affinity of LSMO when compared to YHO [103].

6.6 Temperature Dependence

The measurement of temperature-dependent impedance spectra is a critical step in evaluating the transport phenomena within a device. Furthermore, it serves to validate the assignment of equivalent circuit elements to layers within the device stack [186, 304]. It is widely known that LSMO undergoes a metal-to-insulator transition (MIT), which occurs at a Curie temperature $T_{C,MIT} \sim 369$ K in bulk crystals [150]. As described in section 2.3, the $T_{C,MIT}$ decreases in thin-films due to a magnetic and electronic dead-layer playing a more significant role. Furthermore, when interfaced with a ferroelectric oxide, the $T_{C,MIT}$ can shift through a plethora of mechanisms, which include the ferroelectric field effect [305], piezoelectric strain [306] or oxygen ion exchange [162, 163]. The previous sections highlighted the significant role of the LSMO bottom electrode in stabilising and participating during the SOT. The question arises whether the RS behaviour is influenced by a metal-insulator transition (MIT) in the LSMO [307, 308]. Impedance spectroscopy is a promising way to characterise this transition since it can dissect the resistance and capacitance contributions from different layers of the device stack. Observing a change from metallic to semiconducting conductivity above a $T_{C,MIT}$, with a positive to negative temperature coefficients of resistivity (TCR) respectively, would therefore be indicative of an MIT in LSMO. A subsequent shift in $T_{C,MIT}$ between the HRS and LRS would suggest a LSMO MIT to influence the SOT switching.

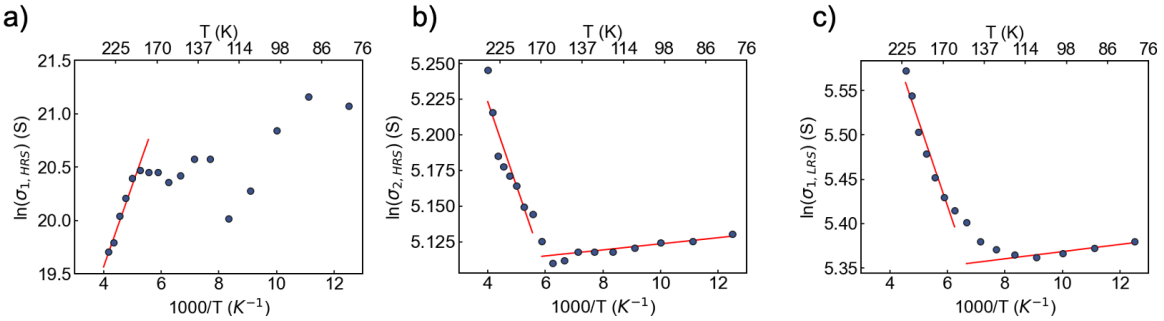

Figure 6.8: Temperature dependence of the conductivity of a) the YHO layer σ_1 in the HRS with an activation energy of 66 meV b) the YHO|LSMO interfacial layer in the HRS σ_2 with an activation energy of -4.1 meV above 140K c) σ_2 in the LRS with an activation energy of -8.2 meV above 140K.

Figure 6.8 shows the extracted conductivity from the equivalent circuit analysis for the HRS YHO feature a), the HRS interface feature b), and the LRS c) against temperature. The low-temperature region of the YHO feature in the high resistance state was challenging to fit, since the relaxation time was outside of the measurement range, thus giving noisy results. An extended analysis of the temperature-dependent permittivity changes in the YHO using the domain wall pinning element Z_{DWP} is elaborated in the appendix, see Fig. B.1.

The observed conductivity changes between 80 and 250 K are very small, within 10%. The conductivity values in the high temperature range were fitted using an Arrhenius law. The YHO conductivity, $\sigma_{1,HRS}$ in the HRS shows a negative TCR with a small activation energy of 66 meV. Conversely, the interface relaxation in the HRS $\sigma_{2,HRS}$ and the LRS $\sigma_{1,LRS}$ have very similar magnitudes and a positive TCR with a similar activation energy of -4.1 meV and -8.2 meV, indicative of metallic conductivity. Furthermore, a transition region is observed around 140 K, indicated by a change in the slope of the conductivity against temperature. Interestingly, this occurs at a similar temperature for all of the investigated conductivities.

A first consideration would be to ascribe the transition region to the $T_{C,MIT}$ of the resistive phase transition within the LSMO. The transition temperature falls within the range of a highly resistive LSMO. However, the LSMO changes from metallic to semiconducting, i.e. from a positive to a negative TCR, whereas the opposite is observed for the high-frequency $\sigma_{2,HRS}$ and $\sigma_{1,LRS}$, which both describe the LSMO|YHO interface region. In addition, the change in conductivity is expected to be significantly larger for LSMO[309]. We can therefore conclude that the $T_{C,MIT}$ of the LSMO is above the measurement range of 250 K. Another possibility would be that the transition region coincides with the antiferro-distortive phase transition (T_{AFD}) of NbSTO. At 0.5 wt% Nb doping, the T_{AFD} has been measured to occur

around 120K [310]. The NbSTO acts as a degenerate semiconductor, where the Fermi level is above the conduction band edge and therefore displays metallic conductivity. The resistivity ρ of NbSTO varies according to the $\rho \propto AT^2$, where at T_{AFD} the scaling parameter A changes in magnitude. The transition temperature is not expected to change with a change in the resistance state in the device. However, the NbSTO remains metallic and can therefore not account for the behaviour observed in the YHO feature $\sigma_{1,HRS}$. The expected transitions within the NbSTO and LSMO cannot account for the observed behaviour and thus source of the transition may be the YHO layer.

One should also the small magnitude of the activation energies, which fall in the range for hopping conduction and is a commonly attributed transport mechanism for filamentary HfO_2 [311–315] but also ferroelectric HZO and La-doped HfO_2 thin films [316]. Hopping conduction involves the thermally activated transport of electrons near the Fermi edge, jumping from a state below the Fermi level to just above. The activation energy is the difference in energy between both states [37]. This is to be distinguished from Poole-Frenkel behaviour whereby an electron is emitted from a trap state into the conduction band via thermionic emission.

Transitions in slope with similar magnitudes of activation energies have indeed observed in TiO_2 [317] and HfO_2 filamentary RS devices [318]. Wang et al identified the transition temperature to be close to $\frac{\theta_D}{2}$ [318], where θ_D is the Debye temperature, determined to be $\theta_D \approx$220K for HfO_2 [319]. At $\frac{\theta_D}{2}$ a transition between polaronic hopping regimes had been predicted by Schnakenberg, below which certain phonon modes are frozen and no longer contribute to conduction [320, 321]. Polaronic hopping is particularly prevalent as a type of impurity conduction. A polaron is formed when trapped electrons couple strongly to phonon modes and cause a distortion in the local lattice environment. Transport subsequently would occur through phonon-assisted tunnelling between trapping sites, where the activation energy is related to the absorption and release of a phonon. [37]. Polaronic hopping can be described by a thermally activated Arrhenius process, shown in equation 6.1, where σ is the conductivity, σ_0 the pre-exponential factor, T is the temperature, E_a the activation energy and k_b the Boltzmann constant.

$$\sigma = \sigma_0 T^{-1} \exp\left(-\frac{E_a}{k_b T}\right) \tag{6.1}$$

Large electron-phonon coupling has been predicted for the formation of polarons in singly charged oxygen vacancies in oxygen-deficient HfO_2 [322, 323] and therefore the change in slope observed here may be a plausible indication of polaronic hopping occurring within the YHO layer. Different hopping regimes are often separated by their T^n dependencies.

However, polaronic hopping (n = -1), variable range hopping (n = -1/4 or n = -1/3) and nearest neighbour hopping (n = -1) could not be differentiated.

6.7 Proposed Mechanism

In this section, we will propose an elementary model of the SOT, which is consistent with the electrical, chemical and structural information obtained within this thesis. The resistance change during the SOT is predominantly due to a reorganisation of oxygen species, which is schematically illustrated in Fig. 6.9.

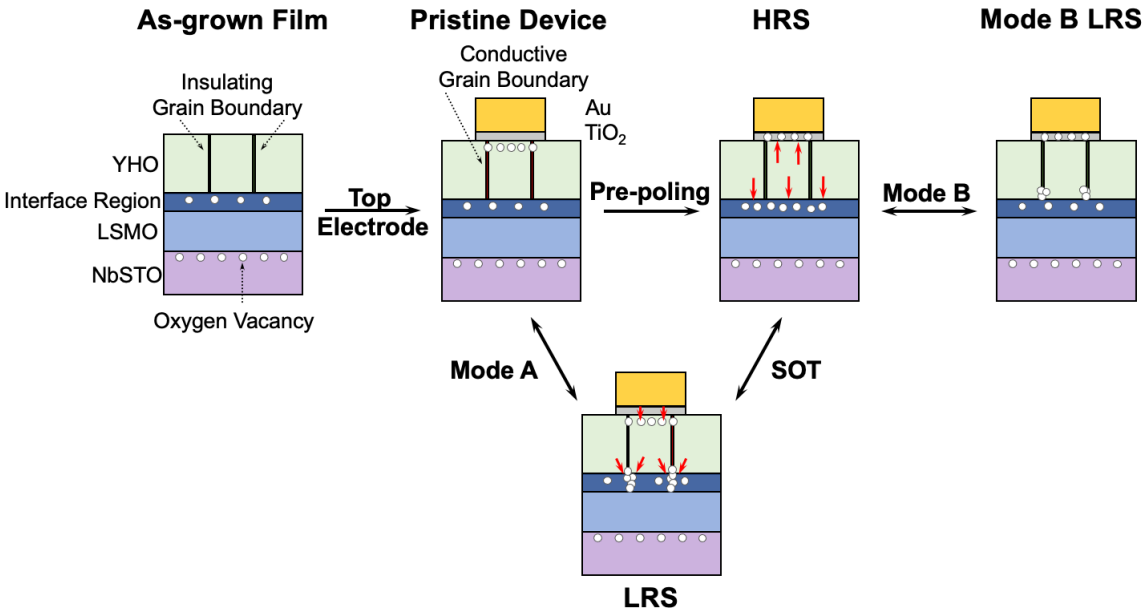

Figure 6.9: Proposed Mechanism displaying oxygen exchange across multiple device layers, which enable the SOT, mode A and mode B.

We begin with the film deposition process. During high temperature vacuum annealing of the NbSTO substrate, the atomic step edges on the surface are flattened and a substoichiometric surface is created. The LSMO, which is deposited subsequently, becomes slightly more resistive due to electron donation from the NbSTO and depletion of hole carriers at the interface. Upon deposition of the YHO, either the PLD plasma or the oxygen affinity difference between YHO and LSMO create a oxygen vacancy rich top surface within the LSMO. The epitaxial device stack is cooled slowly and under high oxygen pressure to ameliorate oxygen deficiency. The YHO is strained into a rhombohedral distortion, exhibiting a high density of grain-boundaries and ferroelectric properties. The growth of the top electrode is associated with oxygen scavenging from the top surface of the YHO, establishing a oxygen concentra-

tion gradient across the Ti adhesion layer. Sputtering damage or a high oxygen affinity are the main drivers behind this. The scavenging seems to mainly affect crystallographically incoherent regions within the YHO, perhaps between separate crystallographic phases/orientations, dislocations or grain boundaries . These are rendered electronically conductive, shorting the YHO grain conduction and only leaving the LSMO|YHO interface region to limit current conduction. Hence, the pristine state exhibits an intermediate resistance state. Device stacks with thick LSMO buffer electrodes do not exhibit these conductive pristine states. Slight thickness dependent differences in symmetry from a rhombohedral to a monoclinic distortion within the LSMO may influence the symmetry of the film above. In YHO a difference in rhombohedral distortion or the relative abundance of non-ferroelectric monoclinic phases may alter the density of defective and chemically under-coordinated regions, which may serve as nucleation points for filament formation. Critically, both a thickness confined and hole depleted LSMO are required to stabilise such a conductive pristine state.

The application of a positive voltage sweep RESETs the device into the HRS. Positive bias causes oxygen anions to migrate from the bottom LSMO electrode into the YHO, reducing the LSMO and increasing its resistance. In addition, the high currents present during the RESET operation cause significant Joule heating. Oxygen from the interlayer may diffuse into the YHO to alleviate concentration differences. The oxygen may accumulate near the conductive channels, rapidly increasing their resistance. Conversely, the SET process is achieved by application of a negative bias. Oxygen anions depart the YHO and are absorbed by the top and bottom interface through field enhanced drift and Soret thermodiffusion. Conductive filaments are nucleated along the under-coordinated regions and break through the LSMO|YHO interface region. A high defect concentration near the top surface of the YHO also facilitates electron transport, leaving the device stack in a highly conductive LRS. Ferroelectric polarisation reversal may contribute to the SET process.

A number of closely related switching modes of the same switching polarity were observed within different devices of the same thin film stack. Mode A switching exhibited a HRS similar to the pristine state and the same LRS as the SOT. However, this mode did not fully RESET into the SOT HRS. The conductive channels within the YHO remained and the resistance change was confined to the LSMO|YHO interface region. Mode B on the other hand, was significantly more resistive. The HRS was of similar magnitude as the SOT, but this mode did not exhibit a conductive pristine state. Mode B still was of filamentary nature, however not breaking through the LSMO|YHO interface region. This was the dominant switching mode observed in devices with 50 uc LSMO and those with undoped STO substrate, indicating the crucial role of sufficiently tuned LSMO in stabilising the SOT. The lack of a conductive pristine state may originate from fewer under-coordinated regions,

such as incoherent grain boundaries present underneath the electrodes or due to locally diminished Ti oxygen scavenging. During cycling of all three modes, a degradation effect was observed in the LSMO|YHO interface region, which manifested itself as an increase in resistance over time. Repeated high voltage stress may cause an agglomeration of oxygen vacancies over time at the LSMO top interface. Such an oxygen depletion would increase the LSMO resistance over time. A similar effect has been observed in similar device stacks and was termed a *training-effect*[245] or a low RS endurance [216].

6.8 Conclusion

To conclude, a comprehensive microscopic understanding of the RS processes occurring during SOT switching was developed using impedance spectroscopy. Relaxations originating from the YHO grains and LSMO|YHO interface region were detected and separated. In the conductive pristine state, the LSMO|YHO interface region was indicated to be the current limiting element. The YHO grain resistance was bypassed by localised conduction paths induced by the top electrode fabrication. The enhancement of a strain induced oxygen vacancy concentration at the LSMO|YHO interface and thickness related symmetry changes within the LSMO were hypothesised to be the root cause behind stabilising the SOT only at low LSMO thicknesses. The complex switching processes and stages were disentangled by observing impedance spectra in intermediate resistance states of different switching modes. A related RS mode was detected, where solely the interface region undergoes filamentary switching, akin to a virtual cathode model [287]. Furthermore, degradation of the LSMO|YHO interface over multiple switching cycles could successfully be tracked using impedance spectroscopy. Next, a potential MIT within the LSMO does not seem to play a significant role in determining the resistance state within the SOT. Finally, the temperature dependent transport investigations suggested that current flows through the device are governed through a polaronic hopping regime.

Chapter 7

Conclusions and Outlook

In this thesis the resistance switching of ultrathin epitaxial ferroelectric HfO_2 based devices is explored for its application in future non-volatile memory and neuromorphic computing applications. A device stack was engineered to obtain both high ferroelectric polarisation and high oxygen mobility to probe for coupled resistance switching phenomena. The HfO_2 film (4.5 nm) was doped with Y (YHO), to generate a controlled oxygen vacancy concentration, and grown epitaxially for high ferroelectric polarisation. The bottom buffer electrode employed a LSMO (11nm) on NbSTO stack to allow for a tuneable carrier concentration with electrode thickness.

X-Ray diffraction, piezoresponse force microscopy and capacitance voltage measurments demonstrated the ferroelectric properties of the YHO. Upon contacting the stack with Ti|Au top electrodes, a resistance switching mode was found with a high on/off ratio which changed the conduction properties from Schottky emission limiting to ohmic transport, a Schottky-to-ohmic transition (SOT). The application of voltage pulses stabilised intermediate resistance states and given a suitable pulse scheme, an accumulation function, integrate-and-fire, was demonstrated.

Several features of the SOT switching mode hinted towards a complex interplay of interactions. First, the device in the pristine state was in an intermediate resistance state between the HRS and the LRS. An inspection of the area dependence of the current indicated that the conduction in the LRS occurs through a conductive filament. This area independence of conduction current was already present in the pristine state, indicating the role of the stack engineering to form conductive channels. Hence, the device did not require a forming process. Capacitance-voltage measurements revealed that the SET process did correlate with ferroelectric polarisation reversal, whereas the RESET operation did not. This indicated a predominantly ionic mechanism to govern the switching mode. The FE polarisation reversal may aid in the SET process through additional displacement current, heat, piezoelectric or

interfacial termination effects.
Changes to the interface chemistry revealed that the Ti adhesion layer of the Au electrode is indeed not inert and a carefully tuned interface oxygen leaching at the top electrode is required to stabilise the SOT, possibly making under-coordinated regions in YHO, such as incoherent grain boundaries, conductive. Furthermore, the crucial role of the bottom interface was established, that thickness confined LSMO is essential for the switching mode, through enhanced oxygen exchange or symmetry transfer. Chemical analysis indicated that oxygen moves out of the YHO film into the Ti interlayer and the LSMO during the SET operation and subsequently returns during the RESET operation, indicating a predominantly ionic origin to the SOT.
It was demonstrated that impedance spectroscopy is an effective and powerful method to investigate microscopic resistance changes in complex heterostructures. A number of poling schemes and film modifications were employed to disentangle the RS contributions from the LSMO|YHO interface region and the YHO film. Both the interface and the film region switched simultaneously during the SET process, whereas the RESET process occurred separately, indicating separate mechanisms, which was proposed to occur through first field enhanced drift and subsequently thermally stimulated motion of ionic species. However, a possible metal-insulator transition in the LSMO does not seem to play a significant role.

In the study of ionic and ferroelectric resistance switching systems, it is important to recognize that the conditions favourable for each can often be contradictory. Interfacial strain in oxide electrode, presents an intriguing method to enhance oxygen transport across material interfacial barriers and enhance resistance switching performance. However, it presents a double-edged sword due to its tendency to accelerate the degradation of the ferroelectric and the electrode material. Strain can also contribute to the formation of a high density of grain boundaries, where oxygen scavenging by top electrode materials may alter the conductivity of the grain boundaries. This process could eliminate the need for the electro-forming step typically required in filamentary resistive switching devices, a step associated with high variability. However, this same approach is detrimental for ferroelectrics. Finally, this thesis clearly demonstrates that impedance spectroscopy is a powerful analytical tool to disentangle convoluted resistance switching phenomena. Yet, it remains underutilized in this field. Specifically in multi-layer stacks, the voltage dependent changes in different layers can be identified and degradation processes monitored, providing valuable insights into device stack behaviour.

A number of intriguing phenomena were observed in this thesis, which may be of interest for further study using simplified device stacks. Some potential avenues are suggested:

The thickness of the LSMO clearly had a significant electronic impact on the HfO_2 based devices and a structural change within the YHO was indicated. A structural correlation between the degree of the rhombohedral distortion within the LSMO and YHO could be studied using a wide thickness range, high resolution XRD and STEM measurements. This could shed light on the impact of the rhombohedral distortion on the ferroelectric properties of HfO_2.

The LSMO|YHO interface seems to exist in an unstable state as-grown, leading to a *training* effect of decreasing device leakage over a number of switching cycles, observed here and elsewhere [216, 245]. This may be related to an oxygen-dependent alignment of LSMO Fermi level to the charge neutrality level in the YHO [324]. Fatigue studies correlating HAXPES based valence band offsets, CV profiling and impedance spectroscopy may be helpful to reveal the underlying dynamics.

The nature of the conductive pristine state warrants further research. Conductive grain boundaries in stoichiometric and oxygen deficient monoclinic HfO_2 have recently been observed [249]. Considering the potential conductivity of stoichiometric inter-phase boundaries and their chemical and electronic structure using conductive AFM and EELS with high spatial resolution, may yield opportunities to tune filamentary RS memories.

An investigation into the temperature dependence of the permittivity in ferroelectric HfO_2 near the Curie temperature using the domain-wall pinning element may yield fruitful insights into domain dynamics stabilising the ferroelectric phase.

Chapter 8

Glossary

AC	alternating current
ANN	artificial neural network
C	capacitance
cAFM	conductive atomic force microscopy
CPE	constant phase element
DC	direct current
DT	Direct tunneling
EELS	electron energy loss spectroscopy
ELNES	electron energy-loss near edge fine structure
FNT	Fowler-Nordheim tunnelling
FSD	ferroelectric schottky diode
FWHM	full width half maximum
GPU	graphics processing units
HAADF	high angle annular dark field
HAXPES	hard X-ray photoelectron spectroscopy
HRS	high resistance state
HZO	$HfZrO_4$
IPA	isopropyl alcohol
IS	impedance spectroscopy
ITO	Sn doped In_2O_3
LRS	low resistance state
LSCO	$LaSrCoO_3$
LSMO	$La_{1-x}Sr_xMnO3$
LTP-LTD	long-term potentiation long-term depression
MAC	multiply and accumulate

MIT metal insulator transition
ML machine learning
NbSTO Nb doped $SrTiO_3$
PFM piezo-response force microscopy
PLD pulsed laser deposition
PPF-PPD paired pulse facilitation paired pulse depression
PTO $PbTiO_3$
PXRD powder X-ray diffraction
R resistance
RAM random access memory
RHEED reflection high energy electron diffraction
RS resistive switching
SCLC space-charge limited conduction
SOT Schottky-to-Ohmic transition
SPM scanning probe microscopy
STEM scanning transmission electron microscopy
STO $SrTiO_3$
TAT trap assisted tunnelling
TCM thermo-chemical mechanism
TCR temperature coefficients of resistivity
TI thermionic injection
VCM valence change mechanism
WKB Wentzel-Kramers-Brillouin
XPS X-ray photo electron spectroscopy
XRR X-ray reflectivity
YHO Y doped HfO_2
YSZ Yttria stabilised Zirconia
ZLP zero loss peak

Bibliography

1. Von Neumann, J. & Kurzweil, R. *The Computer and the Brain* (Yale university press, 1958).
2. Moore, G. E. Cramming more components onto integrated circuits. *Electronics* **38** (1965).
3. Dennard, R. *et al.* Design of Ion-Implanted Small MOSFET ' S Dimensions with Very Small Dimensions. *IEEE Journal of Solid State Circuits* **9,** 257–268 (1974).
4. Mehonic, A. & Kenyon, A. J. Brain-inspired computing needs a master plan. *Nature* **604,** 255–260 (2022).
5. Dally, B. *Hardware for Deep Learning* in *Hot Chips 2023* (2023).
6. Amodeim, D. & Hernandez, D. *AI and Compute* 2018.
7. Vaswani, A. *et al.* Attention is All You Need. *Advances in Neural Information Processing Systems* **30** (2017).
8. Alabdulmohsin, I., Neyshabur, B. & Zhai, X. Revisiting Neural Scaling Laws in Language and Vision. *Advances in Neural Information Processing Systems* **35,** 1–13 (2022).
9. Conklin, A. A. & Kumar, S. Solving the big computing problems in the twenty-first century. *Nature Electronics* **6,** 464–466 (2023).
10. Jones, N. *et al.* The information factories. *Nature* **561,** 163–6 (2018).
11. Landauer, R. Irreversibility and heat generation in the computing process. *IBM Journal of Research and Development* **5,** 183–191 (1961).
12. Von Neumann, J. *First draft report on EDVAC* 1945.
13. Horowitz, M. 1.1 Computing's energy problem (and what we can do about it). *Digest of Technical Papers - IEEE International Solid-State Circuits Conference* **57,** 10–14 (2014).
14. Schenk, T., Pesic, M., Slesazeck, S., Schroeder, U. & Mikolajick, T. Memory technology — a primer for material. *Rep. Prog. Phys.* **83,** 086501 (2020).
15. Das, S., Chen, A. & Marinella, M. Beyond CMOS. *Proceedings - 2021 IEEE International Roadmap for Devices and Systems Outbriefs, IRDS 2021* (2021).
16. Shastri, B. J. *et al.* Photonics for artificial intelligence and neuromorphic computing. *Nature Photonics* **15,** 102–114 (2021).
17. Hylton, T. Thermodynamic Computing: An Intellectual and Technological Frontier. *Proceedings* **47,** 23 (2020).

18. Sebastian, A., Le Gallo, M., Khaddam-Aljameh, R. & Eleftheriou, E. Memory devices and applications for in-memory computing. *Nature Nanotechnology* **15,** 529–544 (2020).
19. Wang, Z. *et al.* Resistive switching materials for information processing. *Nature Reviews Materials* **5,** 173–195 (2020).
20. Block, H.-D. The perceptron: A model for brain functioning. i. *Reviews of Modern Physics* **34,** 123 (1962).
21. Kumar, S., Wang, X., Strachan, J. P., Yang, Y. & Lu, W. D. Dynamical memristors for higher-complexity neuromorphic computing. *Nature Reviews Materials* **7,** 575–591 (2022).
22. Kendall, J. D. & Kumar, S. The building blocks of a brain-inspired computer. *Applied Physics Reviews* **7** (2020).
23. Waser, R., Böttger, U. & (Ed.), S. T. *Polar Oxides* 1st Editio (Wiley, New York, 2005).
24. Scott, J. F. Ferroelectrics go bananas. *Journal of Physics Condensed Matter* **20** (2008).
25. Damjanovic, D. Ferroelectric, dielectric and piezoelectric properties of ferroelectric thin films and ceramics. *Reports on Progress in Physics* **61,** 1267–1324 (1998).
26. Scott, J. F. *Ferroelectric Memories. Springer Series in Advanced Microelectronics, Vol. 3* 248 (2000).
27. Chanthbouala, A. *et al.* Giant Tunnel Electroresistance in Ferroelectric Tunnel Junctions. *Frontiers in Electronic Materials* **94,** 50–50 (2013).
28. Pantel, D. & Alexe, M. Electroresistance effects in ferroelectric tunnel barriers. *Physical Review B - Condensed Matter and Materials Physics* **82,** 1–8 (2010).
29. Hong, S., Nakhmanson, S. M. & Fong, D. D. Screening mechanisms at polar oxide heterointerfaces. *Reports on Progress in Physics* **79** (2016).
30. MOTT, N. F. The theory of crystal rectifiers. **1,** 153–165 (1939).
31. Tung, R. T. The physics and chemistry of the Schottky barrier height. *Applied Physics Reviews* **1,** 11304 (2014).
32. Robertson, J. Band offsets of wide-band-gap oxides and implications for future electronic devices. *Journal of Vacuum Science & Technology B: Microelectronics and Nanometer Structures Processing, Measurement, and Phenomena* **18,** 1785–1791 (2000).
33. Bardeen, J. Surface states and rectification at a metal semi-conductor contact. *Physical Review* **71,** 717–727 (May 1947).
34. Mönch, W. Role of virtual gap states and defects in metal-semiconductor contacts. *Physical Review Letters* **58,** 1260–1263 (1987).
35. Cowley, A. M. & Sze, S. M. Surface states and barrier height of metal-semiconductor systems. *Journal of Applied Physics* **36,** 3212–3220 (1965).
36. Rhoderick, E. H. Metal-Semiconductor Contacts. *IEE Proceedings I: Solid State and Electron Devices* **129,** 1–14 (1982).
37. Mott, N. F. & Davis, E. A. *Electronic Processes in Non-Crystalline Materials* (1971).
38. Tuller, H. in *Springer Handbooks* 1 (Springer, 2017).

39. Kröger, F. A. & Vink, H. J. Relations between the Concentrations of Imperfections in Crystalline Solids. *Solid State Physics - Advances in Research and Applications* **3,** 307–435 (Jan. 1956).
40. Li, H., Guo, Y. & Robertson, J. Dopant compensation in HfO2 and other high K oxides. *Applied Physics Letters* **104** (2014).
41. SHOCKLEY, W. & READ, W. T. Statistics of the Recombinations of Holes and Electrons. *Physical Review* **87,** 835–842 (1952).
42. Bagdzevicius, S., Maas, K., Boudard, M. & Burriel, M. Interface-type resistive switching in perovskite materials. *Journal of Electroceramics* **39,** 157–184 (2017).
43. Mehrer, H. *Diffusion in solids: fundamentals, methods, materials, diffusion-controlled processes* (Springer Science & Business Media, 2007).
44. Ielmini, D. & Waser, R. *Resistive switching: from fundamentals of nanoionic redox processes to memristive device applications* (John Wiley \& Sons, 2015).
45. Fröhlich, H. Electronic Processes in Ionic Crystals. *Nature 1949-sep vol. 164 iss. 4166* **164** (Sept. 1949).
46. Genreith-Schriever, A. R. & De Souza, R. A. Field-enhanced ion transport in solids: Reexamination with molecular dynamics simulations. *Physical Review B* **94,** 224304 (Dec. 2016).
47. Strukov, D. B. & Williams, R. S. Exponential ionic drift: Fast switching and low volatility of thin-film memristors. *Applied Physics A: Materials Science and Processing* **94,** 515–519 (Mar. 2009).
48. Lee, J. S., Lee, S. & Noh, T. W. *Resistive switching phenomena: A review of statistical physics approaches* Sept. 2015.
49. Strukov, D. B., Alibart, F. & Stanley Williams, R. Thermophoresis/diffusion as a plausible mechanism for unipolar resistive switching in metal-oxide-metal memristors. *Applied Physics A: Materials Science and Processing* **107,** 509–518 (June 2012).
50. Chua, L. Memristor - The missing Circuit Element. *IEEE Transactions on Circuit Theory* **C,** 507–519 (1971).
51. Lin, D., Chua, L. & Hui, S. Y. The first man-made memristor: Circa 1801. *Proceedings of the IEEE* **103,** 131–136 (2015).
52. Strukov, D. B., Snider, G. S., Stewart, D. R. & Williams, R. S. The missing memristor found. *Nature* **453,** 80–83 (2008).
53. Chua, L. If it's pinched it's a memristor. *Semiconductor Science and Technology* **29** (2014).
54. Waser, R. & Aono, M. in *Nanoscience and Technology: A Collection of Reviews from Nature Journals* 158–165 (World Scientific, 2009).
55. Chanthbouala, A. *et al.* A ferroelectric memristor. *Nature Materials* **11,** 860–864 (2012).
56. Keshavarzi, A., Ni, K., Van Den Hoek, W., Datta, S. & Raychowdhury, A. FerroElectronics for Edge Intelligence. *IEEE Micro* **40,** 33–48 (2020).
57. Blom, P. W., Wolf, R. M., Cillessen, J. F. & Krijn, M. P. Ferroelectric Schottky diode. *Physical Review Letters* **73,** 2107–2110 (1994).

58. Liu, X., Wang, Y., Burton, J. D. & Tsymbal, E. Y. Polarization-controlled Ohmic to Schottky transition at a metal/ferroelectric interface. *Physical Review B - Condensed Matter and Materials Physics* **88,** 1–6 (2013).
59. Choi, T., Lee, S., Choi, Y., Kiryukhin, V. & Cheong, S.-W. Switchable ferroelectric diode and photovoltaic effect in BiFeO3. *Science* **324,** 63–66 (2009).
60. Jiang, A. Q. *et al.* A resistive memory in semiconducting BiFeO3 thin-film capacitors. *Advanced Materials* **23,** 1277–1281 (2011).
61. Wang, C. *et al.* Switchable diode effect and ferroelectric resistive switching in epitaxial BiFeO3 thin films. *Applied Physics Letters* **98** (2011).
62. Luo, Q. *et al.* A highly CMOS compatible hafnia-based ferroelectric diode. *Nature Communications* **11,** 1391 (2020).
63. Fan, Z. *et al.* Ferroelectric Diodes with Charge Injection and Trapping. *Physical Review Applied* **7,** 1–11 (2017).
64. Kohlstedt, H., Pertsev, N. A., Rodríguez Contreras, J. & Waser, R. Theoretical current-voltage characteristics of ferroelectric tunnel junctions. *Physical Review B - Condensed Matter and Materials Physics* **72,** 1–10 (2005).
65. Tsymbal, E. Y. & Kohlstedt, H. Tunneling across a ferroelectric. *Science* **313,** 181–183 (2006).
66. Kwon, D. H. *et al.* Atomic structure of conducting nanofilaments in TiO_2 resistive switching memory. *Nature Nanotechnology* **5,** 148–153 (2010).
67. O'Dwyer, J. J. Theory of Dielectric Breakdown in Solids. *Journal of The Electrochemical Society* **116,** 239 (1969).
68. Strukov, D. B., Alibart, F. & Stanley Williams, R. Thermophoresis/diffusion as a plausible mechanism for unipolar resistive switching in metal-oxide-metal memristors. *Applied Physics A: Materials Science and Processing* **107,** 509–518 (2012).
69. Kinoshita, K. *et al.* Reduction in the reset current in a resistive random access memory consisting of Ni Ox brought about by reducing a parasitic capacitance. *Applied Physics Letters* **93,** 33506 (2008).
70. Waser, R., Dittmann, R., Staikov, C. & Szot, K. Redox-based resistive switching memories nanoionic mechanisms, prospects, and challenges. *Advanced Materials* **21,** 2632–2663 (2009).
71. Sharath, S. U. *et al.* Control of Switching Modes and Conductance Quantization in Oxygen Engineered HfO_x based Memristive Devices. *Advanced Functional Materials* **27,** 1–13 (2017).
72. Yang, J. J., Inoue, I. H., Mikolajick, T. & Hwang, C. S. Metal oxide memories based on thermochemical and valence change mechanisms. *MRS Bulletin* **37,** 131–137 (2012).
73. Sawa, A. Resistive switching in transition metal oxides. *Materials Today* **11,** 28–36 (June 2008).
74. Sawa, A., Fujii, T., Kawasaki, M. & Tokura, Y. *Interface transport properties and resistance switching in perovskite-oxide heterojunctions* in *Strongly Correlated Electron Materials: Physics and Nanoengineering* **5932** (SPIE, Aug. 2005), 59322C.

75. Baeumer, C. *et al.* Quantifying redox-induced Schottky barrier variations in memristive devices via in operando spectromicroscopy with graphene electrodes. *Nature Communications* **7,** 1–7 (2016).
76. Dawber, M., Scott, J. F. & Hartmann, A. J. Effects of donor and acceptor dopants on schottky barrier heights and vacancy concentrations in barium strontium titanate. *Journal of the European Ceramic Society* **21,** 1633–1636 (2001).
77. Dawber, M., Rabe, K. M. & Scott, J. F. Physics of thin-film ferroelectric oxides. *Reviews of Modern Physics* **77,** 1083–1130 (2005).
78. Schafranek, R., Payan, S., Maglione, M. & Klein, A. Barrier height at (Ba,Sr)TiO_3 /Pt interfaces studied by photoemission. *Physical Review B - Condensed Matter and Materials Physics* **77,** 30–33 (2008).
79. Baumgarten, L. *et al.* Smart Design of Fermi Level Pinning in HfO_2-Based Ferroelectric Memories. *Advanced Functional Materials* **34,** 1–16 (2024).
80. Dittmann, R. *et al.* Engineering the kinetics of redox-based memristive devices for neuromorphic computing. *Technical Digest - International Electron Devices Meeting, IEDM* (2023).
81. Guo, Y. & Robertson, J. Materials selection for oxide-based resistive random access memories. *Applied Physics Letters* **105,** 1–6 (2014).
82. Schroeder, H., Zhirnov, V. V., Cavin, R. K. & Waser, R. Voltage-time dilemma of pure electronic mechanisms in resistive switching memory cells. *Journal of Applied Physics* **107,** 054517 (Mar. 2010).
83. Jiang, J. & Hertz, J. L. On the variability of reported ionic conductivity in nanoscale YSZ thin films. *Journal of Electroceramics* **32,** 37–46 (2014).
84. Harrington, G. F. *et al.* The interplay and impact of strain and defect association on the conductivity of rare-earth substituted ceria. *Acta Materialia* **166,** 447–458 (2019).
85. Kushima, A. & Yildiz, B. Oxygen ion diffusivity in strained yttria stabilized zirconia: Where is the fastest strain? *Journal of Materials Chemistry* **20,** 4809–4819 (2010).
86. Kharton, V. V., Naumovich, E. N. & Vecher, A. A. Research on the electrochemistry of oxygen ion conductors in the former Soviet Union. I. ZrO_2-based ceramic materials. *Journal of Solid State Electrochemistry* **3,** 61–81 (1999).
87. Szyjka, T. *et al.* From Doping to Dilution: Local Chemistry and Collective Interactions of La in HfO2. *Physica Status Solidi - Rapid Research Letters* **16** (2022).
88. Koettgen, J. *et al.* Understanding the ionic conductivity maximum in doped ceria: Trapping and blocking. *Physical Chemistry Chemical Physics* **20,** 14291–14321 (2018).
89. Clausen, K. N. & Hayes, W. Defect structure of yttria-stabilized zirconia and its influence on the ionic conductivity at elevated temperatures. *Physical Review B - Condensed Matter and Materials Physics* **59,** 14202–14219 (1999).
90. Knöner, G., Reimann, K., Röwer, R., Södervall, U. & Schaefer, H. E. Enhanced oxygen diffusivity in interfaces of nanocrystalline $ZrO_2{\cdot}Y_2O_3$. *Proceedings of the National Academy of Sciences of the United States of America* **100,** 3870–3873 (2003).
91. Szot, K., Speier, W., Bihlmayer, G. & Waser, R. Switching the electrical resistance of individual dislocations in single-crystalline SrTiO3. *Nature Materials* **5,** 312–320 (2006).

92. Lanza, M. *et al.* Grain boundaries as preferential sites for resistive switching in the HfO_2 resistive random access memory structures. *Applied Physics Letters* **100,** 123508 (2012).

93. Feng, B., Ishikawa, R., Kumamoto, A., Shibata, N. & Ikuhara, Y. Atomic Scale Origin of Enhanced Ionic Conductivity at Crystal Defects. *Nano Letters* **19,** 2162–2168 (2019).

94. Cho, S. *et al.* Self-assembled oxide films with tailored nanoscale ionic and electronic channels for controlled resistive switching. *Nature Communications* **7,** 12373 (Aug. 2016).

95. MacManus-Driscoll, J. L. *et al.* New approaches for achieving more perfect transition metal oxide thin films. *APL Materials* **8,** 40904 (2020).

96. Yang, S. M. *et al.* Strongly enhanced oxygen ion transport through samarium-doped CeO_2 nanopillars in nanocomposite films. *Nature Communications* **6,** 8588 (2015).

97. Petzold, S. *et al.* Forming-Free Grain Boundary Engineered Hafnium Oxide Resistive Random Access Memory Devices. *Advanced Electronic Materials* **5,** 1900484 (Oct. 2019).

98. Kenyon, A. J. *et al.* The interplay between structure and function in redox-based resistance switching. *Faraday Discussions* **213,** 151–163 (2019).

99. Kunwar, S. *et al.* Protons: Critical Species for Resistive Switching in Interface-Type Memristors. *Advanced Electronic Materials* **9** (2023).

100. Heisig, T. *et al.* Oxygen Exchange Processes between Oxide Memristive Devices and Water Molecules. *Advanced Materials* **30** (2018).

101. Cooper, D. *et al.* Anomalous Resistance Hysteresis in Oxide ReRAM: Oxygen Evolution and Reincorporation Revealed by In Situ TEM. *Advanced Materials* **29,** 1–8 (2017).

102. Siegel, S. *et al.* Trade-Off Between Data Retention and Switching Speed in Resistive Switching ReRAM Devices. *Advanced Electronic Materials* **7** (2021).

103. Posadas, A. B. *et al.* Scavenging of oxygen from $SrTiO_3$ during oxide thin film deposition and the formation of interfacial 2DEGs. *Journal of Applied Physics* **121** (2017).

104. Kim, W. *et al.* Impact of oxygen exchange reaction at the ohmic interface in Ta_2O_5-based ReRAM devices. *Nanoscale* **8,** 17774–17781 (2016).

105. Zhu, J. *et al.* Probing vacancy behavior across complex oxide heterointerfaces. *Science Advances* **5** (2019).

106. Mikheev, E., Hoskins, B. D., Strukov, D. B. & Stemmer, S. Resistive switching and its suppression in Pt/Nb:$SrTiO_3$ junctions. *Nature Communications* **5** (2014).

107. Fan, Z. *et al.* Resistive switching induced by charge trapping/detrapping: A unified mechanism for colossal electroresistance in certain Nb:SrTiO3-based heterojunctions. *Journal of Materials Chemistry C* **5,** 7317–7327 (2017).

108. Herpers, A. *et al.* Spectroscopic proof of the correlation between redox-state and charge-carrier transport at the interface of resistively switching Ti/PCMO devices. *Advanced Materials* **26,** 2730–2735 (2014).

109. Choi, J. H., Mao, Y. & Chang, J. P. Development of hafnium based high-k materials - A review. *Materials Science and Engineering R: Reports* **72,** 97–136 (2011).

110. Lin, Y. S., Puthenkovilakam, R. & Chang, J. P. Dielectric property and thermal stability of HfO2 on silicon. *Applied Physics Letters* **81,** 2041–2043 (2002).

111. Robertson, J. High dielectric constant gate oxides for metal oxide Si transistors. *Reports on Progress in Physics* **69,** 327–396 (2006).

112. Böscke, T. S., Müller, J., Bräuhaus, D., Schröder, U. & Böttger, U. Ferroelectricity in hafnium oxide thin films. *Applied Physics Letters* **99** (2011).

113. Müller, J., Polakowski, P., Mueller, S. & Mikolajick, T. Ferroelectric Hafnium Oxide Based Materials and Devices: Assessment of Current Status and Future Prospects. *ECS Journal of Solid State Science and Technology* **4,** N30–N35 (2015).

114. Reiner, J. W. *et al.* Crystalline oxides on silicon. *Advanced Materials* **22,** 2919–2938 (2010).

115. Cremers, V., Puurunen, R. L. & Dendooven, J. Conformality in atomic layer deposition: Current status overview of analysis and modelling. *Applied Physics Reviews* **6** (2019).

116. Wurfel P & Batra I P. Depolarization-field-induced instability in thin ferroelectric film—experiment and theory. *Physical Review B* **8,** 5126–5133 (1973).

117. Tian, J. *et al.* Depolarization-Field-Induced Retention Loss in Ferroelectric Diodes. *Physical Review Applied* **11,** 1 (2019).

118. Lichtensteiger, Ć. *et al.* Monodomain to polydomain transition in ferroelectric $PbTiO_3$ thin films with $La_{0.67}Sr_{0.33}MnO_3$ electrodes. *Applied Physics Letters* **90,** 31–34 (2007).

119. Lee, H. J. *et al.* Scale-free ferroelectricity induced by flat phonon bands in HfO_2. *Science* **369,** 1343–1347 (2020).

120. Zhou, S., Zhang, J. & Rappe, A. M. Strain-induced antipolar phase in hafnia stabilizes robust thin-film ferroelectricity. *Science Advances* **8,** 6–11 (2022).

121. Glinchuk, M. D. *et al.* Possible electrochemical origin of ferroelectricity in HfO_2 thin films. *Journal of Alloys and Compounds* **830,** 1–13 (2020).

122. Kelley, K. P. *et al.* Ferroelectricity in hafnia controlled via surface electrochemical state. *Nature Materials* **22,** 1144–1151 (2023).

123. Kharton, V. V., Yaremchenko, A. A. & Naumovich, E. N. Research on the electrochemistry of oxygen ion conductors in the former Soviet Union. II. Perovskite-related oxides. *Journal of Solid State Electrochemistry* **3,** 303–326 (1999).

124. Christensen, D. V. *et al.* 2022 Roadmap on Neuromorphic Computing and Engineering. *Neuromorphic Computing and Engineering* **2,** 022501 (2022).

125. Johnson, B. & Jones, J. L. *Structures, phase equilibria, and properties of HfO_2* 25–45 (Elsevier Ltd., 2019).

126. Toriumi, A., Yamamoto, Y., Zhao, Y., Tomida, K. & Kita, K. Doped HfO_2 for Higher-k Dielectrics. *ECS Meeting Abstracts* **MA2005-02,** 508–508 (2006).

127. Li, F. M. *et al.* High-k (k= 30) amorphous hafnium oxide films from high rate room temperature deposition. *Applied Physics Letters* **98** (2011).

128. Meshcherskikh, A. N., Kolchugin, A. A., Antonov, B. D. & Dunyushkina, L. A. Phase Composition, Microstructure, and Electroconductivity of HfO_2–R_2O_3 Solid Electrolytes (R = Sc, Y, Ho, Er, Tm, Yb, and Lu). *Physics of the Solid State* **62,** 188–195 (2020).

129. Trubelja, M. F. & Stubican, V. S. Ionic Conductivity of the Fluorite-Type Hafnia–R_2O_3 Solid Solutions. *Journal of the American Ceramic Society* **74,** 2489–2494 (1991).

130. Schroeder, U., Park, M. H., Mikolajick, T. & Hwang, C. S. The fundamentals and applications of ferroelectric HfO_2. *Nature Reviews Materials* **7,** 653–669 (2022).

131. Hsain, H. A. *et al.* Many routes to ferroelectric HfO_2: A review of current deposition methods. *Journal of Vacuum Science & Technology A* **40** (2022).

132. Silva, J. P. *et al.* Roadmap on ferroelectric hafnia- and zirconia-based materials and devices. *APL Materials* **11** (2023).

133. Noheda, B., Nukala, P. & Acuautla, M. *Lessons from hafnium dioxide-based ferroelectrics* 2023.

134. Jan, A. *et al.* In Operando Optical Tracking of Oxygen Vacancy Migration and Phase Change in few Nanometers Ferroelectric HZO Memories. *Advanced Functional Materials* **33** (2023).

135. Yun, Y. *et al.* Intrinsic ferroelectricity in Y-doped HfO2 thin films. *Nature Materials* **21,** 903–909 (2022).

136. Shimizu, T. *et al.* Growth of epitaxial orthorhombic $YO_{1.5}$-substituted HfO_2 thin film. *Applied Physics Letters* **107** (2015).

137. Shimizu, T. *et al.* The demonstration of significant ferroelectricity in epitaxial Y-doped HfO2 film. *Scientific Reports* **6,** 1–8 (2016).

138. Shimizu, T. *et al.* Ferroelectricity mediated by ferroelastic domain switching in HfO_2-based epitaxial thin films. *Applied Physics Letters* **113** (2018).

139. Wei, Y. *et al.* A rhombohedral ferroelectric phase in epitaxially strained $Hf_{0.5}Zr_{0.5}O_2$ thin films. *Nature Materials* **17,** 1095–1100 (2018).

140. Lyu, J., Fina, I., Solanas, R., Fontcuberta, J. & Sánchez, F. Robust ferroelectricity in epitaxial $Hf_{0.5}Zr_{0.5}O_2$ thin films. *Applied Physics Letters* **113** (2018).

141. Estandía, S., Dix, N., Chisholm, M. F., Fina, I. & Sánchez, F. Domain-Matching Epitaxy of Ferroelectric $Hf_{0.5}Zr_{0.5}O_2(111)$ on $La_{2/3}Sr_{1/3}MnO_3(001)$. *Crystal Growth and Design* **20,** 3801–3806 (2020).

142. Nukala, P. *et al.* Guidelines for the stabilization of a polar rhombohedral phase in epitaxial $Hf_{0.5}Zr_{0.5}O_2$ thin films. *Ferroelectrics* **569,** 148–163 (2020).

143. Estandía, S. *et al.* Engineering Ferroelectric $Hf_{0.5}Zr_{0.5}O_2$ Thin Films by Epitaxial Stress. *ACS Applied Electronic Materials* **1,** 1449–1457 (2019).

144. Estandía, S. *et al.* Critical effect of the bottom electrode on the ferroelectricity of epitaxial $Hf_{0.5}Zr_{0.5}O_2$ thin films. *Journal of Materials Chemistry C* **9,** 3486–3492 (2021).

145. Shi, S. *et al.* Interface-engineered ferroelectricity of epitaxial $Hf_{0.5}Zr_{0.5}O_2$ thin films. *Nature Communications* **14** (2023).

146. Shen, Y. *et al.* Stabilization of ferroelectric $Hf_{0.5}Zr_{0.5}O_2$ epitaxial films via monolayer reconstruction driven by valence-dependent interfacial redox reaction and intralayer electron transfer. *Physical Review Materials* **7,** 1–8 (2023).

147. Lee, K. *et al.* Deterministic Orientation Control of Ferroelectric HfO_2 Thin Film Growth by a Topotactic Phase Transition of an Oxide Electrode. *ACS Nano* **18,** 12707–12715 (2024).

148. He, S. *et al.* $La_{0.6}Sr_{0.4}CoO_{3x}$ Films Under Deoxygenation: Magnetic And Electronic Transitions Are Apart from The Structural Phase Transition. *Advanced Functional Materials* **34,** 1–8 (2024).

149. Majumdar, S. & Dijken, S. V. Pulsed laser deposition of $La_{1-x}Sr_xMnO_3$: Thin-film properties and spintronic applications. *Journal of Physics D: Applied Physics* **47** (2014).

150. Tokura, Y. & Tomioka, Y. Colossal magnetoresistive manganites. *Journal of Magnetism and Magnetic Materials* **200,** 1–23 (1999).

151. Liao, Z. *et al.* Origin of the metal-insulator transition in ultrathin films of $La_{2/3}Sr_{1/3}MnO_3$. *Physical Review B - Condensed Matter and Materials Physics* **92,** 1–8 (2015).

152. Zhan, J. M. *et al.* Carrier tuning the metal-insulator transition of epitaxial $La_{2/3}Sr_{1/3}MnO_3$ thin film on Nb doped $SrTiO_3$ substrate. *AIP Advances* **6,** 0-6 (2016).

153. Rana, K. G., Parui, S. & Banerjee, T. Probing electron transport across a LSMO/Nb:STO heterointerface at the nanoscale. *Physical Review B - Condensed Matter and Materials Physics* **87,** 1–5 (2013).

154. Minohara, M., Yasuhara, R., Kumigashira, H. & Oshima, M. Termination layer dependence of Schottky barrier height for $La_{0.6}Sr_{0.4}MnO_3$ /Nb: SrTiO3 heterojunctions. *Physical Review B - Condensed Matter and Materials Physics* **81,** 1–6 (2010).

155. Minohara, M., Horiba, K., Kumigashira, H., Ikenaga, E. & Oshima, M. Depth profiling the potential in perovskite oxide heterojunctions using photoemission spectroscopy. *Physical Review B - Condensed Matter and Materials Physics* **85,** 1–6 (2012).

156. Liao, Z. & Zhang, J. Metal-to-insulator transition in ultrathin manganite heterostructures. *Applied Sciences (Switzerland)* **9,** 1–20 (2019).

157. Santiso, J. *et al.* Thickness evolution of the twin structure and shear strain in LSMO films. *CrystEngComm* **15,** 3908–3918 (2013).

158. Sandiumenge, F. *et al.* Competing misfit relaxation mechanisms in epitaxial correlated oxides. *Physical Review Letters* **110,** 1–5 (2013).

159. Hong, X., Posadas, A., Lin, A. & Ahn, H. Ferroelectric-field-induced tuning of magnetism in the colossal magnetoresistive oxide $La_{1-x}Sr_xMnO_3$. *Physical Review B - Condensed Matter and Materials Physics* **68,** 1–5 (2003).

160. Hong, X., Posadas, A. & Ahn, C. H. Examining the screening limit of field effect devices via the metal-insulator transition. *Applied Physics Letters* **86,** 1–3 (2005).

161. Ge, C. *et al.* Metal-Insulator Transition Induced by Oxygen Vacancies from Electrochemical Reaction in Ionic Liquid-Gated Manganite Films. *Advanced Materials Interfaces* **2,** 1–6 (2015).

162. Yao, L., Inkinen, S. & Van Dijken, S. Direct observation of oxygen vacancy-driven structural and resistive phase transitions in La2/3Sr1/3MnO3. *Nature Communications* **8,** 1–9 (2017).

163. Wei, Y. *et al.* Magneto-ionic control of spin polarization in multiferroic tunnel junctions. *npj Quantum Materials* **4,** 1–6 (2019).

164. Qin, Q. H. *et al.* Resistive Switching in All-Oxide Ferroelectric Tunnel Junctions with Ionic Interfaces. *Advanced Materials* **28,** 6852–6859 (2016).

165. Nukala, P. *et al.* Reversible oxygen migration and phase transitions in hafnia-based ferroelectric devices. *Science* **372,** 630–635 (2021).

166. Braun, W. *et al.* In situ thermal preparation of oxide surfaces. *APL Materials* **8** (2020).

167. Boyd, I. & Chrisey, D. B. *Pulsed laser deposition of thin films* (2004).

168. Ojeda-G-P, A., Döbeli, M. & Lippert, T. Influence of Plume Properties on Thin Film Composition in Pulsed Laser Deposition. *Advanced Materials Interfaces* **5,** 1–16 (2018).

169. Blank, D. H., Rijnders, G. J., Koster, G. & Rogalla, H. In-situ monitoring by reflective high energy electron diffraction during pulsed laser deposition. *Applied Surface Science* **138-139,** 17–23 (1999).

170. Connell, J. G., Isaac, B. J., Ekanayake, G. B., Strachan, D. R. & Seo, S. S. Preparation of atomically flat $SrTiO_3$ surfaces using a deionized-water leaching and thermal annealing procedure. *Applied Physics Letters* **101,** 98–101 (2012).

171. Jo, J., Tchoe, Y., Yi, G. C. & Kim, M. Real-Time Characterization Using in situ RHEED Transmission Mode and TEM for Investigation of the Growth Behaviour of Nanomaterials. *Scientific Reports* **8,** 1–10 (2018).

172. Wang, P. *et al.* X-ray scattering of calcite thin films deposited by atomic layer deposition: Studies in air and in calcite saturated water solution. *Thin Solid Films* **565,** 277–284 (2014).

173. Müller, M. L., Becker, M. T., Strkalj, N. & MacManus-Driscoll, J. L. Schottky-to-Ohmic switching in ferroelectric memristors based on semiconducting $Hf_{0.93}Y_{0.07}O_2$thin films. *Applied Physics Letters* **121,** 0-7 (2022).

174. Speakman, S. A. Introduction to High Resolution X-Ray Diffraction of Epitaxial Thin Film. *MIT Center for Materials Science and Engineering* (2012).

175. Chason, E. & Mayer, T. M. *Thin film and surface characterization by specular X-ray reflectivity* **1,** 1–67 (1997).

176. Patterson, A. L. The scherrer formula for X-ray particle size determination. *Physical Review* **56,** 978–982 (1939).

177. Vasudevan, R. K., Balke, N., Maksymovych, P., Jesse, S. & Kalinin, S. V. Ferroelectric or non-ferroelectric: Why so many materials exhibit "ferroelectricity" on the nanoscale. *Applied Physics Reviews* **4** (2017).

178. Binnig, G., Quate, C. F. & Gerber, C. Atomic Force Microscope (AFM). *Physical Review Letters* **56,** 51–57 (1986).

179. Güthner, P. & Dransfeld, K. Local poling of ferroelectric polymers by scanning force microscopy. *Applied Physics Letters* **61,** 1137–1139 (1992).

180. Gruverman, A., Alexe, M. & Meier, D. Piezoresponse force microscopy and nanoferroic phenomena. *Nature Communications* **10,** 1–9 (2019).

181. Balke, N. *et al.* Differentiating Ferroelectric and Nonferroelectric Electromechanical Effects with Scanning Probe Microscopy. *ACS Nano* **9,** 6484–6492 (2015).

182. Nahir, T. M., Barsoukov, E. & Macdonald, J. R. *Impedance Spectroscopy: Theory, Experiment, and Applications, Edited by Evgenij Barsoukov (Texas Instruments Inc.) and J. Ross Macdonald (University of North Carolina, Chapel Hill). John Wiley & Sons, Inc.: Hoboken, NJ. 2005. xvii+ 596 pp.* 125.00.*ISBN*0471 − 64749 − 7. (ACS Publications, 2005).

183. Bauerle, J. Study of solid electrolyte polarization by a complex admittance method. *Solid State Communications* **7,** ii (1969).

184. Schenk, T. *et al.* Physical Approach to Ferroelectric Impedance Spectroscopy: The Rayleigh Element. *Physical Review Applied* **10,** 064004 (Dec. 2018).

185. Hodge, I. M., Ingram, M. D. & West, A. R. Impedance and modulus spectroscopy of polycrystalline solid electrolytes. *Journal of Electroanalytical Chemistry* **74,** 125–143 (1976).

186. Irvine, J. T., Sinclair, D. C. & West, A. R. Electroceramics: Characterization by Impedance Spectroscopy. *Advanced Materials* **2,** 132–138 (1990).

187. Von Schweidler, E. R. Studien uber die Anomalien im Verhalten der Dielektrika. *Annalen der Physik* (1907).

188. Ngai, K. L., Jonscher, A. K. & White, C. T. On the origin of the universal dielectric response in condensed matter. *Nature* **277,** 185–189 (1979).

189. Almond, D. P. & Vainas, B. The dielectric properties of random R-C networks as an explanation of the 'universal' power law dielectric response of solids. *Journal of Physics Condensed Matter* **11,** 9081–9093 (1999).

190. Ramírez-González, J., Sinclair, D. C. & West, A. R. Impedance and Dielectric Spectroscopy of Functional Materials: A Critical Evaluation of the Two Techniques. *Journal of The Electrochemical Society* **170,** 116504 (2023).

191. Bruce, P., West, A. R. & Almond, D. P. A new analysis of ac conductivity data in single crystal ß-alumina. *Solid State Ionics* **7,** 57–60 (1982).

192. Mulder, W. H., Sluyters, J. H., Pajkossy, T. & Nyikos, L. Tafel current at fractal electrodes. Connection with admittance spectra. *Journal of Electroanalytical Chemistry* **285,** 103–115 (1990).

193. Morrison, F. D., Jung, D. J. & Scott, J. F. Constant-phase-element (CPE) modeling of ferroelectric random-access memory lead zirconate-titanate (PZT) capacitors. *Journal of Applied Physics* **101** (2007).

194. Becker, M. T., Burkhardt, C. J., Kleiner, R. & Koelle, D. Impedance spectroscopy of ferroelectrics: The domain wall pinning element. *Journal of Applied Physics* **132,** 0-11 (2022).

195. Becker, M., Burkhardt, C. J., Schröppel, B., Kleiner, R. & Koelle, D. Rayleigh analysis and dielectric dispersion in polycrystalline 0.5(Ba0.7Ca0.3)TiO3-0.5Ba(Zr0.2Ti0.8)O3ferroelectric thin films by domain-wall pinning element modeling. *Journal of Applied Physics* **128,** 0-8 (2020).

196. Williams, D. B. & Carter, C. B. *Transmission electron microscopy: A textbook for materials science* 1–760 (Springer, 2009).

197. R.F. Egerton. *Electron Energy-Loss Spectroscopy in the Electron Microscope* 3rd ed. (Springer, 2011).

198. Coenen, T. & Haegel, N. M. Cathodoluminescence for the 21st century: Learning more from light. *Applied Physics Reviews* **4,** 1–35 (2017).

199. Van der Heide, P. *X-Ray Photoelectron Spectroscopy: An Introduction to Principles and Practices* 13 (2011).

200. Müller, M. *et al.* Hard x-ray photoelectron spectroscopy of tunable oxide interfaces. *Journal of Vacuum Science & Technology A* **40,** 013215 (2022).

201. Kalha, C. *et al.* Hard x-ray photoelectron spectroscopy: A snapshot of the state-of-the-art in 2020. *Journal of Physics Condensed Matter* **33** (2021).

202. Covi, E., Mulaosmanovic, H., Max, B., Slesazeck, S. & Mikolajick, T. Ferroelectric-based synapses and neurons for neuromorphic computing. *Neuromorphic Computing and Engineering* **2,** 012002 (2022).

203. Kim, Y. M. *et al.* Direct observation of ferroelectric field effect and vacancy-controlled screening at the $BiFeO_3/La_xSr_{1-x}MnO3$ interface. *Nature Materials* **13,** 1019–1025 (2014).

204. Morozovska, A. N., Eliseev, E. A., Morozovsky, N. V. & Kalinin, S. V. Ferroionic states in ferroelectric thin films. *Physical Review B* **95,** 1–17 (2017).

205. Vaz, C. A. *et al.* Epitaxial ferroelectric interfacial devices. *Applied Physics Reviews* **8** (2021).

206. Hernandez-Martin, D. *et al.* Controlled Sign Reversal of Electroresistance in Oxide Tunnel Junctions by Electrochemical-Ferroelectric Coupling. *Physical Review Letters* **125,** 266802 (2020).

207. Qian, M., Fina, I., Sulzbach, M. C., Sánchez, F. & Fontcuberta, J. Synergetic Electronic and Ionic Contributions to Electroresistance in Ferroelectric Capacitors. *Advanced Electronic Materials* **5,** 1–8 (2019).

208. Li, M. *et al.* A family of oxide ion conductors based on the ferroelectric perovskite $Na_{0.5}Bi_{0.5}TiO_3$. *Nature Materials* **13,** 31–35 (2014).

209. Katayama, K. *et al.* Growth of (111)-oriented epitaxial and textured ferroelectric Y-doped HfO_2 films for downscaled devices. *Applied Physics Letters* **109** (2016).

210. Yun, Y. *et al.* Intrinsic ferroelectricity in Y-doped HfO2 thin films. *Nature Materials* **21,** 903–909 (Aug. 2022).

211. Zhong, H. *et al.* Large-Scale $Hf_{0.5}Zr_{0.5}O_2$ Membranes with Robust Ferroelectricity. *Advanced Materials* **34,** 1–9 (2022).

212. Nukala, P. *et al.* Guidelines for the stabilization of a polar rhombohedral phase in epitaxial $Hf_{0.5}Zr_{0.5}O_2$ thin films. *Ferroelectrics* **569,** 148–163 (2020).

213. Kwon, O., Seol, D., Qiao, H. & Kim, Y. Recent Progress in the Nanoscale Evaluation of Piezoelectric and Ferroelectric Properties via Scanning Probe Microscopy. *Advanced Science* **7** (2020).

214. Guyonnet, J. *et al.* Shear effects in lateral piezoresponse force microscopy at 180° ferroelectric domain walls. *Applied Physics Letters* **95,** 10–13 (2009).

215. Seol, D. *et al.* Determination of ferroelectric contributions to electromechanical response by frequency dependent piezoresponse force microscopy. *Scientific Reports* **6,** 1–10 (2016).

216. Knabe, J., Berg, F., Goß, K., Boettger U & Dittmann, P. R. Dual-Mode Operation of Epitaxial $Hf_{0.5}Zr_{0.5}O_2$: Ferroelectric and Filamentary-Type Resistive Switching. *Physica Status Solidi (a)* (2023).

217. Long, X., Tan, H., Sánchez, F., Fina, I. & Fontcuberta, J. Ferroelectric Electroresistance after a Breakdown in Epitaxial $Hf_{0.5}Zr_{0.5}O_2$ Tunnel Junctions. *ACS Applied Electronic Materials* **5,** 740–747 (2023).

218. Scott, J. F. Models for the frequency dependence of coercive field and the size dependence of remanent polarization in ferroelectric thin films. *Integrated Ferroelectrics* **12,** 71–81 (1996).

219. Pintilie, L. & Alexe, M. Metal-ferroelectric-metal heterostructures with Schottky contacts. I. Influence of the ferroelectric properties. *Journal of Applied Physics* **98,** 1–8 (2005).

220. Starschich, S., Menzel, S. & Böttger, U. Evidence for oxygen vacancies movement during wake-up in ferroelectric hafnium oxide. *Applied Physics Letters* **108** (2016).

221. Jiang, P. *et al.* Wake-Up Effect in HfO_2-Based Ferroelectric Films. *Advanced Electronic Materials* **7,** 1–18 (2021).

222. Wei, Y. *et al.* Magnetic Tunnel Junctions Based on Ferroelectric $Hf_{0.5}Zr_{0.5}O_2$ Tunnel Barriers. *Physical Review Applied* **12,** 1 (2019).

223. Cervo Sulzbach, M. *et al.* Polarization and Resistive Switching in Epitaxial 2 nm $Hf_{0.5}Zr_{0.5}O_2$ Tunnel Junctions. *ACS Applied Electronic Materials* **3,** 3657–3666 (2021).

224. Gruverman, A. *et al.* Tunneling electroresistance effect in ferroelectric tunnel junctions at the nanoscale. *Nano Letters* **9,** 3539–3543 (2009).

225. Brinkman, W. F., Dynes, R. C. & Rowell, J. M. Tunneling conductance of asymmetrical barrier. *Journal of Applied Physics* **41,** 410–414 (1970).

226. Yoong, H. Y. *et al.* Epitaxial Ferroelectric $Hf_{0.5}Zr_{0.5}O_2$ Thin Films and Their Implementations in Memristors for Brain-Inspired Computing. *Advanced Functional Materials* **28,** 1806037 (2018).

227. Jiao, P. *et al.* Electroresistance in metal/ferroelectric/semiconductor tunnel junctions based on a Hf0.5Zr0.5O2 barrier. *Applied Physics Letters* **118,** 0-5 (2021).

228. Wen, Z., Li, C., Wu, D., Li, A. & Ming, N. Ferroelectric-field-effect-enhanced electroresistance in metal/ferroelectric/semiconductor tunnel junctions. *Nature Materials* **12,** 617–621 (2013).

229. Bae, H. *et al.* Ferroelectric Diodes with Sub-ns and Sub-fJ Switching and Its Programmable Network for Logic-in-Memory Applications. *Digest of Technical Papers - Symposium on VLSI Technology* **2021-June,** 1–2 (2021).

230. Chen, A. *et al.* Couplings of Polarization with Interfacial Deep Trap and Schottky Interface Controlled Ferroelectric Memristive Switching. *Advanced Functional Materials* **30,** 1–9 (2020).

231. Taylor, D. V. & Damjanovic, D. Evidence of domain wall contribution to the dielectric permittivity in PZT thin films at sub-switching fields. *Journal of Applied Physics* **82,** 1973–1975 (1997).

232. Mulaosmanovic, H., Chicca, E., Bertele, M., Mikolajick, T. & Slesazeck, S. Mimicking biological neurons with a nanoscale ferroelectric transistor. *Nanoscale* **10,** 21755–21763 (2018).

233. Mikheev, V. *et al.* Ferroelectric Second-Order Memristor. *ACS Applied Materials and Interfaces* **11,** 32108–32114 (2019).

234. Nukala, P. *et al.* Direct observation of reversible oxygen migration and phase transitions in ferroelectric $Hf_{0.5}Zr_{0.5}O_2$ thin-film devices. *Microscopy and Microanalysis* **27,** 956–959 (2021).

235. Li, M. *et al.* Controlling Resistance Switching Polarities of Epitaxial BaTiO3 Films by Mediation of Ferroelectricity and Oxygen Vacancies. *Advanced Electronic Materials* **1,** 1–8 (2015).

236. Ferreyra, C. *et al.* Key Role of Oxygen-Vacancy Electromigration in the Memristive Response of Ferroelectric Devices. *Physical Review Applied* **14,** 1 (2020).

237. Jin, Q. *et al.* Enhanced resistive memory in Nb-doped $BaTiO_3$ ferroelectric diodes. *Applied Physics Letters* **111,** 1–6 (2017).

238. Yang, S. M. *et al.* Mixed electrochemical-ferroelectric states in nanoscale ferroelectrics. *Nature Physics* **13,** 812–818 (2017).

239. Garcia, V. *et al.* Giant tunnel electroresistance for non-destructive readout of ferroelectric states. *Nature* **460,** 81–84 (2009).

240. Prasad, B. *et al.* Large Tunnel Electroresistance with Ultrathin Hf0.5Zr0.5O2 Ferroelectric Tunnel Barriers. *Advanced Electronic Materials* **7,** 1–6 (2021).

241. Salje, E. K. Mild and wild ferroelectrics and their potential role in neuromorphic computation. *APL Materials* **9** (2021).

242. Kohlstedt, H. *et al.* Method to distinguish ferroelectric from nonferroelectric origin in case of resistive switching in ferroelectric capacitors. *Applied Physics Letters* **92,** 2–5 (2008).

243. Max, B., Pešić, M., Slesazeck, S. & Mikolajick, T. Interplay between ferroelectric and resistive switching in doped crystalline HfO_2. *Journal of Applied Physics* **123** (2018).

244. Sulzbach, M. C. *et al.* Blocking of Conducting Channels Widens Window for Ferroelectric Resistive Switching in Interface-Engineered $Hf_{0.5}Zr_{0.5}O_2$ Tunnel Devices. *Advanced Functional Materials* **30,** 1–10 (2020).

245. Sulzbach, M. C. *et al.* Unraveling Ferroelectric Polarization and Ionic Contributions to Electroresistance in Epitaxial $Hf_{0.5}Zr_{0.5}O_2$ Tunnel Junctions. *Advanced Electronic Materials* **6,** 1–8 (2020).

246. Buragohain, P. *et al.* Fluid Imprint and Inertial Switching in Ferroelectric La:HfO_2 Capacitors. *ACS Applied Materials and Interfaces* **11,** 35115–35121 (2019).

247. Choi, W., Kim, S., Jin, Y. W., Lee, S. Y. & Sands, T. D. Capacitance-voltage modeling of metal-ferroelectric-semiconductor capacitors based on epitaxial oxide heterostructures. *Applied Physics Letters* **98,** 7–10 (2011).

248. Park, M. H. *et al.* A comprehensive study on the structural evolution of HfO_2 thin films doped with various dopants. *Journal of Materials Chemistry C* **5,** 4677–4690 (2017).

249. Schmidt, N. *et al.* Impact of Non-Stoichiometric Phases and Grain Boundaries on the Nanoscale Forming and Switching of HfO_x Thin Films. *Advanced Electronic Materials* **10,** 1–10 (2024).

250. Boffelli, M. *et al.* Oxygen hole states in zirconia lattices: Quantitative aspects of their cathodoluminescence emission. *Journal of Physical Chemistry A* **118,** 9828–9836 (2014).

251. Islamov, D. R. *et al.* The Evolution of the Conductivity and Cathodoluminescence of the Films of Hafnium Oxide in the Case of a Change in the Concentration of Oxygen Vacancies. *Physics of the Solid State* **60,** 2050–2057 (2018).

252. Perevalov, T. V. *et al.* The origin of 2.7 eV luminescence and 5.2 eV excitation band in hafnium oxide. *Applied Physics Letters* **104,** 2–6 (2014).

253. Perevalov, T. V., Gismatulin, A. A., Prosvirin, I. P., Pustovarov, V. A. & Gritsenko, V. A. Oxygen Vacancies as Traps Responsible for La-Doped $Hf_{0.5}Zr_{0.5}O_2$ Charge Transport. *The Journal of Physical Chemistry C* **99,** 53–54 (July 2023).

254. Zhang, Z., Sigle, W. & Rühle, M. Atomic and electronic characterization of the a[100] dislocation core in $SrTiO_3$. *Physical Review B - Condensed Matter and Materials Physics* **66,** 1–8 (2002).

255. Kurata, H. & Colliex, C. Electron-energy-loss core-edge structures in manganese oxides. *Physical Review B* **48,** 2102–2108 (1993).

256. De Groot, F., Grioni, M. & Fuggle, J. Oxygen 1s x-ray-absorption. *Physical Review B* **40,** 5715–5723 (1989).

257. Chen, H. *et al.* Reversible modulation of orbital occupations via an interface-induced polar state in metallic manganites. *Nano Letters* **14,** 4965–4970 (2014).

258. Homonnay, N. *et al.* Interface Reactions in LSMO-Metal Hybrid Structures. *ACS Applied Materials and Interfaces* **7,** 22196–22202 (2015).

259. Estandía, S. *et al.* Insights into the atomic structure of the interface of ferroelectric $Hf_{0.5}Zr_{0.5}O_2$ grown epitaxially on $La_{2/3}Sr_{1/3}MnO_3$. *Physical Review Materials* **5** (2021).

260. Kim, K. H. *et al.* Continuous Oxygen Vacancy Gradient in TiO_2 Photoelectrodes by a Photoelectrochemical-Driven "Self-Purification" Process. *Advanced Energy Materials* **12,** 1–9 (2022).

261. Grunes, L. A., Leapman, R. D., Wilker, C. N., Hoffmann, R. & Kunz, A. B. Oxygen K near-edge fine structure: An electron-energy-loss investigation with comparisons to new theory for selected 3d transition-metal oxides. *Physical Review B* **25,** 7157–7173 (1982).

262. Muller, D. A., Nakagawa, N., Ohtomo, A., Grazul, J. L. & Hwang, H. Y. Atomic-scale imaging of nanoengineered oxygen vacancy profiles in $SrTiO_3$. *Nature* **430,** 657–661 (2004).

263. Müller, M. *et al.* Enhanced ferroelectric polarization in TiN/HfO2/TiN capacitors by interface design. *ACS Applied Electronic Materials* **2,** 3152–3159 (2020).

264. Szyjka, T. *et al.* Chemical Stability of IrO_2 Top Electrodes in Ferroelectric $Hf_{0.5}Zr_{0.5}O_2$-Based Metal–Insulator–Metal Structures: The Impact of Annealing Gas. *Physica Status Solidi - Rapid Research Letters* **15,** 2–7 (2021).

265. Baumgarten, L. *et al.* Impact of vacancies and impurities on ferroelectricity in PVD-And ALD-grown HfO2films. *Applied Physics Letters* **118** (2021).

266. Matveyev, Y. *et al.* Effect of Polarization Reversal in Ferroelectric TiN/$Hf_{0.5}Zr_{0.5}O_2$/TiN Devices on Electronic Conditions at Interfaces Studied in Operando by Hard X-ray Photoemission Spectroscopy. *ACS Applied Materials and Interfaces* **9,** 43370–43376 (2017).

267. Chernikova, A. G., Lebedinskii, Y. Y., Khakimov, R. R. & Markeev, A. M. Chemical and electronic properties of interfaces between $RuO_2$and $Hf_{0.5}Zr_{0.5}O_2$ studied by x-ray photoelectron spectroscopy. *Applied Physics Letters* **122,** 0-7 (2023).

268. Matveyev, Y. *et al.* Polarization-dependent electric potential distribution across nanoscale ferroelectric $Hf_{0.5}Zr_{0.5}O_2$ in functional memory capacitors. *Nanoscale* **11,** 19814–19822 (2019).

269. Zahari, F. *et al.* Trap-Assisted Memristive Switching in HfO_2-Based Devices Studied by In Situ Soft and Hard X-Ray Photoelectron Spectroscopy. *Advanced Electronic Materials* **9** (2023).

270. Frankcombe, T. J. & Liu, Y. Interpretation of Oxygen 1s X-ray Photoelectron Spectroscopy of ZnO. *Chemistry of Materials* **35,** 5468–5474 (2023).

271. Strachan, J. P. *et al.* The switching location of a bipolar memristor: Chemical, thermal and structural mapping. *Nanotechnology* **22** (2011).

272. Russo, U., Ielmini, D., Cagli, C. & Lacaita, A. L. Self-accelerated thermal dissolution model for reset programming in unipolar resistive-switching memory (RRAM) devices. *IEEE Transactions on Electron Devices* **56,** 193–200 (2009).

273. Molegraaf, H. J. *et al.* Magnetoelectric effects in complex oxides with competing ground states. *Advanced Materials* **21,** 3470–3474 (2009).

274. Macdonald, J. R. Impedance spectroscopy. *Annals of Biomedical Engineering* **20,** 289–305 (May 1992).

275. Urquidi-Macdonald, M., Real, S. & Macdonald, D. D. Applications of Kramers-Kronig transforms in the analysis of electrochemical impedance data-III. Stability and linearity. *Electrochimica Acta* **35,** 1559–1566 (1990).

276. Fengler, F. P. *et al.* Analysis of Performance Instabilities of Hafnia-Based Ferroelectrics Using Modulus Spectroscopy and Thermally Stimulated Depolarization Currents. *Advanced Electronic Materials* **4,** 1–11 (2018).

277. Jung, M., Ahn, D. & Ahn, S. E. Analysis of Polarization Characteristics Change of the Si-doped HfO_2 with Temperature Using Impedance Spectroscopy. *Journal of the Korean Physical Society* **77,** 784–789 (2020).

278. Marquardt, R. *et al.* Domain Wall Movement in Undoped Ferroelectric HfO_2: A Rayleigh Analysis. *ACS Applied Electronic Materials* **5,** 3251–3260 (2023).

279. Grimley, E. D., Schenk, T., Mikolajick, T., Schroeder, U. & LeBeau, J. M. Atomic Structure of Domain and Interphase Boundaries in Ferroelectric HfO_2. *Advanced Materials Interfaces* **5,** 1–9 (2018).

280. Mittmann, T. *et al.* Optimizing process conditions for improved $Hf_XZr_{1-x}O_2$ ferroelectric capacitor performance. *Microelectronic Engineering* **178,** 48–51 (2017).

281. Chouprik, A., Negrov, D., Tsymbal, E. Y. & Zenkevich, A. Defects in ferroelectric HfO_2. *Nanoscale* **13,** 11635–11678 (2021).

282. Song, T. *et al.* Thickness effect on the ferroelectric properties of La-doped HfO_2 epitaxial films down to 4.5 nm. *Journal of Materials Chemistry C* **9,** 12224–12230 (2021).

283. Xiong, K. *et al.* Epitaxial $Hf_{0.5}Zr_{0.5}O_2$ films: A temperature dependence study. *Applied Physics Letters* **124,** 0-6 (2024).

284. Sinnamon, L. J., Saad, M. M., Bowman, R. M. & Gregg, J. M. Exploring grain size as a cause for "dead-layer" effects in thin film capacitors. *Applied Physics Letters* **81,** 703–705 (2002).

285. Peters, C., Weber, A., Butz, B., Gerthsen, D. & Ivers-Tiffée, E. Grain-size effects in YSZ thin-film electrolytes. *Journal of the American Ceramic Society* **92,** 2017–2024 (2009).

286. Ye, C. *et al.* Physical Mechanism and Performance Factors of Metal Oxide Based Resistive Switching Memory: A Review. *Journal of Materials Science and Technology* **32,** 1–11 (2016).

287. Akinaga, H. & Shima, H. Resistive random access memory (ReRAM) based on metal oxides. *Proceedings of the IEEE* **98,** 2237–2251 (2010).

288. Kumar, S. *et al.* Direct Observation of Localized Radial Oxygen Migration in Functioning Tantalum Oxide Memristors. *Advanced Materials* **28,** 2772–2776 (2016).

289. Sharath, S. U. *et al.* Towards forming-free resistive switching in oxygen engineered HfO_{2-x}. *Applied Physics Letters* **104** (2014).

290. Dou, H. *et al.* Electroforming-Free HfO_2:CeO_2 Vertically Aligned Nanocomposite Memristors with Anisotropic Dielectric Response. *ACS Applied Electronic Materials* **3,** 5278–5286 (2021).

291. Zacharaki, C. *et al.* Depletion induced depolarization field in $Hf_{0.5}Zr_{0.5}O_2$ metal-ferroelectric-semiconductor capacitors on germanium. *Applied Physics Letters* **116** (2020).

292. Liu, K. *et al.* Anisotropic Strain-Mediated Symmetry Engineering and Enhancement of Ferroelectricity in $Hf_{0.5}Zr_{0.5}O_2|La_0.67Sr_0.33MnO_3$ Heterostructures. *Advanced Functional Materials* **33,** 2209925 (2023).

293. De, A. *et al.* Symmetry Engineering of Epitaxial $Hf_{0.5}Zr_{0.5}O_2$ Ultrathin Films. *ACS Applied Materials & Interfaces* (2024).

294. Dildar, I. M., Beekman, C., He, X. & Aarts, J. Hall effect measurements on strained and unstrained thin films of La 0.7 Ca 0.3 MnO 3 and La 0.7 Sr 0.3 MnO 3. *Physical Review B—Condensed Matter and Materials Physics* **85,** 205103 (2012).

295. Lyu, J., Song, T., Fina, I. & Sánchez, F. High polarization, endurance and retention in sub-5 nm $Hf_{0.5}Zr_{0.5}O_2$ films. *Nanoscale* **12,** 11280–11287 (2020).

296. Schenk, T. *et al.* Complex internal bias fields in ferroelectric hafnium oxide. *ACS Applied Materials and Interfaces* **7,** 20224–20233 (2015).

297. Wu, W., Wong, K. H. & Choy, C. L. Interface-oxygen-loss-controlled voltage offsets in epitaxial $Pb(Zr_{0.52}Ti_{0.48})O_3$ thin-film capacitors with $La_{2/3}Sr_{1/3}MnO_3$ electrodes. *Applied Physics Letters* **85,** 5013–5015 (2004).

298. Fengler, F. P., Hoffmann, M., Slesazeck, S., Mikolajick, T. & Schroeder, U. On the relationship between field cycling and imprint in ferroelectric $Hf_{0.5}Zr_{0.5}O_2$. *Journal of Applied Physics* **123,** 0-8 (2018).

299. Fengler, F. P. *et al.* Domain Pinning: Comparison of Hafnia and PZT Based Ferroelectrics. *Advanced Electronic Materials* **3** (2017).

300. Fister, T. T. *et al.* In situ characterization of strontium surface segregation in epitaxial $La_{0.7}Sr_{0.3}MnO_3$ thin films as a function of oxygen partial pressure. *Applied Physics Letters* **93** (2008).

301. Dulli, H., Dowben, P. A., Liou, S.-H. & Plummer, E. W. Surface segregation and restructuring of colossal-magnetoresistant manganese perovskites $La_{2/3}Sr_{1/3}MnO_3$. *Physical Review B* **62,** R14629 (2000).

302. Chen, L. *et al.* Surface and interface properties of $La_{2/3}Sr_{1/3}MnO_3$ thin films on $SrTiO_3$ (001). *Physical Review Materials* **3,** 044407 (2019).

303. Kubicek, M. *et al.* Tensile lattice strain accelerates oxygen surface exchange and diffusion in $La_{1-x}Sr_xCoO_{3-\delta}$ thin films. *ACS nano* **7,** 3276–3286 (2013).

304. Pintilie, L., Vrejoiu, I., Hesse, D., LeRhun, G. & Alexe, M. Ferroelectric polarization-leakage current relation in high quality epitaxial $Pb(Zr,Ti)O_3$ films. *Physical Review B - Condensed Matter and Materials Physics* **75,** 1–14 (2007).

305. Jiang, L. *et al.* Tunneling electroresistance induced by interfacial phase transitions in ultrathin oxide heterostructures. *Nano Letters* **13,** 5837–5843 (2013).

306. Srinivasan, G., Rasmussen, E. T., Levin, B. J. & Hayes, R. Magnetoelectric effects in bilayers and multilayers of magnetostrictive and piezoelectric perovskite oxides. *Physical Review B - Condensed Matter and Materials Physics* **65,** 1–7 (2002).

307. Hizi, W., Rahmouni, H., Gassoumi, M., Khirouni, K. & Dhahri, S. Transport properties of $La_{0.9}Sr_{0.1}MnO_3$ manganite. *European Physical Journal Plus* **135,** 1–13 (2020).

308. Dussan, S., Kumar, A., Scott, J. & Katiyar, R. S. Effect of electrode resistance on dielectric and transport properties of multiferroic superlattice: A Impedance spectroscopy study. *AIP Advances* **2** (2012).

309. Li, T. *et al.* Origin of Ferroelectricity in Epitaxial Si-Doped HfO_2 Films. *ACS Applied Materials and Interfaces* **11,** 4139–4144 (2019).

310. Zhang, Z. *et al.* Manipulating the carrier concentration and phase transition via Nb content in $SrTiO_3$. *Scientific Reports* **12,** 1–7 (2022).

311. Lim, E. W. & Ismail, R. Conduction mechanism of valence change resistive switching memory: A survey. *Electronics (Switzerland)* **4,** 586–613 (2015).

312. García, H. *et al.* Influences of the temperature on the electrical properties of HfO_2-based resistive switching devices. *Electronics (Switzerland)* **10,** 1–9 (2021).
313. Lew, W. S. *et al.* Oxygen vacancy density dependence with a hopping conduction mechanism in multilevel switching behavior of HfO_2-based resistive random access memory devices. *ACS Applied Electronic Materials* **2,** 3160–3170 (2020).
314. Larcher, L. *et al.* A compact model of program window in HfO_x RRAM devices for conductive filament characteristics analysis. *IEEE Transactions on Electron Devices* **61,** 2668–2673 (2014).
315. Vinuesa, G. *et al.* Impact of the temperature on the conductive filament morphology in HfO_2-based RRAM. *Materials Letters* **357,** 1–5 (2024).
316. Gritsenko, V. A., Perevalov, T. V. & Islamov, D. R. Electronic properties of hafnium oxide: A contribution from defects and traps. *Physics Reports* **613,** 1–20 (2016).
317. Yildiz, A., Iacomi, F. & Mardare, D. Polaron transport in TiO_2 thin films. *Journal of Applied Physics* **108** (2010).
318. Wang, Z. *et al.* Transport properties of HfO 2-x based resistive-switching memories. *Physical Review B - Condensed Matter and Materials Physics* **85,** 1–10 (2012).
319. Jacobs, C. G. & Hershkowitz, N. Mössbauer-effect observations of recoil radiation damage following Coulomb excitation in various Hf compounds. *Physical Review B* **1,** 839–850 (1970).
320. Schnakenberg, J. Polaronic Impurity Hopping Conduction. *Physica Status Solidi (B)* **28,** 623–633 (1968).
321. Austin, I. G. & Mott, N. F. Polarons in crystalline and non-crystalline materials. *Advances in Physics* **50,** 757–812 (2001).
322. Clark, S. J., Lin, L. & Robertson, J. On the identification of the oxygen vacancy in HfO_2. *Microelectronic Engineering* **88,** 1464–1466 (2011).
323. Wang, Z., Yu, H. & Su, H. The transport properties of oxygen vacancy-related polaron-like bound state in HfO_x. *Scientific Reports* **3,** 1–6 (2013).
324. Baumgarten, L. *et al.* Smart Design of Fermi Level Pinning in HfO_2-Based Ferroelectric Memories. *Advanced Functional Materials* **2307120,** 1–16 (2023).
325. Petraru, A. *et al.* Distinguishing the Rhombohedral Phase from Orthorhombic Phases in Epitaxial Doped HfO2 Ferroelectric Films. *ACS Applied Materials and Interfaces* (2024).
326. Bégon-Lours, L. *et al.* Stabilization of phase-pure rhombohedral $HfZrO_4$ in pulsed laser deposited thin films. *Physical Review Materials* **4,** 1–6 (2020).
327. Wang, Y. *et al.* A stable rhombohedral phase in ferroelectric $Hf_{0.5}Zr_{0.5}O_2$ capacitor with ultralow coercive field. *Science* **381,** 558–563 (2023).
328. Schroeder, U. *et al.* Temperature-Dependent Phase Transitions in $Hf_xZr_{1-x}O_2$ Mixed Oxides: Indications of a Proper Ferroelectric Material. *Advanced Electronic Materials* **8,** 1–9 (2022).
329. Song, T. *et al.* Impact of La Concentration on Ferroelectricity of La-Doped HfO_2 Epitaxial Thin Films. *ACS Applied Electronic Materials* **3,** 4809–4816 (2021).
330. Kita, K., Kyuno, K. & Toriumi, A. Permittivity increase of Yttrium-doped HfO_2 through structural phase transformation. *Applied Physics Letters* **86,** 1–3 (2005).

Appendix A

Hafnia Phase Determination

In an attempt to clarify the crystallographic phase present in this film, we combine the use of XRD, PFM and STEM. The identity of the ferroelectric phase of epitaxial HfO_2 based films grown on LSMO buffer layers is under debate. Distinctions are made between a rhombohedral R3m phase (r-phase)[139, 325–327] or the orthorhombic [135, 140, 211] $Pca2_1$ phase (o-phase), which has also been observed in polycrystalline samples [112] and epitaxial films grown on ITO [137].

Crystallographically, these two phases are distinguished by their lattice parameters, where for the o-phase ($a \neq b \neq c$) and for the r phase all edges are equal. Furthermore, the angles between the edges equivalent, but for the o-phase $\alpha = 90°$ and the r-phase $\alpha \neq 90°$. The debate arises from a rhombohedral distortion being present in the (111) oriented hafnia based films, where the out of plane lattice parameter is slightly larger than those of in plane oriented domains. Yun et al. observed this rhombohedral distortion, yet by analysing the family (002) lattice planes observed $a \neq b \approx c$, significant evidence for the o-phase. This was termed an o-phase with a rhombohedral distortion [135]. Strictly speaking, such a phase would be triclinic. However, the nature of the ferroelectric phase is important, since in an orthorhombic ferroelectric phase the polarisation points along the [001] direction, whereas in an r-phase it points along [111]. Therefore, an o-phase with (111) orientation is expected to have a significant projection of in-plane polarisation, which was observed by Yun.

We demonstrated the existence of a rhombohedral distortion within the presently investigated films in section 4.3. However, this distortion is small, having a deviation of $\delta = 0.74°$ from the ideal $\alpha = 90°$. We further analysed the family of (002) lattice planes by performing a ϕ scan at $2\theta = 35°$ and $\chi = 55.7°$ using a lab-based diffractometer. 12 reflections were observed, corresponding to 200, 020 and 002 reflections with a further 4 substrate symmetry imposed domains for each reflection. Each reflection was measured along 2θ and summed improve the signal to noise ratio, which is shown in Fig.A.1a). For o-phase symmetry, a

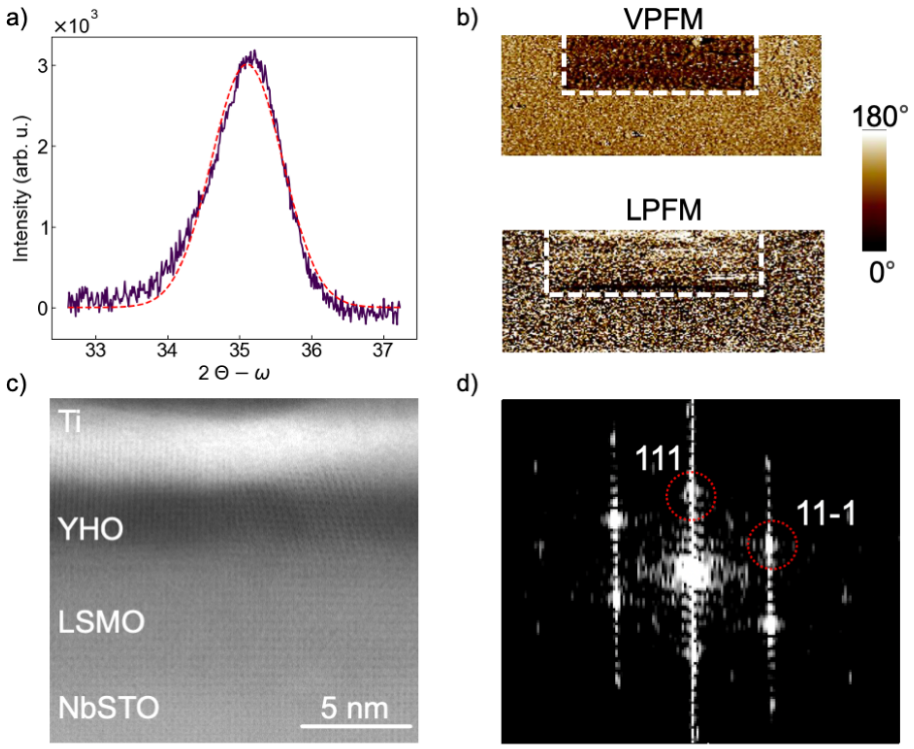

Figure A.1: a) Sum of 12 reflections of 2θ scan across the in-plane 002 reflection at $\chi = 55.7°$ b) Vertical and lateral PFM phase signal c) Bright-field image of two differently oriented YHO grains d) FFT of a single YHO grain

difference in lattice parameters is expected to result in multiple peaks being present. Here, the data can be fitted well with a single peak, suggesting r-phase symmetry. However, a lab-based source has large beam size, causing significant interference from different areas from the film and causing peak broadening. Therefore, higher resolution scans with a synchrotron point source would be required for definite attribution. Finally, the FWHM of the 002 peak is $\sim 1°$, is equivalent to the FWHM of 11-1 peak at $\chi = 71°$, suggesting suggesting the experimental data corresponds to a single peak.

We can distinguish a ferroelectric o-phase from a ferroelectric r-phase by the presence of an in-plane signal from the projection of a [001] polarization along in-plane for (111) out-of-plane grain orientation in the former and lack of projection of [111] polarization along in-plane for (111) out-of-plane orientation in the latter. We performed PFM to determine the presence of in-plane polarisation by poling the sample surface with +6V and -4V and a reading AC amplitude of 1V. Fig. A.1 b) displays the vertical piezoresponse phase signal (VPFM) and lateral PFM (LPFM) phase signal, corresponding to mainly out of plane and singly in plane polarisation contributions respectively. The measured amplitudes, data not shown, did not show a significant response, as expected for ferroelectrics. The phase images

in VPFM do show the clear phase contrast between up and down polarisation directions. A weaker difference in phase signal is also present in the lateral direction, indicating the presence of in-plane polarisation. However, this is not conclusive evidence on the o-phase vs r-phase, since the in-plane polarisation signal is low and can also originate from minority contributions of grain orientations other than (111).

We now inspect a bright field STEM image showing two different grain orientations, shown in Fig. A.1 c). Three-fold symmetry is clearly present in the right grain, indicative of (111) orientation. The left grain does not show obvious three-fold symmetry, indicative of (001) orientation or a parasitic monoclinic phase. A (001) oriented r-phase grain could contribute to an in-plane polarisation response. A fast-fourier transform (FFT) would be required for phase identification, however the signals here are too noisy for adequate analysis.

An FFT of a single grain from the HAADF STEM image in Fig 3.7 is shown in Fig. A.1 d). The 111, and -111 the distances of crystallographic planes were determined to be 3.07 Å and 2.26 Å, correlating with the results measured in section 5.5. The observed FFT corresponds well to the simulated pattern of the o-phase.

The results from XRD and STEM therefore yield inconclusive phase assignments. It is important to note that for XRD, a YHO sample with 9 nm thickness was used to maximise the signal to noise ratio. For STEM, a sample with nominally 5 nm thickness was used. However the STEM lamella was extracted at the edge of the sample, yielding to artificially thinner LSMO and YHO. It is therefore not possible to assign the crystallographic phase with confidence.

Appendix B

Extended Impedance Analysis

B.1 Fitting with the Domain Wall Pinning Element

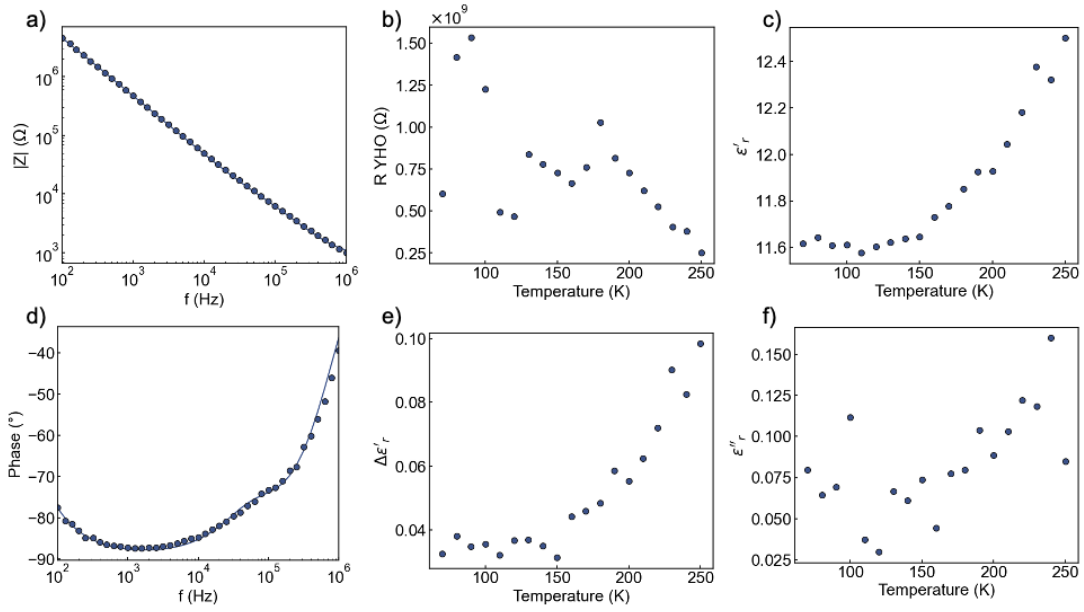

Figure B.1: a)|Z| and d) phase of the HRS fitted in section 6.2 where the CPE is replaced by Z_{DWP} b,c,e,f) showing the temperature dependence of the YHO layer fitted with a parallel (R-Z_{DWP}) with b) the layer resistance R c) the real part of the permittivity ε_r' e) the dispersion of the real part of the permittivity $\Delta\varepsilon_r'$ and f) the imaginary part of the permittivity ε_r''

Fig. B.1 a) and d) show the fitted impedance spectra where the CPE in the equivalent circuit described in section 6.2 is replaced by Z_{DWP}. The features in the spectra are well accounted for and show an excellent fit. The fit parameters are summarised in Table B.1 and compared to parameters obtained from poly-crystalline undoped HfO_2 [278] and Si-doped

HfO_2[184]. As discussed previously, the ε_r' is lower than comparable systems, whereas the losses ε_r'' are of similar magnitude. However, the dispersion obtained is significantly lower than those obtained in [278], which indicates a lower degree of domain pinning. This may originate from the difference between poly-crystalline and the epitaxial films used here.

	Ref [184]	Ref [278]	This work
ε_r'	35.4	37.4	14.4
ε_r''	0.33	0.1	0.197
$\Delta\varepsilon_r'$	N/A	0.176	0.063

Table B.1: Summary of Z_{DWP} fit parameters in the HRS, compared with literature values.

The coupling between the frequency dispersion and the excitation field can be investigated through Rayleigh analysis by successively increasing the measurement AC amplitude [184]. This was attempted, however irreversible degradation in the interfacial layer prevented reliable interpretation. Furthermore, the temperature dependence of the impedance spectra in the HRS was also investigated by fitting the data with the Z_{DWP} element instead of the CPE for the YHO layer. The temperature dependent resistance shown in B.1b), shows a similar trend 6.8a), where the low temperature region is difficult to fit, however decreasing slightly at high temperature. The ε_r' shown in Fig. B.1c) increases slightly and is in accordance with previously reported trends [328]. The $\Delta\varepsilon_r'$ shown in Fig. B.1e) again displays a plateau until $\sim$150K beyond which the dispersion increases. This may be related to the freezing of domain walls at low temperature. At higher temperature, the domain walls can become more mobile and is therefore pinned more strongly. The losses ε_r'' do not show a clear trend. Importantly, this type of analysis opens up wide ranging opportunities for the study and evolution of ferroelectric domains at varying atmospheric conditions. However, such an analysis is ill-suited for complex device stacks, such as those studied here, where many parasitic influences to be considered.

B.2 Thickness Dependence

The impact of the YHO layer thickness was investigated. As shown in Fig. B.2 a), increasing YHO d_{111} is found with decreasing thickness, consistent with previous reports. Fig. B.2 b) shows the permittivity-voltage relation at 1 MHz and confirms that each of the films grown are still ferroelectric. Importantly, the extracted permittivity decreases with decreasing thickness, which is the opposite of what has been shown in the Ref. [329] using an STO|LSMO|HZO device stack. As alluded to before, this could originate from an additional capacitance in

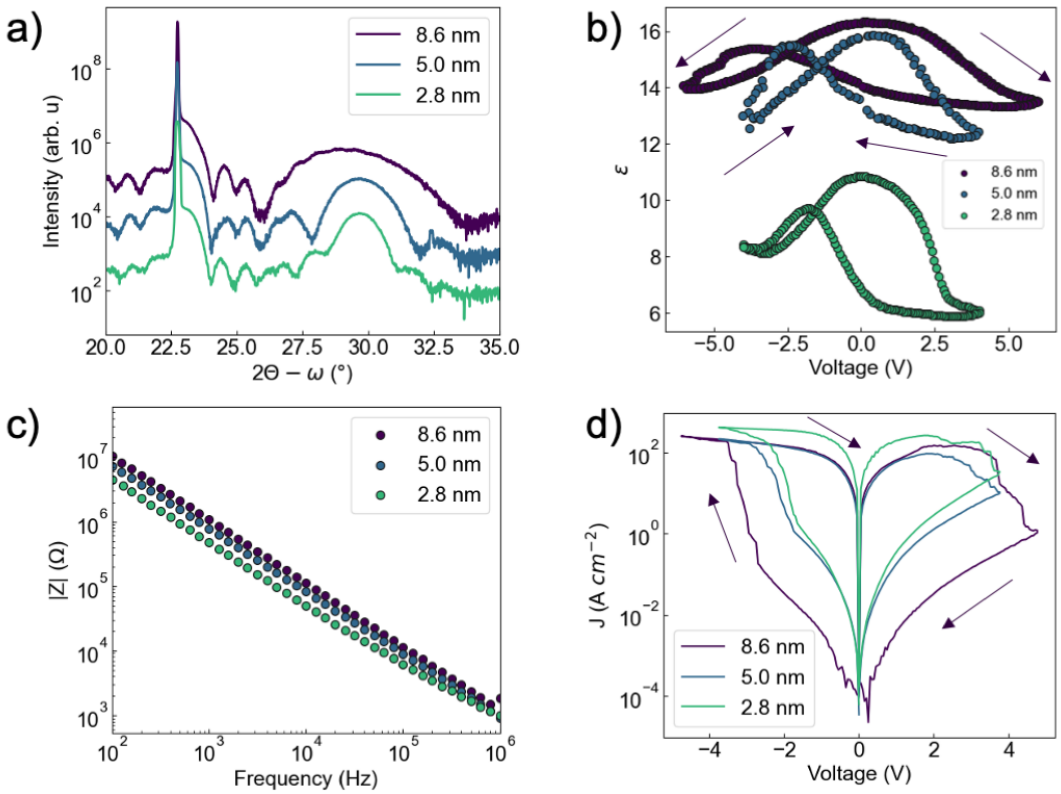

Figure B.2: YHO thickness dependence of the a) $2\theta - \omega$ reflections b) permittivity voltage relation c) impedance magnitude |Z| spectra d) SOT J-V relation

series. Fig. B.2 c) shows the averaged impedance spectra from the different films. The low-frequency relaxation increases in magnitude with increasing thickness of the YHO layer, confirming that the relaxation corresponds to YHO. Potential grain boundary contributions to the impedance were considered. As shown in section 5.5 by transmission electron microscopy, the investigated film showed columnar grains, where grain boundary conduction paths are parallel to grain conduction. Therefore these cannot be identified separately using impedance spectroscopy. Finally, Fig. B.2 d) shows that the SOT can be stabilised for thicknesses down to 2.8 nm. Illustrated are average current densities, which were taken from 10 different devices for each thickness. The current density decreases with increasing film thickness, indicating that the current conduction is indeed bulk-limited rather than interface-limited.

B.3 Dopant Concentration Dependence

The impact of the dopant was investigated by doping HfO_2 with 0, 7, 20 mol % Y and 50 mol % Zr. Structurally, the XRD patterns in Fig. B.3 a), are consistent with the o-phase primary

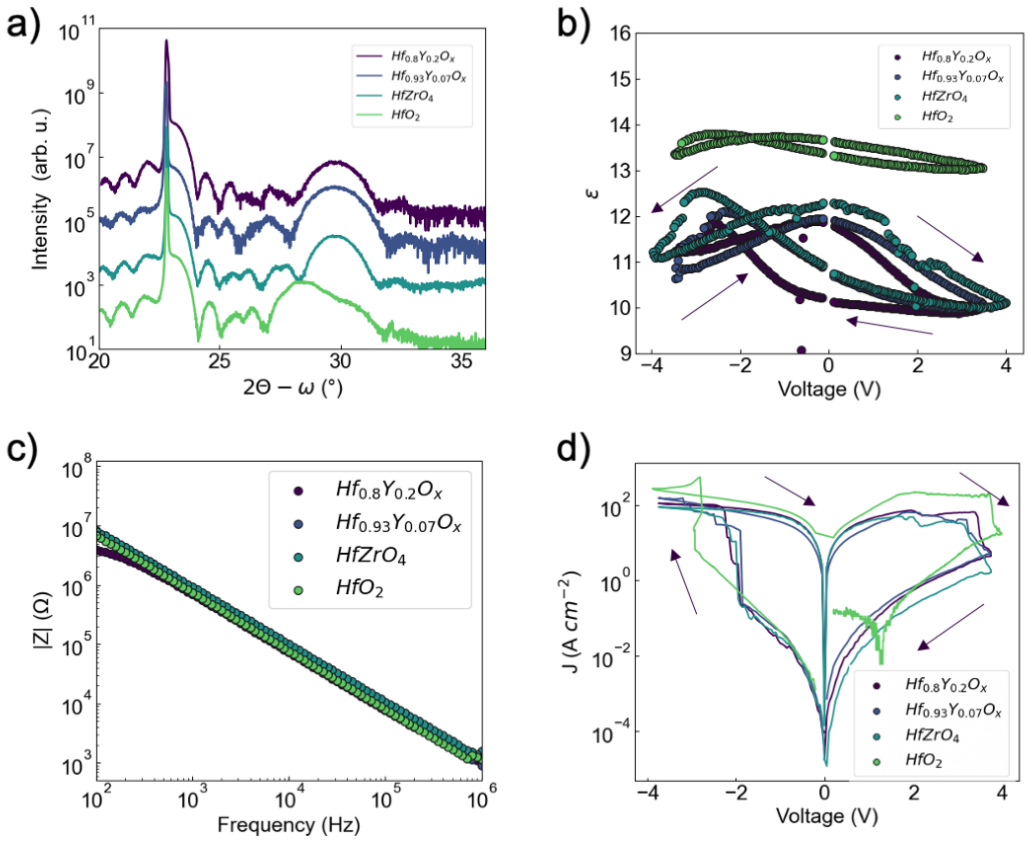

Figure B.3: Dopant concentration dependence of the a) $2\theta - \omega$ reflections b) permittivity voltage relation c) impedance magnitude $|Z|$ spectra d) SOT J-V relation

peak just below 30° in the doped HfO_2 films and no secondary phases are evident. Conversely, for pure HfO_2, a significant reflection at 28.3° appears, corresponding to the monoclinic phase. Considering the permittivity of the films, shown in Fig. B.3 b), surprisingly, the permittivity of the dopant-free HfO_2 is larger than the phase-pure doped films. This is in contrast to previous reports on dopant-dependent permittivity in HfO_2 [330] and strongly suggests that extrinsic phenomena have a significant impact on the permittivity measured here. Furthermore, the impedance spectra shown in Fig. B.3 c), indicate no significant trends with changing dopant concentration. Finally, Fig. B.3 d) shows the SOT can be stabilised with each dopant concentration, indicating that the dopant element plays no considerable role during resistive switching.